Spring 2017

Probing the catalytic properties of Ni-based bimetallic phosphides for deep hydrodesulfurization

Peter J. Topalian
Western Washington University, topalip@wwu.edu

Recommended Citation

Topalian, Peter J., "Probing the catalytic properties of Ni-based bimetallic phosphides for deep hydrodesulfurization" (2017). *WWU Graduate School Collection*. 575.
https://cedar.wwu.edu/wwuet/575

Probing the catalytic properties of Ni-based bimetallic phosphides for deep hydrodesulfurization

By

Peter J. Topalian

Accepted in Partial Completion

Of the Requirements for the Degree

Master of Science

Kathleen L. Kitto, Dean of the Graduate School

ADVISORY COMMITTEE

Chair, Dr. Mark E. Bussell

Dr. David L. Patrick

Dr. Tim Kowalczyk

MASTER'S THESIS

Signature: Peter Topalian

Date: 05/19/2017

Probing the catalytic properties of Ni-based bimetallic phosphides for deep hydrodesulfurization

A Thesis
Presented to
The Faculty of
Western Washington University

In Partial Fulfillment
Of the Requirements for the Degree
Master of Science

By
Peter Topalian
May 2017

Abstract

Global demand for transportation fuels continues to rise while environmental standards for sulfur impurities in fuels have become more stringent. Upgrading crude oil feed stocks via deep hydrodesulfurization (HDS) is necessary to meet the ultra-low sulfur standards for transportation fuels. Transition metal phosphides (e.g. Ni_2P, Ru_2P) represents a new class of hydrotreating catalysts that show promise for improved HDS properties relative to conventional molybdenum sulfide based catalysts. Incorporating a second metal into Ni_2P can influence the surface properties and be used to tailor the catalytic properties (activity, selectivity) for improved hydrotreating performance. Bimetallic phosphides catalysts having the formulas $Ni_xM_{2-x}P/SiO_2$ (M = Ru, Rh) were synthesized over a range of compositions. Metal hypophosphite precursors prepared via incipient wetness were reduced via temperature programmed reduction (TPR). The resulting catalysts were characterized using X-ray diffraction (XRD), X-ray photoelectron spectroscopy (XPS) and CO chemisorption. HDS properties were probed using 4,6-dimethyldibenzothiophene (4,6-DMDBT) as a model compound. The XRD patterns showed single phase and phase-segregated materials having average crystallize sizes of 5-10 nm. CO chemisorption measurements showed an increase in active site density for the higher nickel content catalysts (e.g. $Ni_{1.85}Ru_{0.15}P/SiO_2$). HDS measurements were carried out using a model feed of 1000 ppm 4,6-DMDBT in decalin over a range of temperatures (533-653 K). A substantial increase in the TOFs and HDS activity was observed for the bimetallic phosphides having high nickel contents. For the $Ni_xRh_{2-x}P/SiO_2$ series, the product selectivity was observed to change with metal composition; for Rh-rich phases ($x < 0.25$), the hydrogenation product (3,3’-dimethylbicyclohexane) was favored while for Ni-rich compositions ($x > 0.25$) the partially hydrogenated product (3,3’-dimethylcyclohexylbenzene) dominated.

Acknowledgements

Thesis Committee Chair:	Dr. Mark E. Bussell
Thesis Committee Members:	Dr. David L. Patrick
	Dr. Tim Kowalczyk
Research Group Members:	Paul Cochran, Tess Clinkingbeard, Catherine Miles, and Liam Carmody
Instrument Technicians:	Kyle Mikkelsen, Sam Danforth, and Charles Wandler
Financial Support:	National Science Foundation
	WWU Ross Travel Grant

Western Washington University Chemistry Department

Western Washington University Advanced Materials Science and Engineering Center

Table of Contents

List of Figures

Introduction

1.1 Hydrotreating

Hydrotreating is an industrial process in which hydrogen, in the presence of a catalyst, is consumed either by hydrogenation of unsaturated hydrocarbons that are present in crude oil distillate fractions, or by removal of heteroatom impurities (sulfur, nitrogen and oxygen) via hydrogenolysis reactions such as hydrodesulfurization (HDS), hydrodenitrogenation (HDN), hydrodeoxygenation (HDO). These hydrotreating processes are critically important for the upgrading of crude oil feed stocks into ultra-low sulfur transportation fuels.[1]

Crude oil feedstocks are comprised of paraffins, naphthenes, and aromatic compounds. At higher boiling points, the heavier naphthenes and aromatic compounds dominate the fractions. Regarding the higher boiling point compounds, aromatics are considered the least desirable as they often have different chemical properties that can significantly influence their reactivity and differentiate them from other compounds with higher H/C ratios that are found in the same distillate fraction.[1] Some aromatics are also carcinogenic and are under strict environmental regulations that limit their concentration in transportation fuels. Noble metal catalysts are effective at hydrogenating aromatics to saturated compounds, however, they are quickly poisoned by heteroatom impurities such as sulfur and nitrogen.

1.2 Ultra-low Sulfur Transportation Fuels

There are negative environmental impacts that come with the use of petroleum-based transportation fuels.[2] Volatile organic compounds (unburned hydrocarbons) are a common pollutant and can contribute to the smog levels in cities. Nitrogen oxides (NO_x, x = 1,2) are also a common component in vehicle exhaust and contribute to acid rain formation and to undesirable tropospheric ozone. Additionally, NO_x gases contribute to the weakening of human defenses against respiratory contaminants.[3] Another harmful side effect of combusting petroleum-based transportation fuels is the production of carbon monoxide (CO) which, at elevated levels, contributes to heart disease and will diminishes the ability to get oxygenated blood to vital organs.

Harmful gases are removed from a vehicle exhaust streams by catalytically converting them to less harmful compounds through the use of emission control devices such as catalytic converters. These emission control devices use noble metals (i.e. Pd, Pt, and Rh) to catalyze the reactions outlined in Equations 1.1-1.3.[4]

$$2NO_x \rightarrow N_2 + xO_2 \qquad \textbf{Equation 1.1}$$

$$2CO + O_2 \rightarrow 2CO_2 \qquad \textbf{Equation 1.2}$$

$$C_xH_y + zO_2 \rightarrow xCO_2 + zH_2O \qquad \textbf{Equation 1.3}$$

Emission control devices are deactivated by sulfur present in transportation fuels.[5] Sulfur atoms bind irreversibly to the noble metal catalysts in emission control devices and dramatically decrease the effectiveness of emission control devices for mitigating the harmful exhaust gases due to sulfur poisoning of the catalysts.[6] Environmental protection agencies around the world are placing restrictions on the sulfur content in transportation fuels. The U.S. Environmental Protection Agency (EPA) aims to restrict sulfur content in gasoline to 10 ppm by the year 2017. The European Union (EU) and China are enforcing similar restrictions on the sulfur content for their transportation fuels as shown in Table 1.1.[7-8]

Table 1.1. Current and future sulfur limits by county.[7-8]

	Sulfur Limit (ppm)	
Country	**Diesel**	**Gasoline**
U.S.	15 (2014)	10 (2017)
China	10 (2017)	10 (2017)
Europe	10 (2009)	10 (2009)

While restrictions are being placed on the sulfur content in transportation fuels, the crude oil-feedstocks supplied to U.S. refineries are steadily becoming more sulfur-rich; this trend is shown in Figure 1.1.

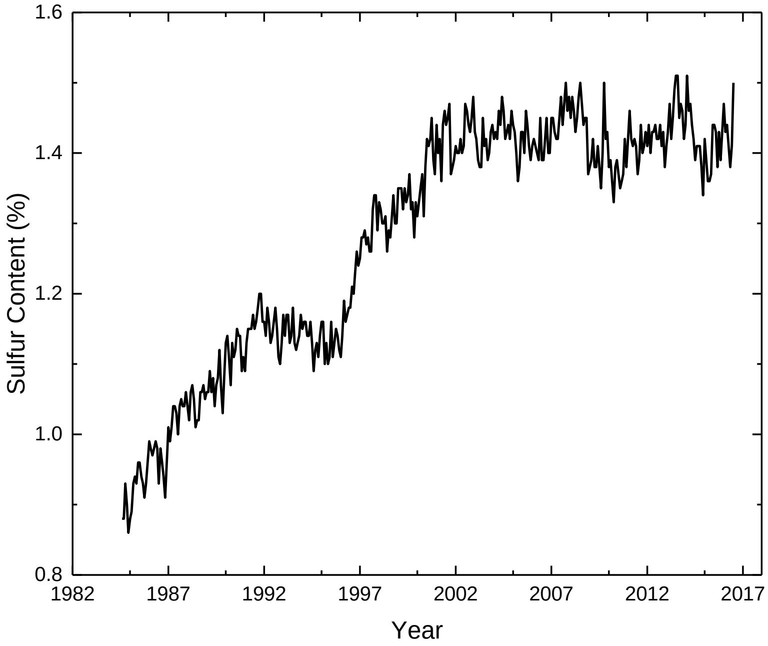

Figure 1.1. Sulfur content (wt%) of crude oil reaching U.S. refineries during 1985-2016.[9]

This increase in sulfur content can be attributed to the diminishing quality of reaming petroleum reserves. In Table 1.2 these increases are most apparent in the oil sands of Canada where the sulfur content reachs ~5 wt%.[1,9] As of 2015, Canada represents 40% of the crude oil imports to the U.S.[9]

Table 1.2. Common impurities in crude oil from various sources.[1,9]

Impurity	Crude Oil Source						
	Arabian Light	Arabian Heavy	Attaka	Boscan	Shale Oil	Tar Sands	U.S
Sulfur (wt%)	1.8	2.9	0.07	5.2	0.7	5.0	2.0
Nitrogen (wt%)	0.1	0.2	<0.1	0.7	1.6	0.5	<0.1
Oxygen (wt%)	<0.1	<0.1	<0.1	<0.1	1.5	0.5	<0.1
Vanadium (ppm)	18	50	<1	1200	-	150	-
Nickel (ppm)	4	16	<1	150	-	75	-

1.3 Hydrodesulfurization

Processing low quality petroleum resources into ultralow sulfur transportation fuels requires improved hydrotreating catalysts. Conventional hydrotreating catalysts are effective at removing sulfur from lower boiling point, organosulfur compounds such as benzothiophene, which has a relatively high reactivity when compared with higher boiling point compounds such as alkyl-substituted benzothiophenes. Due to the steric hindrance caused by the alkyl substituents, these higher boiling point compounds are highly refractory with respect to conventional hydrotreating catalysts. This issue is outlined below in Figure 1.2 where HDS of benzothiophenes and dibenzothiophenes was successful, but alkyl-substituted dibenzothiophenes remained.

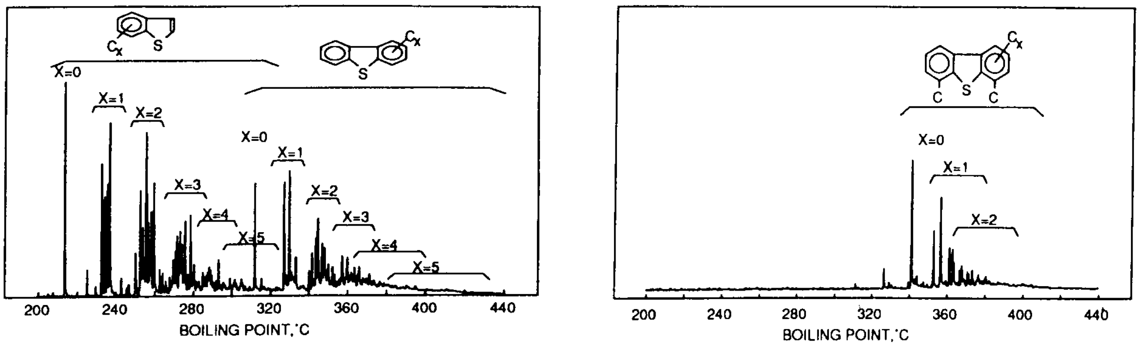

Figure 1.2. GC traces showing a light cycle oil (LCO) (left) and hydrotreated LCO (right) using a sulfided Co-Mo catalyst.[1]

Alkyl-substituted dibenzothiophenes (e.g. 4,6-dimethyldibenzothiophene) represent a class of high boiling point, organosulfur compounds that require "deep" HDS processing. Deep HDS refers to the conversion of the heaviest organosulfur compounds to sulfur-free hydrocarbons. While conventional catalysts are capable of converting these heavier organosulfur compounds, it is accomplished through high-cost methods such as increasing the temperature and pressure of the reactor. Industrial catalysts are typically based on molybdenum sulfide supported on alumina, i.e. MoS_2/Al_2O_3. Molybdenum sulfide adopts an anisotropic structure that is composed of layers of Mo atoms sandwiched between layers of S atoms (Figure 1.3).[9] This structure limits the exposure of the Mo active sites to the edges of MoS_2 crystallites.

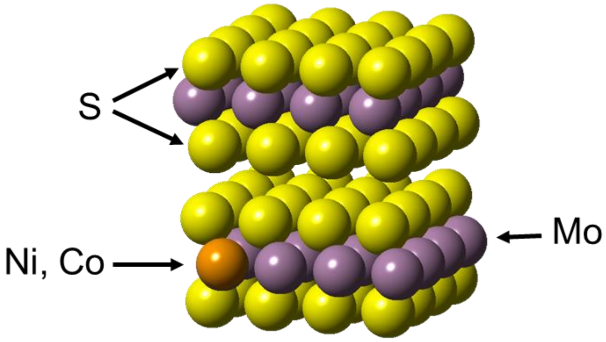

Figure 1.3. Anisotropic structure of a Co or Ni promoted MoS_2/Al_2O_3 catalyst.

Optimization of MoS_2-based catalysts has revealed that the incorporation of a second metal such as nickel or cobalt that can act as a promoter by preferentially replacing Mo atoms at edge sites forming a localized Co(Ni)-Mo-S phase that increases HDS activity.[10,13-14] This increase in HDS activity is caused by an electronic transfer from the promoter atom to neighboring Mo atoms that results in an optimized metal-sulfur bond for HDS activity.[14]

Studies on the reaction pathways available for the HDS of 4,6-dimethyldibenzothiophene (4,6-DMDBT) show two primary routes for the removal of sulfur; these are outlined below in Figure 1.4.[11]

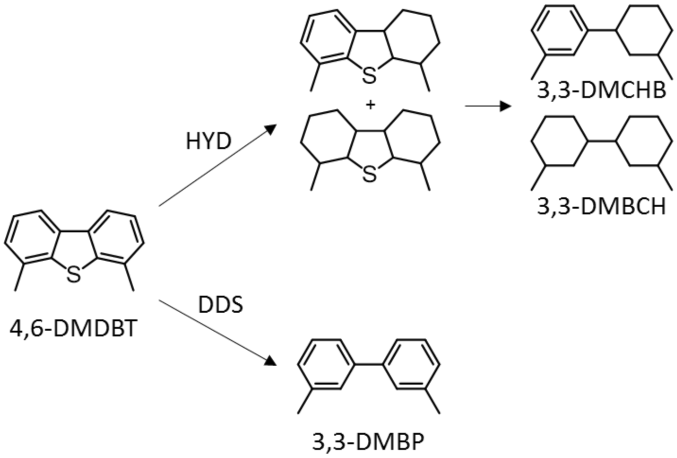

Figure 1.4. Hydogenation (HYD) and direction desulfurization (DDS) reaction pathways for the HDS of 4,6-DMDBT.[11]

The direction desulfurization (DDS) pathway results in the removal of the sulfur atom via hydrogenolysis of the two C-S bonds leading to the product 3,3-dimethylbiphenyl (3,3-DMBP).[1,11-13] In a compound like 4,6-DMDBT, this pathway is impeded by the presence of the two alkyl groups that sterically hinder the DDS pathway.[1,11-13] Due to this steric hindrance, a second pathway is observed in which hydrogenation (HYD) of one or both of the aromatic rings removes rigidity from the compound and allows for greater catalytic access to the sulfur atom. This results in the products 3,3-dimethylcyclohexylbenzene (3,3-DMCHB) or 3,3-dimethylbicyclohexane (3,3-DMBCH). Other reaction pathways that involve isomerization and demethylation can also occur in an effort to release the steric hindrance of the alkyl groups.[11]

1.4 Metal Phosphide Catalysts

To effectively process petroleum feedstocks into ultra-low sulfur transportation fuels, more active HDS catalysts are needed. Transition metal phosphides represent a new class of catalysts that have been the subject of significant research in recent years due to their high HDS activities and stabilities.[15-16] A number of metal phosphides, such as MoP, Co_2P, Ni_2P, and Fe_2P, have shown activity in performing HDS of petroleum feedstocks and while metal phosphides do not require a sulfiding agent like conventional Co(Ni)-MoS_2/Al_2O_3 catalysts, they are similarly tolerant to sulfur poisoning.[16, 17-18] While conventional catalysts phases, such as the Co(Ni)-MoS_2, adopt an anisotropic structure that limits the active site dispersion, metal phosphides benefit from a greater active site dispersion through their isotropic structures.[16]

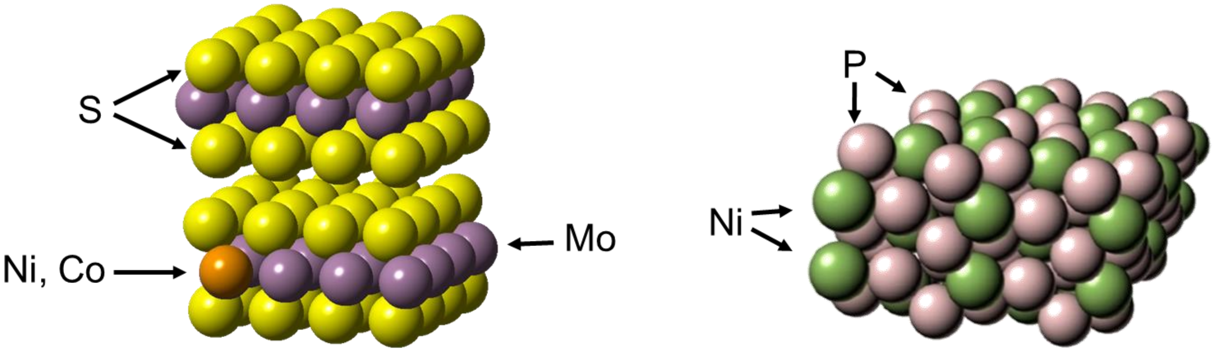

Figure 1.5. Structures of a conventional $Co(Ni)-MoS_s/Al_2O_3$ catalyst (left) and a Ni_2P catalyst phase (right).

Because of their sulfur tolerance, transition metal phosphides are able to remain active and work in tandem with the molybdenum-sulfide catalysts. A good example of this combined utilization would rely on conventional, molybdenum-sulfide based catalysts being used to perform HDS on lighter organosulfur compounds such as thiophene or benzothiophene, and a transition metal phosphide catalyst to perform the deep HDS of the more refractory compounds such as 4,6-dimethyldibeznothiphene.[1]

Nickel phosphide (Ni_2P) has been the subject of much research regarding its ability to perform HDS and has been shown to be the most active transition metal phosphide phase outside of certain noble metal phosphides (e.g. Rh_2P).[16] Bulk Ni_2P adopts a hexagonal unit cell composed of two layers, Ni_3P and Ni_3P_2, that alternate to reveal an overall stoichiometric Ni_2P phase, as shown in Figure 1.5 below.[19-20]

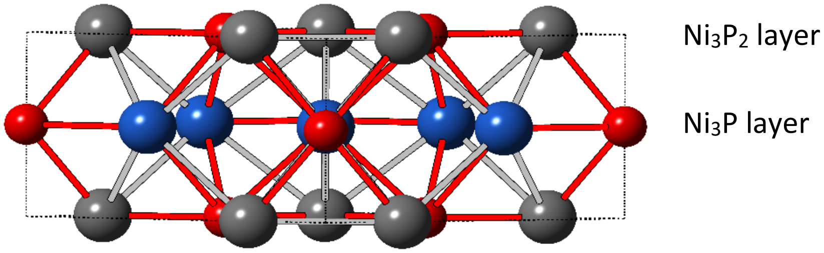

Figure 1.6. Structure of Ni_2P showing the alternating layers of Ni_3P_2 and Ni_3P. Grey (tetrahedral sites) and blue (pyramidal sites) represent Ni atoms while red represents P atoms.[21]

Studies have shown that of the two layers that compose the Ni_2P phase, the Ni_3P_2 layer is the more thermodynamically stable and as such results in Ni_2P particles predominately being terminated by the Ni_3P_2 layer.[22-23] The presence of phosphorus creates distance between Ni atoms that results in a dilution of Ni atoms at the surface of Ni_2P particles. This dilution of Ni atoms contributes to the sulfur tolerance be retarding how strongly sulfur atoms can interact with exposed Ni sites.[16,24]

The inclusion of a second metal can have significant influence upon a metal phosphide's catalytic properties. A study by the Oyama group incorporated Fe into a Ni_2P phase supported on silica. The results showed little difference in HDS activity between Ni_2P/SiO_2 and $Fe_xNi_{2-x}P/SiO_2$ catalysts, but a dramatic shift in the HDS product selectivity was observed for the bimetallic phosphides catalysts (e.g. $Fe_{1.0}Ni_{1.0}P/SiO_2$) which favored the DDS pathway while the Ni_2P/SiO_2 catalyst favored the HYD pathway.[24] Abu and Smith conducted a study probing the effect of incorporating 3.3 mol% and 2.5 mol% Co into unsupported MoP and Ni_2P catalysts respectively in regards to the HDS of 4,6-DMDBT. The results showed an increase in selectivity via the DDS pathway for $Co_{0.07}MoP$ and $Co_{0.08}Ni_2P$; in the case of the latter, the conversion of

4,6-DMDBT was observed to increase by 50% relative to the Ni_2P catalyst. The study suggested that the addition of the Co increased the Brønsted aciditiy of the active sites while decreasing the overall availability of metal sites based on chemisorption studies using *n*-propylamine and CO, respectively.[26] The Bussell group previously demonstrated the influence a second metal can have upon the HDS properties of metal phosphide catalysts by synthesizing a series of $Ni_{2-x}Co_xP/SiO_2$ catalysts ($0 \leq x \leq 2.00$). Of the series, the most HDS active catalyst was $Ni_{1.92}Co_{0.08}P_{2.00}/SiO_2$, which was 34% more active than that of a $Ni_{2.00}P_{1.60}/SiO_2$ catalyst. The study showed that there was an enrichment of P at the surface of the Ni-rich catalysts, compared to the $Ni_{2.00}P_{1.60}/SiO_2$ and $Co_{2.00}P_{1.00}/SiO_2$ catalysts, that led to an increased sulfur tolerance as observed with HDS x-ray photoelectron spectroscopy measurements. The increase in HDS activity was attributed to the enrichment of P as a means of increasing the overall sulfur tolerance of the bimetallic phosphide catalysts.[27]

1.5 Thesis Research Goals

The goal of this research is develop a better understanding of how bimetallic phosphides can be tailored, to achieve the deep HDS of refractory, organosulfur compounds found in petroleum, in an effort to reach ultralow sulfur content transportation fuels. Two series of bimetallic phosphides, $Ni_{2-x}M_xP/SiO_2$ (where $0 \leq x \leq 2$ and M = Ru or Rh), were investigated for their ability to perform HDS of 4,6-DMDBT with the goal of identifying compositions that result in optimized catalytic phases that offer high HDS activities and favorable product selectivities. Each catalyst composition was characterized using X-ray diffraction (XRD), energy dispersive X-ray analysis (EDX), X-ray photoelectron spectroscopy (XPS), surface area analysis using the BET method, and CO chemisorption.

2. Experimental Methods

2.1 Reagents

All reagents were used as received with the exceptions of the fumed silica (SiO_2) support material and all gases used in synthesis and characterization. Prior to use the silica support [CAB-O-SIL, EH-5, 99.0%, 200 m^2/g] was calcined by heating to 773 K for 3 h in air; the calcined silica was then stored at 393 K. Helium and H_2 gases (Airgas, 99.999%) were purified using molecular sieve (Alltech) and oxygen purification (Oxyclear) traps. The 1 mol% O_2/He mixture (Airgas, 1.001/98.999 mol% O_2/He) used for catalyst passivation was purified using a molecular sieve (Alltech) trap.

2.2 Catalyst Synthesis

$Ni_{1.00}Ru_{1.00}P/SiO_2$ Synthesis

Calcined silica was placed in a 300 mL beaker and kept at 343 K prior to use. Hypophosphorus acid (H_3PO_2, 0.3517 g, Sigma-Aldrich, 50 wt% in H_2O) was weighed into a 20 mL beaker, to which ruthenium (III) chloride trihydrate ($RuCl_3{\cdot}3H_2O$, 0.4838 g, Pressure Chemical Co.) and nickel (II) nitrate hexahydrate ($Ni(NO_3)_2{\cdot}6H_2O$, 0.5381 g, Alfa Aesar, ACS, 99%) were added. Approximately 3 mL of water were added to the beaker to aid in dissolving the solids, resulting in a dark brown solution. The solution (~5 mL) was then impregnated onto the support until incipient wetness was reached. The precursor was allowed to dry for 60 min between impregnations. The beaker was then rinsed with ~3 mL of water and the rinse solution was then impregnated onto the support. The impregnated supports were allowed to dry for 24 h at 343 k. The precursor was then reduced via temperature programmed reduction (TPR) at 773 K and passivated in flowing 1 mol% O_2/He to produce a 15 wt% $Ni_{1.0}Ru_{1.0}P/SiO_2$ catalyst (P/M = 0.72). The purity of the resulting catalyst was assessed using X-ray diffraction.

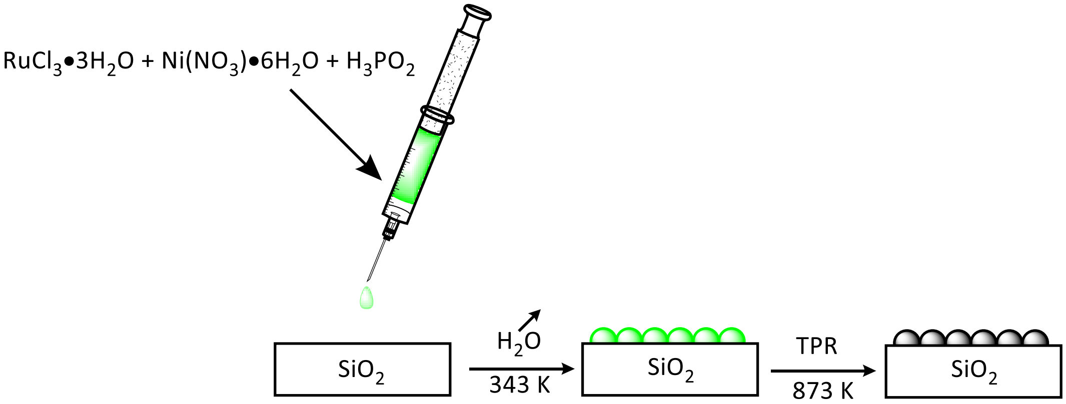

Figure 2.1: Process for $Ni_xRu_{2-x}P/SiO_2$ catalyst synthesis.

$Ni_{1.00}Rh_{1.00}P/SiO_2$ Synthesis

Calcined silica was placed in a 300 mL beaker and kept at 343 K prior to use. Hypophosphorus acid (H_3PO_2, 0.3484 g) was weighed into a 20 mL beaker, to which rhodium (III) chloride trihydrate ($RhCl_3 \cdot 2.66H_2O$, 0.4715 g, Pressure Chemical Co.) and nickel (II) nitrate hexahydrate (0.5330 g) were added. Approximately 3 mL of water were added to the beaker to aid dissolving the solids into solution (dark brown). The solution (~5 mL) was then impregnated onto the support until incipient wetness was reached. The precursor was allowed to dry for 60 min between impregnations. The beaker was then rinsed with ~3 mL of water and the rinse solution was then impregnated onto the support. The impregnated supports were allowed to dry for 24 h at 343 k. The precursor was then reduced via (TPR) at 773 K and passivated in flowing 1 mol% O_2/He (60 mL/min) to give a 15 wt% $Ni_{1.0}Rh_{1.0}P/SiO_2$ catalyst (P/M = 0.72). The purity of the resulting catalyst was assessed using X-ray diffraction.

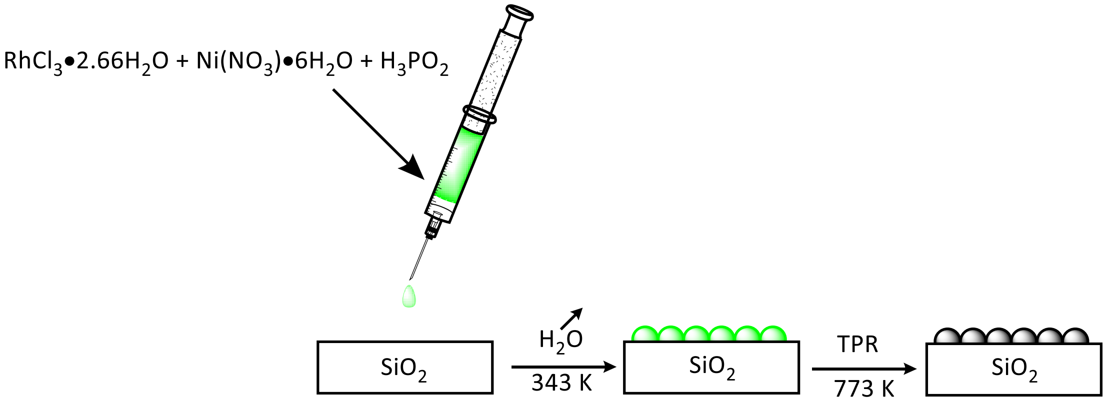

Figure 2.2: Process for $Ni_xRh_{2-x}P/SiO_2$ catalyst synthesis.

$Ni_xM_{2-x}P/SiO_2$ Synthesis

The full series of $Ni_xM_{2-x}P/SiO_2$ catalysts (M = Ru or Rh, $0 \le x \le 2$), were prepared following the steps outlined above and by adjusting the amounts of the metal salt precursors that were used in each catalyst synthesis. The quantities used for the $Ni_xRu_{2-}xP/SiO_2$ series are listed below in Table 2.1 and the quantities used for the $Ni_xRh_{2-x}P/SiO_2$ series are listed below in Table 2.2. For both series, hypophosphorus acid was used as the phosphorus source with a phosphorus-to-metal (P/M) mole ratio of P/M = 0.72.

Table 2.1: Reagent masses for the $Ni_xRu_{2-x}P/SiO_2$ catalysts (15 wt%).

Catalyst	Phosphorous to Metal Ratio	SiO_2 (g)	$Ni(NO_3)_2{\cdot}6H_2O$ (g)	$RuCl_3{\cdot}3H_2O$ (g)	H_3PO_2 (g)*
$Ni_{2.0}P/SiO_2$	0.72	1.0000	0.6915	- - - -	0.2259
$Ni_{1.93}Ru_{0.07}P/SiO_2$	0.72	1.0000	0.6716	0.0115	0.2236
$Ni_{1.88}Ru_{0.12}P/SiO_2$	0.72	1.0000	0.6325	0.0339	0.1816
$Ni_{1.85}Ru_{0.15}P/SiO_2$	0.72	2.0000	1.2133	0.8840	0.4284
$Ni_{1.80}Ru_{0.20}P/SiO_2$	0.72	1.0000	0.5890	0.0588	0.2139
$Ni_{1.75}Ru_{0.25}P/SiO_2$	0.72	2.0000	1.1299	0.1451	0.4220
$Ni_{1.65}Ru_{0.35}P/SiO_2$	0.72	1.0000	0.5077	0.1053	0.2042
$Ni_{1.50}Ru_{0.50}P/SiO_2$	0.72	1.9324	0.8771	0.2643	0.3822
$Ni_{1.25}Ru_{0.75}P/SiO_2$	0.72	1.0946	0.3897	0.2102	0.2830
$Ni_{1.00}Ru_{1.00}P/SiO_2$	0.72	1.9982	0.5376	0.4834	0.3514
$Ni_{0.75}Ru_{1.25}P/SiO_2$	0.72	1.9329	0.3695	0.5537	0.3222
$Ni_{0.50}Ru_{1.50}P/SiO_2$	0.72	2.0101	0.3414	0.6140	0.3347
$Ni_{0.25}Ru_{1.75}P/SiO_2$	0.72	1.9600	0.1159	0.7294	0.3030
$Ru_{2.00}P/SiO_2$	0.72	2.1032	- - - -	0.8326	0.3026

* 50 wt% H_3PO_2 in water

Table 2.2: Reagent masses for the $Ni_xRh_{2-x}P/SiO_2$ catalysts (15 wt%).

Catalyst	**Phosphorous to Metal Ratio**	**SiO_2 (g)**	**$Ni(NO_3)_2·6H_2O$ (g)**	**$RhCl_3·2.66H_2O$ (g)**	**H_3PO_2 (g)***
$Ni_{2.0}P/SiO_2$	0.72	1.0000	0.6915	- - - -	0.2259
$Ni_{1.85}Rh_{0.15}P/SiO_2$	0.72	1.0000	0.6123	0.0439	0.2164
$Ni_{1.75}Rh_{0.25}P/SiO_2$	0.72	1.0000	0.5633	0.7119	0.2105
$Ni_{1.50}Rh_{0.50}P/SiO_2$	0.72	1.0000	0.4514	0.1331	0.1967
$Ni_{1.25}Rh_{0.75}P/SiO_2$	0.72	1.0000	0.3534	0.1890	0.1848
$Ni_{1.00}Rh_{1.00}P/SiO_2$	0.72	1.0000	0.2663	0.2358	0.142
$Ni_{0.75}Rh_{1.25}P/SiO_2$	0.72	1.0000	0.1890	0.2787	0.1647
$Ni_{0.50}Rh_{1.50}P/SiO_2$	0.72	1.0000	0.1195	0.3172	0.1562
$Ni_{0.25}Rh_{1.75}P/SiO_2$	0.72	1.0000	0.0568	0.3519	0.1489
$Rh_{2.0}P/SiO_2$	0.72	1.0000	- - - -	0.3834	0.1416

* 50 wt% in water

2.2.1 Temperature programmed reduction

Following impregnation and drying, ~0.25 g of a catalyst precursor was loaded into a quartz U-tube. A bed of quartz wool was used as a plug to keep the precursor in place. The U-tube was placed in a furnace equipped with a temperature controller (Watlow Series 981). The U-tube was purged with He (99.9999%, 60 mL/min) for 30 min. Following the He purge, H_2 (99.999%, 100 mL/min) was set to flow over the precursor as the temperature was increased at a rate of 5 K/min. A final temperature of 773 K was reached and then held for 1 h while maintaining the H_2 flow. The exhaust was routed through a MKS Cirrus 2 mass spectrometer to observe the evolution of water during reduction. The U-tube was allowed to cool to room temperature and the flow was switched from H_2 to He (60 mL/min). Following the He purge, the reduced catalyst was passivated by flowing a 1 mol% O_2/He (60 mL/min) mixture over the sample; this created a thin oxide layer on the metal phosphide particles which rendered the catalysts to be air stable. The passivation layer was removed via H_2 reduction at 673 K prior to any characterization or HDS testing measurements. The synthesis reactor for this process is illustrated below in Figure 2.3.

2.3 X-ray Diffraction

Powder X-ray diffraction (XRD) patterns of the catalysts prepared in this research were obtained using a PANalytical X'Pert Pro MRD X-ray diffractometer outfitted with a monochromatic Cu K_α source with a wavelength (λ) of 0.1542 nm and operated at a voltage of 45 kV and a current of 40 mA. Catalyst samples were mounted onto glass slides by saturating ~0.05 g of catalyst with methanol, depositing the suspension on the surface of the slide,

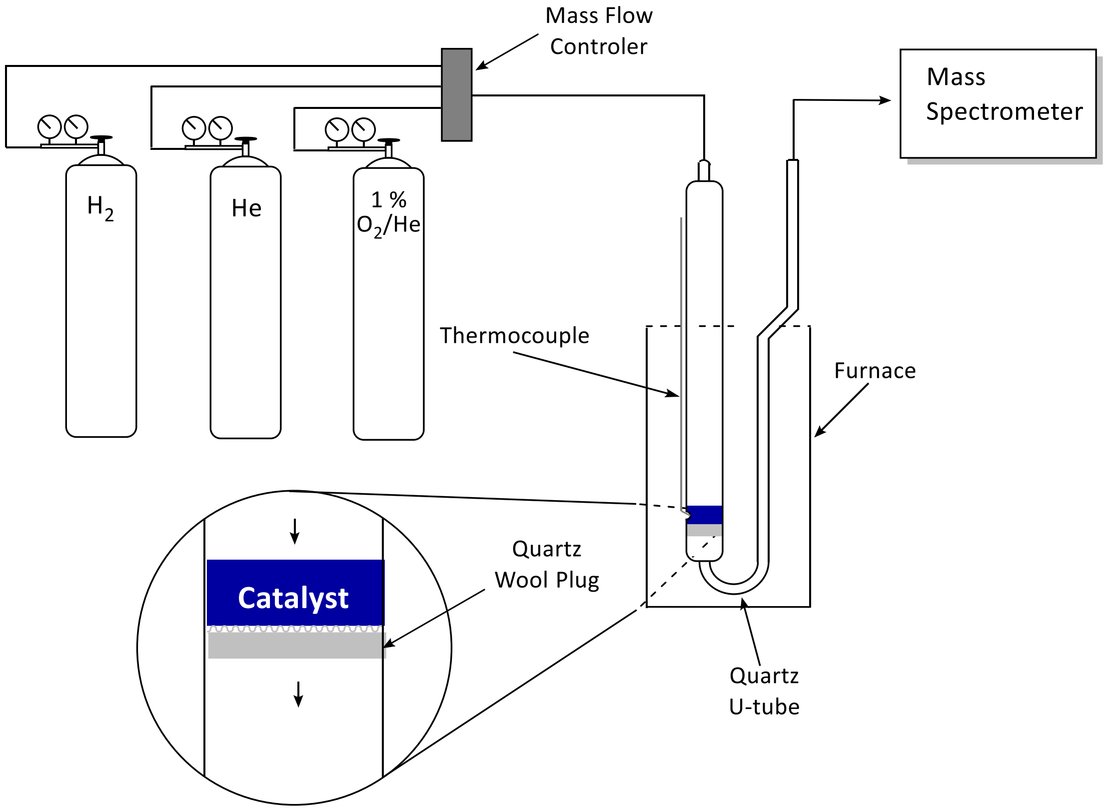

Figure 2.3: Schematic of the temperature programmed reduction setup used.

evaporating the methanol, and then tapping the slide to remove any loose sample. In order to maintain random orientations of the particles, the sample was not pressed onto the slide. XRD patterns were collected over a Bragg angle (2θ) range of 30-60° with a step size of 0.015° and a dwell time of 25 s. Data analysis was carried out using the X'Pert HighScore Plus software and reference patterns were taken from the JCPDS powder diffraction database. Crystallographic information files (CIFs) were acquired from the Pearson Crystal Database.[9,10] Average crystallite sizes were calculated using the Scherrer equation (2.1).

$$D_c = \frac{K\lambda}{\beta cos\theta} \qquad 2.1$$

The following parameters were used for the Scherrer equation calculations: K=1 (assuming spherical particles), λ = the wavelength of the incident X-rays (0.1542 nm), β = the width of peak at half maximum in radians, and θ = the Bragg angle of the selected peak.

2.4 Surface Area Analysis

The surface areas and pore size distributions of both the $Ni_xRu_{2-x}P/SiO_2$ and $Ni_xRh_{2-x}P/SiO_2$ catalysts were determined using an ASAP 2020 surface area and porosimetry analyzer with N_2 as the probe gas. Approximately 0.10 g of a catalyst was placed into a sample tube that had previously been dried at 373 K. The sample tube was attached to the degas port with a heating mantle clamped onto the bottom of the sample tube. The sample was degassed by ramping the temperature to 523 K at a rate of 5 K/min. Once this temperature was reached, it was held for 8 h. After the sample was degassed, it was weighed and transferred to the physisorb port. The sample tube was evacuated to 0.067 kPa at which point N_2 was dosed into the sample tube at a specific mole-to-sample mass ratio of 0.13384 mmol/g. The relative pressure ($P/P_\circ$) was set at nine intervals in the range 0.020-0.100. For each relative pressure, the amount of adsorbed N_2 was measured. The amount of desorbed N_2 was measured as the relative pressure was held at intervals between 0.989-0.240 $P/P_\circ$. The surface area was analyzed using the Brunauer-Emmett-Teller (BET) method and the pore size distribution was analyzed using the Barrett-Joyner-Halenda (BJH) method.

2.4.1 Theory and Calculations

According to the BET method, multiple adsorption layers will form as N_2 interacts with a sample. The BET method also assumes that these adsorbing N_2 layers do not interact with each other and that each layer follows the Langmuir adsorption model. Using these assumptions, the BET method yields Equation 2.2.

$$\frac{1}{V_a\left(\frac{P_O}{P}-1\right)} = \frac{C-1}{V_m C}\left(\frac{P}{P_\circ}\right) + \frac{1}{V_m C} \qquad 2.2$$

The variables in Equation 2.2 are as follows; V_a is the total volume of adsorbed N_2, P_O/P is the relative pressure measured during the analysis, C is a constant that is determined by the adsorbate used, and V_m is the volume of the monolayer of adsorbed N_2.

When plotting the left-hand side of Equation 2.2 vs. the relative pressure, a linear relationship is observed which can be used to calculated the slope, *m*, (Equation 2.3) and the intercept, *b*, (Equation 2.4).

$$m = \frac{C-1}{V_m C} \quad 2.3$$

$$b = \frac{1}{V_m C} \quad 2.4$$

These values were used to determine the BET constant, C, and the volume of the monolayer, V_m. Once the volume of the monolayer was known, the ideal gas law was used to determine the number of moles of N_2 that constituted the monolayer volume. The number of moles was used to determine the number of N_2 molecules in the monolayer. Knowing the molecules in the monolayer and the sample mass and the known cross sectional area of an N_2 molecule (0.162 nm^2/molecule), the surface area (m^2/g) was calculated.

The BJH method assumes that when the relative pressure is near unity ($P/P_o \approx 1$), all the pores are filled with N_2. The volume of adsorbed nitrogen in the pores (V_{liq}) can be related to the total volume of adsorbed nitrogen (V_a) in Equation 2.5.

$$V_{liq} = \frac{P_a V_a V_{N_2}}{RT} \quad 2.5$$

In Equation 2.5, P_a denotes the ambient pressure, T is the ambient temperature, V_{N_2} is the molar volume of a N_2 molecule, and R is the universal gas constant. By relating the volume of nitrogen that filled the pores, the average pore size can be determined (Equation 2.6) assuming a cylindrical pore geometry.

$$r_p = \frac{2V_{liq}}{S_{BET}} \quad 2.6$$

2.5 CO Chemisorption

Carbon monoxide chemisorption measurements were carried out using a Micromeritics Autochem 2950 HP instrument. The measurements were performed using a 10.00 mol% CO/He gas mixture(10.00%/90.00%, Praxair). Approximately 50 mg catalyst was placed in a metal U-tube and reduced to remove the passivation layer. The sample was degassed at 333 K for 1 h under Ar (10.00%, Praxair) flow at 60 mL/min, following which the temperature was ramped to 673 K at 10 K/min under a flow of 10 mol% H_2/Ar (10.00%, Praxair) at 60 mL/min. The temperature was held at 673 K with continued 10 mol% H_2/Ar flow for 1 h. The sample was then purged with He and cooled to 273 K. Pulses of a 10.00 mol% CO/He gas mixture were passed over the sample tube in 1 mL volumes. A thermal conductivity detector (TCD) was used to measure the amount of CO exiting the sample tube. The pulses continued until the TCD measured no increase in peak area of exiting CO, indicating that the sample was fully saturated with CO. The CO was removed from the sample by temperature programmed desorption (TPD) by flowing He through the sample tube at a temperature of 623 K.

2.6 X-Ray Photoelectron Spectroscopy

X-ray photoelectron spectroscopy (XPS) was performed on the $Ni_xM_{2-x}P/SiO_2$ catalysts using a Surface Physics M-Probe ESCA spectrometer equipped with a monochromatic Al K_α source (1486.6 eV) and using a takeoff angle of 55°. Catalyst samples were pressed into pellets at 10,000 psi and placed on a copper plate using double-sided tape. The copper plate was mounted onto a sample stage that was placed in an ultra-high vacuum chamber. XPS spectra were collected in the range of $1.0\text{-}5.0\times10^{-9}$ torr. For each sample, a survey scan was collected along with high resolution scans of the regions of interest; Ni $2p_{3/2}$, Ru $3d_{5/2}$, Ru $3p_{3/2}$, Rh $3d_{5/2}$, Rh $3p_{3/2}$, P $2p_{3/2}$, Si $2p_{3/2}$. The scan parameters are outlined below in Table 2.4.

Table 2.4: Scan parameters for XPS analysis of the $Ni_xM_{2-x}P/SiO_2$ catalysts.

Region	**Center (eV)**	**Region Width (eV)**	**Spot Size (μm)**	**Scans**	**Step size (ev)**	**Time per step (s)**
Survey	500	1000	800	10	0.5	100
Ni $2p_{3/2}$	860	60	400	350-700	0.1	100-250
Ru $3d_{5/2}$	283	36	400	325	0.1	100
Ru $3p_{3/2}$	470	40	400	325-500	0.1	100-250
Rh $3d_{5/2}$	310	40	400	325	0.1	100
Rh $3p_{3/2}$	520	40	400	325-500	0.1	100-250
P $2p_{3/2}$	130	24	400	325	0.1	100
Si $2p_{3/2}$	100	20	400	325	0.1	100
O 1s	532	20	400	325	0.1	100

A mesh screen over the samples along with a low-voltage electron beam were used to minimize sample charging using a current of 1.2 A and a bias voltage of 7 V. The XPS spectra $Ni_xRh_{2-x}P/SiO_2$ catalysts were corrected using the C 1s peak at 284.6 eV while the XPS spectra of the $Ni_xRu_{2-x}P/SiO_2$ catalysts were corrected using the Si 2p peak at 103.3 eV. All data were analyzed using Casa XPS software (ver. 2.3.16 PR1.6).

2.7 Energy-Dispersive X-ray spectroscopy

Scanning electron microscopy-energy-dispersive X-ray spectroscopy (SEM-EDX) was used to determine the elemental composition of the prepared catalysts. A Vega TS 5136MM scanning electron microscope outfitted with an EDAX energy dispersive X-ray analysis system and a retractable backscatter detector (BSE) was used for these measurements. The EDX analysis was performed using a 15 kV electron beam. Catalyst samples were prepared for analysis by loading ~50 mg of catalyst into a pellet die and pressing at 10,000 psi; the resulting wafer was then mounted to an SEM sample standoff using a piece of double-sided carbon tape. Prior to analysis, the catalyst samples were sputter-coated for 30 s with a mixture of Pd and Au in order to ensure sample conductivity. Elemental compositions were determined by averaging EDX spectra from three sampling areas on each pellet. Elemental compositions were normalized to P on a mole basis.

2.8 Carbon and Sulfur Analysis

Carbon and sulfur analyses of HDS-tested catalyst samples were performed using a LECO SC-144DR Sulfur and Carbon Analyzer at the Phillips 66 Refinery in Ferndale, WA. Approximately 0.1 g of a tested catalyst sample was placed into a ceramic boat, which was then loaded into a furnace where the sample was combusted in an oxygen-rich environment at ~1625 K for 3 min. Combusted carbon (CO_2) and sulfur (SO_2) that evolved from the catalyst sample were quantified via IR detection and reported as wt% C and S.

2.9 Hydrodesulfurization Reactor

HDS measurements were carried out using two custom-built, high-pressure, continuous flow reactor systems. Each reactor consisted of a stainless steel tube, 11.2 mm in diameter, which was purchased from Autoclave Engineers. The reactor was equipped with two inlets at the top, one supplied gaseous flow (H_2) while the second was for the liquid feed. A series I metering HPLC pump was used to introduce the liquid feed to the top of the reactor. Once introduced into the reactor, the liquid feed was vaporized by flowing through a length of tubing wrapped with heat tape set to 473 K. The gas flow was controlled via a Brooks Model 5850S mass flow controller that was operated using computer control. A total pressure of 3.0 MPa was maintained by a back pressure regulator (Swagelok). The two reactor systems ran in tandem, each using a 2000 W clamshell furnace (Watlow). The temperature was measured using an type K thermocouple (Omega) mounted coaxially in the reactor tube and in direct contact with the catalyst bed.

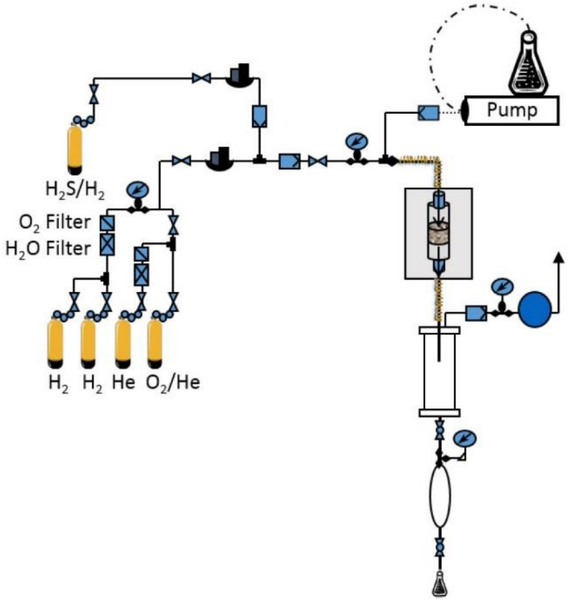

Figure 2.4: Reactor system used for HDS measurements.

Catalyst samples were prepared as follows for the reactor studies. Powdered catalyst was pressed at 7,000 psi to form pellets 1 cm in diameter. Each pellet was forced through a sieve mesh with 1.18 mm openings and caught by a second sieve mesh with 0.85 mm openings. Those pieces that did not fall through the smaller sieve were used in the reactor studies. A mass of ~0.1500 g of sieved catalyst was collected, and diluted with ~0.85 mm quartz chips to fill a volume of 5 mL. The diluted catalyst was placed between two 15 mL volumes of Pyrex beads.

Quartz wool was used to separate the beads and the diluted catalyst and to ensure that no movement of the catalyst bed occurred during testing. Once the catalyst was loaded into the reactor tube, a pretreatment was carried out. Samples were purged with 60 mL/min He for 30 min and then reduced in 60 mL/min of H_2 at 101.3 Pa, with heating from room temperature to a final temperature of 650 K over 1 h followed by a 2 h soak period. After cooling to room temperature, the hydrogen pressure was increased to 3.0 MPa and the catalyst then heated to 513 or 533 K. Once the temperature was stabilized, the model feed was allowed to flow into the reactor at a rate of 0.09 mL/min, with no sampling over the first 10 h. Each reactor was allowed to stabilize for a minimum of 3 h after a temperature change. Effluent was allowed to flow into a secondary chamber to cool before it was collected, in ~ 3 mL volumes, four times at 30 min intervals at each reactor temperature. The model feed consisted of 1,000 ppm 4,6-dimethyldibenzothiphene (4,6-DMDBT, $C_{14}H_{12}S$, Alfa Aesar, 97%) dissolved in 1 L of decahydronaphthalene ($C_{10}H_{18}$, Alfa Aesar, cis + trans, 98%). An internal standard, 500 ppm of dodecane ($C_{12}H_{26}$, Alfa Aesar, 99+%), was used for GC analysis.

An Agilent 6890N GC with a 763b auto-sampling system, a flame ionization detector (FID), and a HP-5 (Agilent, 5% Phenyl-methylpolysiloxane) GC column was used for off-line analysis of the reactor effluent. Helium (Airgas, 99.999%) was used as the carrier gas and the split injection had a ratio of 39.9:1 and a total flow of 108.5 mL/min with a 3 µL injection volume. The initial column temperature was set to 398 K followed by a ramp to 418 k, at a rate of 10 k/min, at which the temperature was held for 2 min. The column temperature was then ramped to 523 k at 15 k/min with no hold time. Each run totaled 11.33 min.

To measure HDS activity and selectivity, the reactor temperature ranged from 513-653 K, in 20 K increments, while keeping the weight time constant. Reactor weight time (τ) was defined as the mass of the catalyst divided by the molar flow of reactants as shown below in Equation 2.5.

$$\tau = \frac{g_{cat}}{n_{feed}} \qquad 2.5$$

In Equation 2.5, n_{feed} is defined as the flow of the model feed plus the flow of H_2 gas, and g_{cat} is the mass of catalyst used. For all measurements taken, the weight time was kept at 0.75 g*min/mol. The HDS activity was defined as moles of 4,6-DMDBT converted to hydrocarbon products per unit time divided by the mass of the catalyst used as given in Equation 2.6.

$$\text{HDS activity} = \frac{nmol}{g_{cat} \cdot s} \qquad 2.6$$

Catalyst selectivity was determined by taking the total moles of the products, listed in Figure 2.5, and subtracting them from the moles of starting material and normalizing to 100%. The HDS products, 3,3-DMBP, 3,3-DMBCH, 3,3-DMCHB, where those that resulted in a loss of sulfur atom; while TH-4,6-DMDBT was a non-HDS product that was observed due to the hydrogenation of a benzene ring.

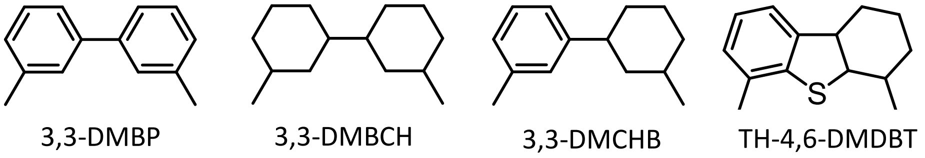

Figure 2.5: Products identified in the reactor effluent and used for product selectivity calculations: 3,3-dimethylbiphenyl (3,3'-DMBP), 3,3-dimethylbicyclohexane (3,3'-DMBCH), 3,3-dimethylcyclohexylbenzene (3,3', and tetrahydro-4,6-dimethyldibenzothiophene.

The peak areas for the 4,6-DMDBT and products were determined by gas chromatography (GC) analysis. The *cis* and *trans* decahydronaphthalene isomer peaks appeared at 2.31 and 2.09 min/ respectively. Figure 2.6 shows the GC traces of reference samples for the major products (3,3'-DMCHB isomers and 3,3'-DMBP) along with the 4,6-DMDBT starting material.

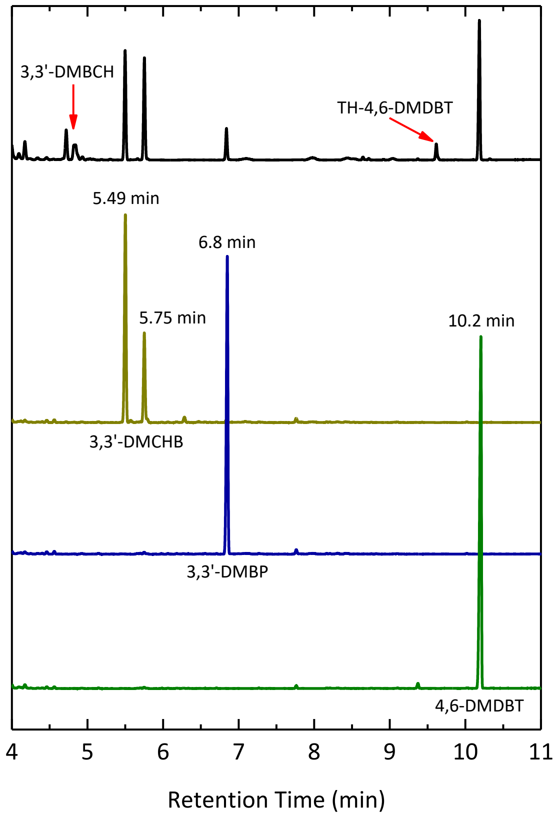

Figure 2.6: GC analysis showing peaks for the starting materials and HDS products.

The peaks for the internal standard, dodecane, appeared at 2.54 min. Because reference samples of 3,3'-DMBCH and TH-4,6-DMDBT were not available, these product peaks were identified using GC-MS. Supplementary peak identification for 3,3-DMBCH and TH-4,6-DMDBT was carried out using molecular ion and fragment analysis. A Varian GC-MS composed of a CP3800 GC and Saturn 2000 Ion Trap mass spectrometer was used for these peak assignments.

For 3,3-DMBCH, retention times of 4.7 and 4.8 min were found for the *trans* and *cis* isomers, respectively, and 9.6 min for TH-4,6-DMDBT.

Ten-point calibration curves of the starting material, 4,6-DMDBT, and major products, 3,3-DMCHB and 3,3-DMBP, were used for product quantification. A series of ten solutions was made by serial diluting a stock solution, 1000 ppm 4,6-DMDBT with 500 ppm of both 3,3-DMCHB and 3,3-DMBP, by 10% with a blank solution of decahydronaphthalene and 500 ppm of dodecane. Response factors for each analyte were calculated using Equation 2.7 below.

$$\text{response factor} = \frac{\frac{peak\ area\ of\ analyte}{peak\ area\ of\ dodecane}}{concentration\ of\ analyte} \qquad 2.7$$

The peak area of the analyte was divided by the peak area of the dodecane, and plotted as a

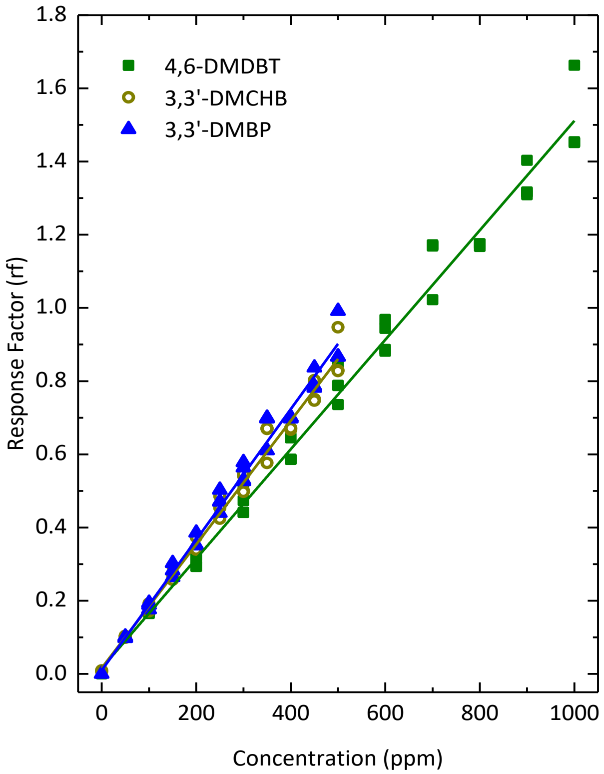

Figure 2.7: GC analysis peaks for starting materials and HDS products.

function of concentration as shown in Figure 2.7. A linear fit was applied and the analyte response factors were determined by the slope of the fit; these results are displayed in Table 2.5.

Table 2.5: Retention times and response factors of major products in 4,6-DMDBT HDS.

Analyte	Retention Time (min)	Response Factor (rf)
3,3’-DMBCH	4.7 & 4.8	0.00169
3,3’-DMCHB	5.5 & 5.7	0.00169
3,3'-DMBP	6.8	0.00178
4H-DMDBT	9.6	0.00150
4,6-DMDBT	10.2	0.00150

3. Results

3.1 Characterization Methods

The catalysts prepared in this research were examined using powder X-ray diffraction (XRD) to determine the crystalline phases present by comparing the diffraction patterns of the synthesized catalysts with reference patterns from the JCPDS database.[28] From the diffraction patterns measured, the Scherrer equation was used to calculate average crystallite sizes. X-ray photoelectron spectroscopy (XPS) was used to determine the elemental composition at the surface of the catalysts as well as to provide information regarding the chemical states of the elements as the catalyst composition changed throughout a series. To complement the compositional result determined using the XPS, energy-dispersive X-ray spectroscopy (EDX) was also used to measure elemental composition in the near surface region of the catalysts. The surface areas and average pore sizes of the catalysts were measured using nitrogen adsorption and the Brunauer-Emmett-Teller (BET) and Barrett-Joyner-Halenda (BJH) methods. Carbon monoxide chemisorption was used to the measure active site densities of the catalysts. Hydrodesulfurization (HDS) measurements were carried out to determine catalyst conversions and product selectivities. Finally, carbon and sulfur analysis was used on post-HDS samples to determine the carbon and sulfur contents of the tested catalysts.

3.1.1 X-ray Diffraction Analysis

Ni_2P/SiO_2 Catalyst Figure 3.1 shows the X-ray diffraction pattern for a synthesized 15 wt% Ni_2P/SiO_2 catalyst. The XRD pattern matches well with a Ni_2P reference pattern (card no. 03-065-1989) from the JCPDS database and there is no evidence of impurity phases such as

$Ni_{12}P_5$ or Ni_5P_4, indicating that phase pure Ni_2P was synthesized.[36] The average Ni_2P crystallite size (~5 nm) of the 15 wt% Ni_2P/SiO_2 catalyst was calculated using the Scherrer equation and the peak at 40.7° corresponding to the {111} reflection. An XRD pattern of the Ni_2P/SiO_2 catalyst was acquired after HDS testing to determine if sintering occurred during HDS testing (T = 513-613K, ~95 hrs) . The slight increase in average Ni_2P crystallite size suggests that a small amount of sintering did occur during HDS testing.

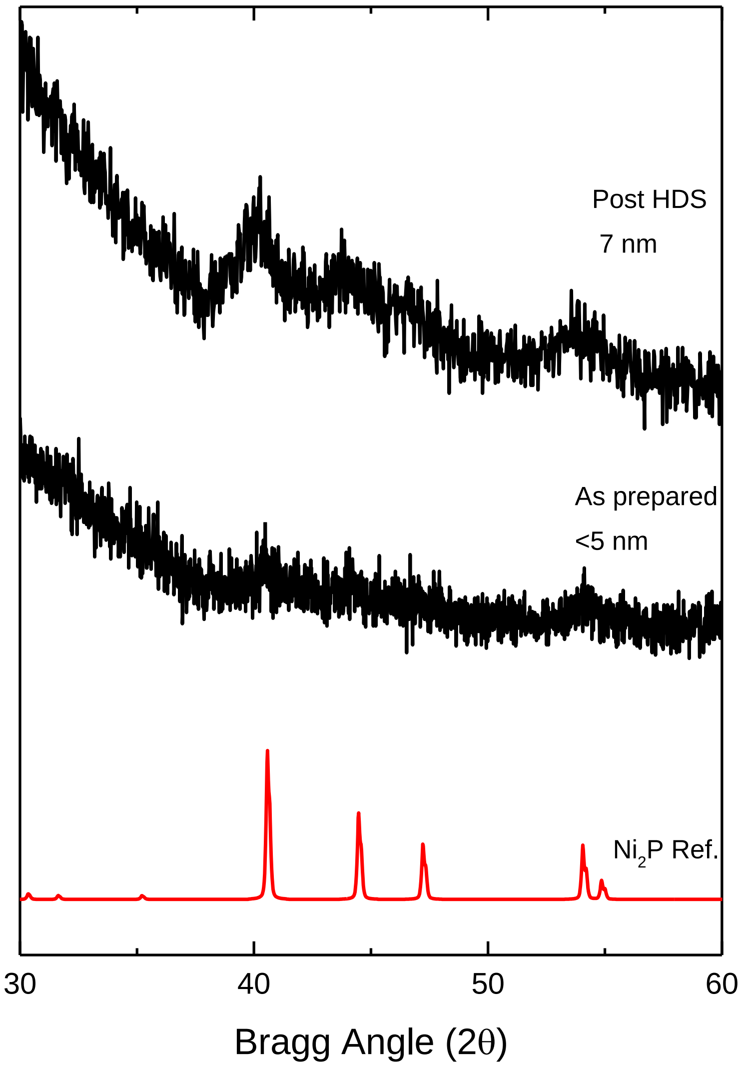

Figure 3.1: X-ray diffraction patterns of as-prepared 15 wt% Ni_2P/SiO_2 catalyst compared to the HDS tested catalyst.

Ru_2P/SiO_2 Catalyst

Attempts to synthesize 15 wt% Ru_2P/SiO_2 at a P/M = 0.72 resulted in a mixed phase catalyst consisting of both Ru and Ru_2P phases. As seen in Figure 3.2, phase pure Ru_2P/SiO_2 was achieved by increasing the phosphorus-to-metal ratio to P/Ru = 0.90. At ratios above P/Ru = 1.10, RuP was observed in addition to Ru_2P.

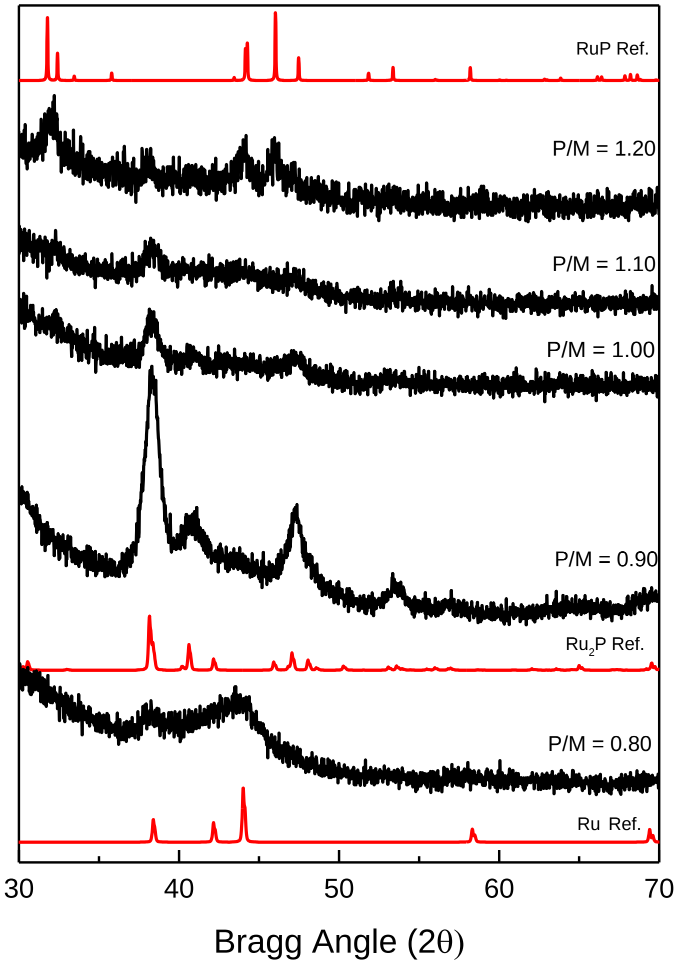

Figure 3.2: XRD patterns showing the evolution of Ru phases in Ru_2P/SiO_2 catalyst as the P/Ru ratio is increased.

Figure 3.3 shows the X-ray diffraction pattern for an as-prepared 15 wt% Ru_2P/SiO_2 (P/M = 1.00) catalyst. The diffraction pattern compares well with a Ru_2P reference pattern (card no. 96-900-9204) from the JCPDS database as well as published work by the Bussell group that investigated Ru_2P/SiO_2 for its hydrodeoxygenation (HDO) and HDS properties.[24-26] The average Ru_2P crystallite size (9 nm) for the 15 wt% Ru_2P/SiO_2 catalyst was calculated using the Scherrer equation and the peak at 38.4^o corresponding to the {112} reflection. An XRD pattern of the Ru_2P/SiO_2 catalyst was acquired after HDS testing and a slight increase in the average crystallite size was determined, but with no evidence for loss of phase purity. This suggests some sintering occurred during HDS testing at 533-653 K.

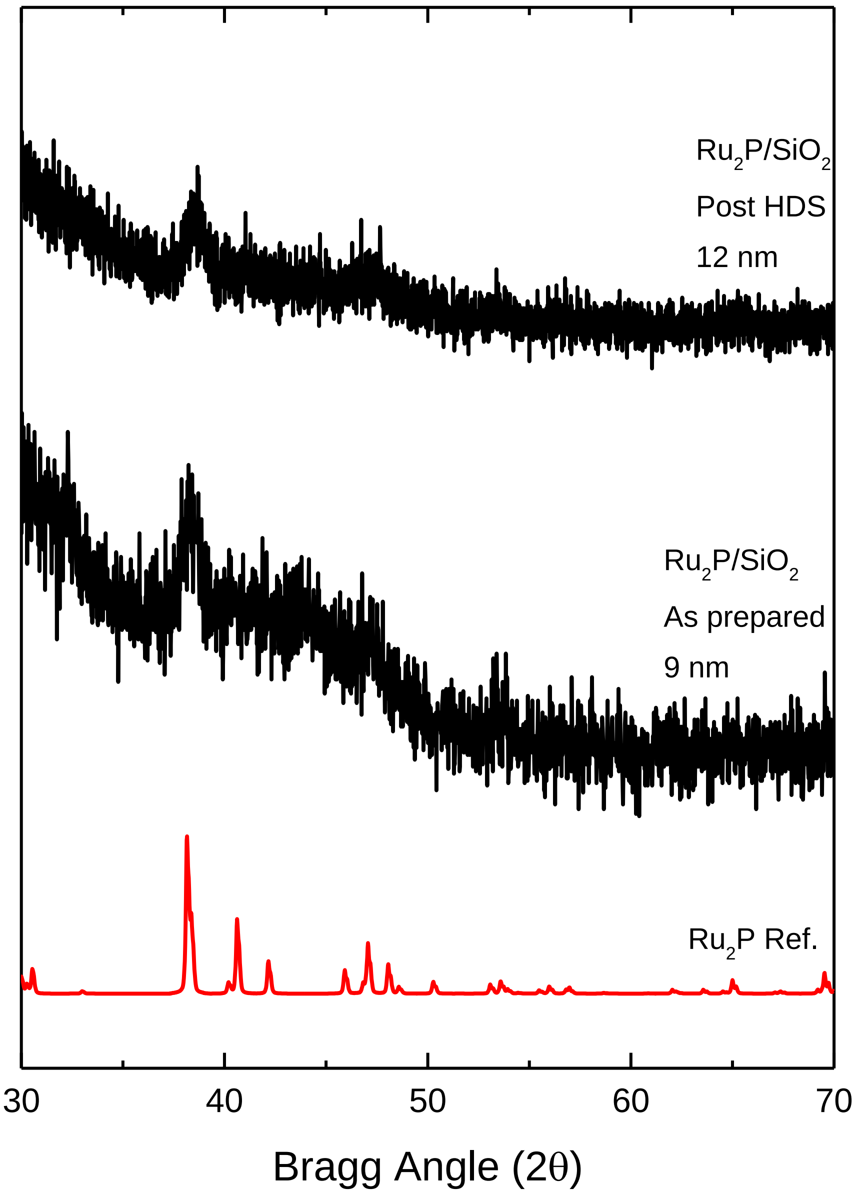

Figure 3.3: XRD patterns of as as-prepared and HDS-tested 15 wt% Ru_2P/SiO_2 catalysts (P/M = 1.00).

Rh_2P/SiO_2 Catalyst

Figure 3.4 shows the X-ray diffraction pattern for an as-prepared 15 wt% Rh_2P/SiO_2 catalyst (P/Rh = 0.72). The XRD pattern matches well with a Rh_2P reference pattern (card no. 96-101-1345) from the JCPDS database, which indicates phase pure Rh_2P was synthesized. A previous study by the Bussell group reported a 5 wt% Rh_2P/SiO_2 catalyst with a X-ray diffraction pattern that was consistent with this work.[27] The average Rh_2P crystallite size (9 nm) of the 15 wt% Rh_2P/SiO_2 catalyst was calculated using the Scherrer equation and the peak at 32.7° corresponding to the {002} reflection in Figure 3.4. An XRD pattern of the Rh_2P/SiO_2 catalyst was acquired after HDS testing. Based on the average Rh_2P crystallite size, no sintering occurred during HDS testing.

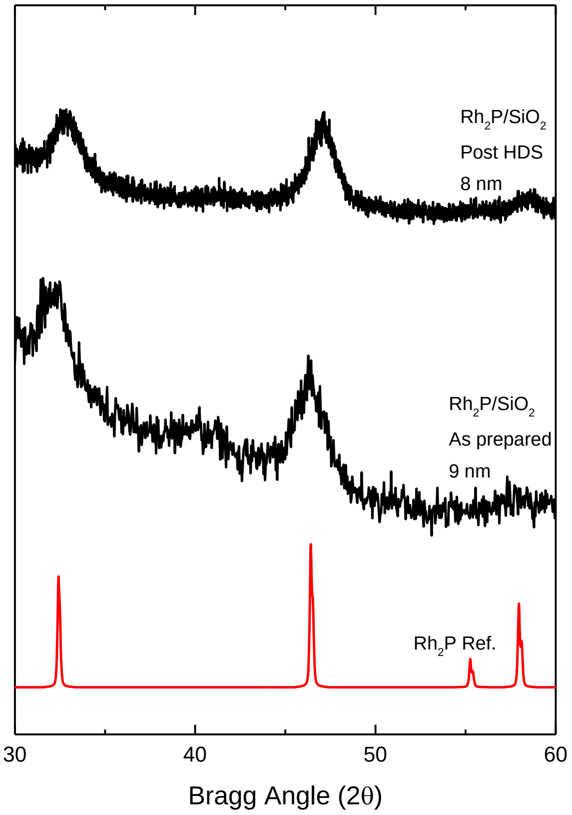

Figure 3.4: XRD patterns of as-prepared 15 wt% Rh_2P/SiO_2 catalyst and HDS tested 15 wt% Rh_2P/SiO_2 catalysts (P/Rh_2P = 0.72).

$Ni_xRu_{2-x}P/SiO_2$ Catalysts

Figure 3.5 shows x-ray diffraction patterns for a series of 15 wt% $Ni_xRu_{2-x}P/SiO_2$ catalysts. Starting from phase pure Ni_2P/SiO_2, the peak resulting from the {111} reflection at 40.7° shifted to a lower Bragg Angle as Ru was incorporated into the Ni_2P phase ($x \leq 1.75$). This was most apparent in the $Ni_{1.0}Ru_{1.0}P/SiO_2$ catalyst for which the {111} peak shifted to 39.6° which is between the reference patterns for Ni_2P and Ru_2P. This suggested that Ru was incorporated into the Ni_2P phase and that a single phase was maintained for $x \geq 1.50$. As the catalysts became more Ru-rich ($0.75 \leq x \leq 1.25$), the major reflection shifted from 39.6 ° to 39.1° and the phase purity became difficult to determine. This suggests the possibility that both Ni_2P and Ru_2P were present for these compositions. At Ru-rich compositions ($x \leq 0.50$) the major reflection appeared to be {112} at 38.6° suggesting that a phase change had occurred and that Ni atoms were being incorporated into the Ru_2P phase. As compositions increased in Ru-content ($x \leq 0.25$), the {112} reflection shifted to 38.2° corresponding to phase pure Ru_2P. This peak shift suggests the presence of a single bimetallic phosphide phase at compositions where $x \geq 1.50$ and $x \leq 0.50$. For compositions $0.75 \leq x \leq 1.25$, the phase purity was difficult to determine and the possibility of both Ni_2P and Ru_2P phases existing together was likely.

As described later, the most active catalyst from the $Ni_xRu_{2-x}P/SiO_2$ series was $Ni_{1.85}Ru_{0.15}P/SiO_2$. Additional, high Ni-content catalysts were synthesized with compositions on either side of this maximum in HDS conversion and the diffraction patterns for these catalysts are shown in Figure 3.6.

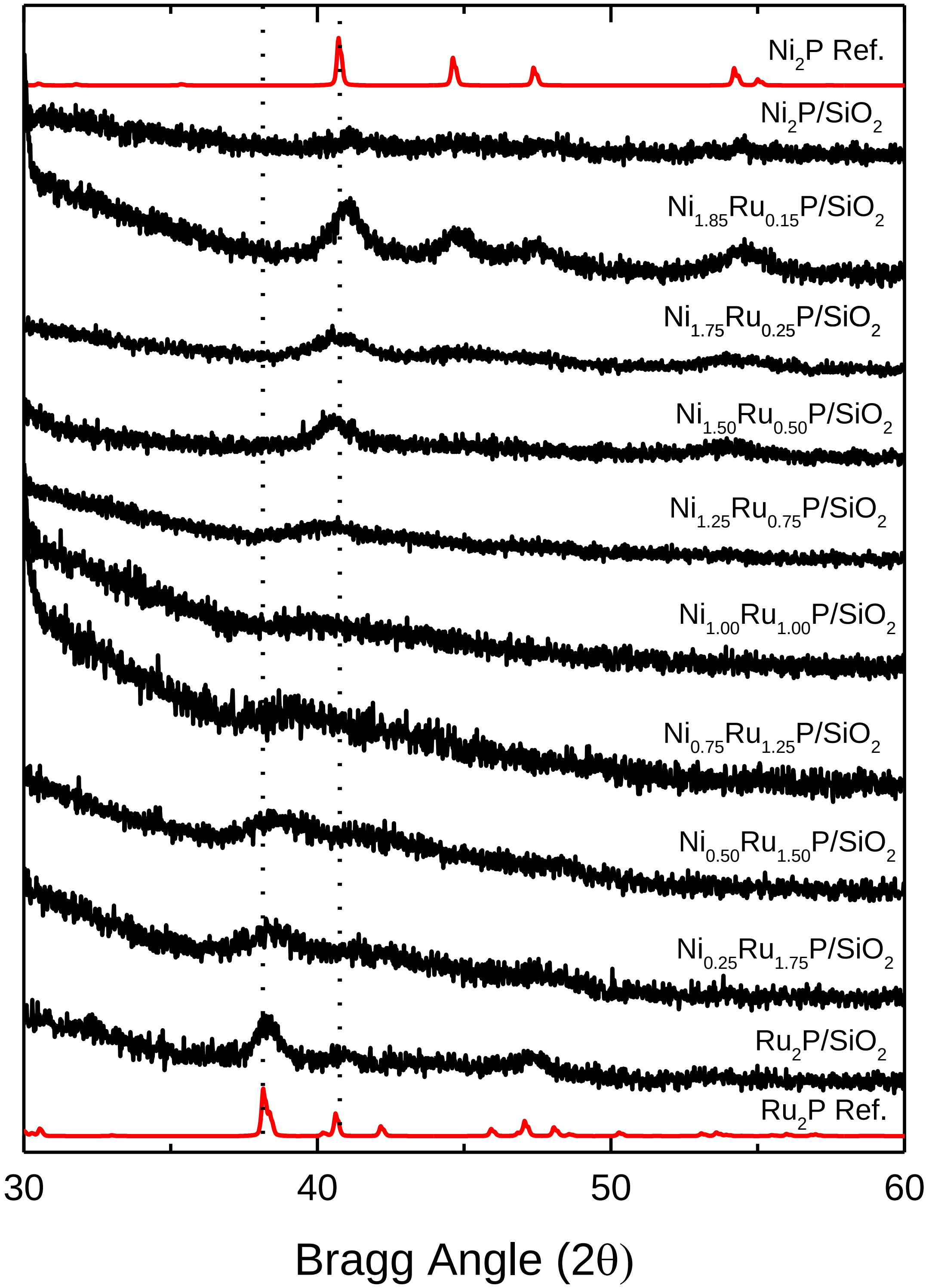

Figure 3.5: X-ray diffraction patterns of as-prepared 15 wt% $Ni_xRu_{2-x}P/SiO_2$ catalysts.

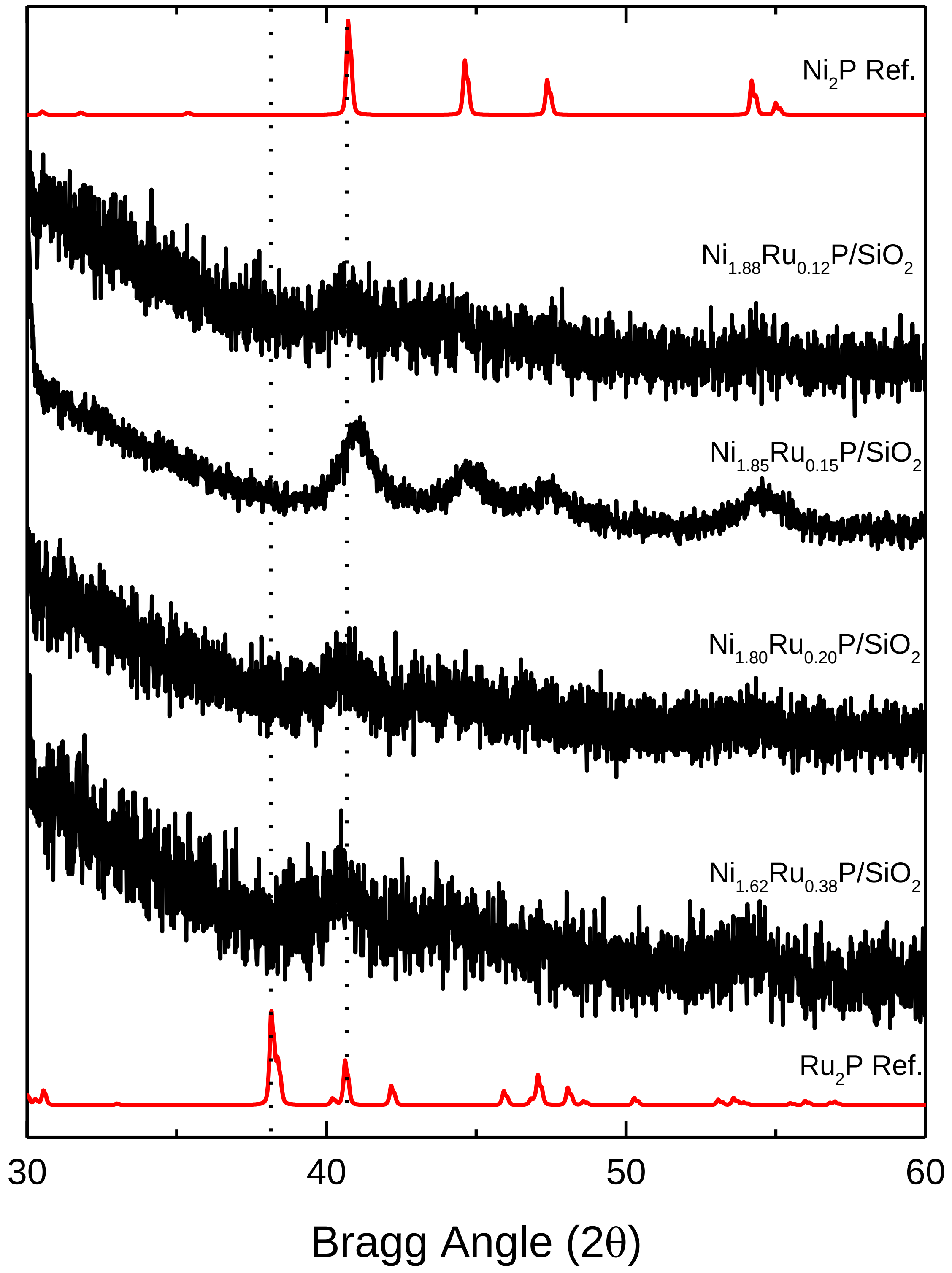

Figure 3.6: X-ray diffraction patterns of as-prepared 15 wt% $Ni_xRu_{2-x}P/SiO_2$ catalysts with compositions $1.62 \leq x \leq 1.88$.

$Ni_xRh_{2-x}P/SiO_2$ Catalysts

Figure 3.7 shows XRD patterns of the $Ni_xRh_{2-x}P/SiO_2$ catalysts over the full range of compositions investigated.

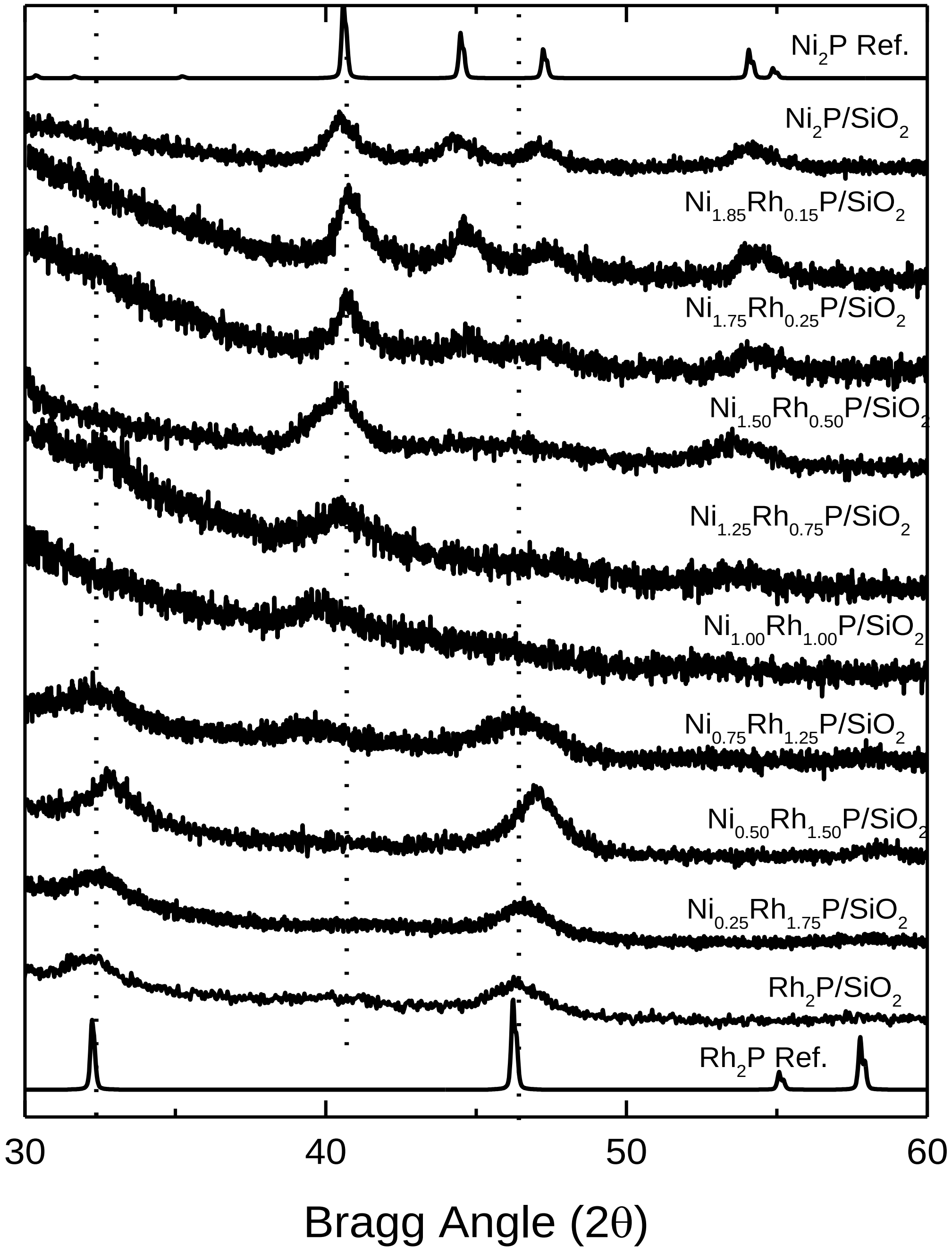

Figure 3.7: X-ray diffraction patterns of the as-prepared 15 wt% $Ni_xRh_{2-x}P/SiO_2$ catalysts.

For the Ni-rich catalysts, the peak at 40.7° is assigned to the {111} reflection of the Ni_2P phase. This peak shifted to lower Bragg angle due to the increased incorporation of Rh into the Ni_2P phase. Similar to the $Ni_xRu_{2-x}P/SiO_2$ series, two phases (Rh_2P and Ni_2P) were observed for the compositions having $0.63 \le x \le 0.75$. The most prominent peaks for the two phases appeared at composition $Ni_{0.75}Rh_{1.25}P/SiO_2$, for which the Rh_2P and Ni_2P phases composed 78% and 22% of the catalyst, respectively, as determined from Rietveld refinement (Figure 3.9). Two additional

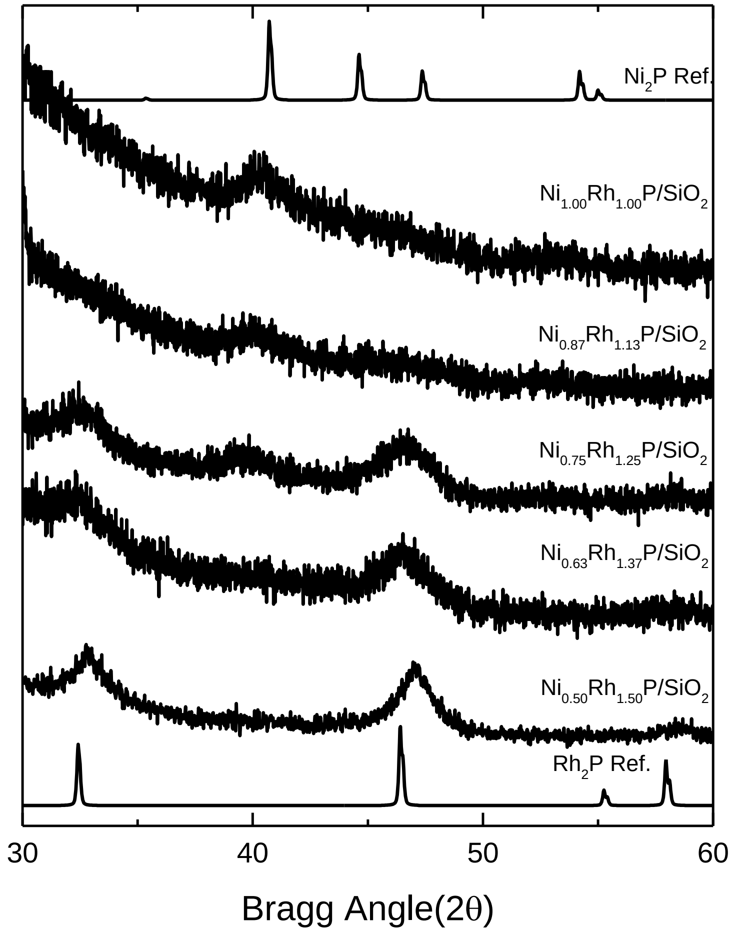

Figure 3.8: X-ray diffraction patterns of as-prepared 15 wt% $Ni_xRh_{2-x}P/SiO_2$ catalysts with compositions $0.50 \le x$ 1.00.

catalysts were synthesized in this compositional space for which two phases were identified as being present (Figure 3.8).

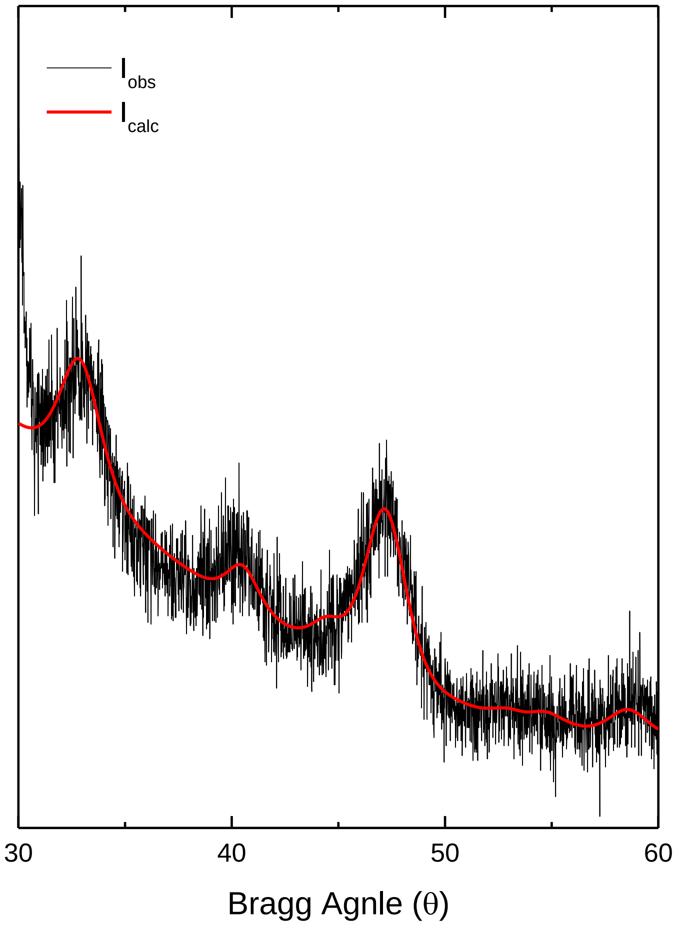

Figure 3.9: Rietveld fit (red line) for the XRD pattern (black line) of $Ni_{0.75}Rh_{1.25}P/SiO_2$ catalyst.

While a composition of $Ni_{0.87}Rh_{1.13}P/SiO_2$ displayed only one peak resulting from the {111} reflection of the Ni_2P phase, $Ni_{0.63}Rh_{1.37}P/SiO_2$ showed a strong peak resulting from the {002} reflection of the Rh_2P phase, but also a weak peak resulting from the {111} reflection of the Ni_2P phase. For the Rh rich catalysts, the primary peak at 32.5° resulted from the {002} reflection. The subsequent Rh rich catalysts (x = 0.50) shows peaks at 32.5° and 46.6° corresponding to Rh_2P crystalline phase. Outside of the composition space of $0.63 \leq x \leq 0.75$, the $Ni_xRh_{2-x}P/SiO_2$ catalyst series consisted of a single phase. Prior to the phase change from

Ni_2P to Rh_2P, $x \geq 0.87$, the Rh atoms were incorporated into the hexagonal structure (C22-type) of the Ni_2P phase as evidenced by the {111} reflection shifting to a lower Bragg angle as a result of the expansion of the unit cell due to the incorporation of the larger Rh atoms.[28] At higher Rh-content compositions, $x \leq 0.50$, the Ni atoms were incorporated into the cubic structure (C1-type) of the Rh_2P phase as evidenced by the {112} reflection shifting to higher Bragg angles due to the contraction of the unit cell by the incorporation of the smaller Ni atoms.[29]

3.1.2 Energy Dispersive X-ray Analysis

SEM-EDX was used to determine the elemental composition in the near surface region of the 15 wt% $Ni_xRu_{2-x}P/SiO_2$ catalysts (Figure 3.10) and 15 wt% $Ni_xRh_{2-x}P/SiO_2$ catalysts (Figure 3.13).

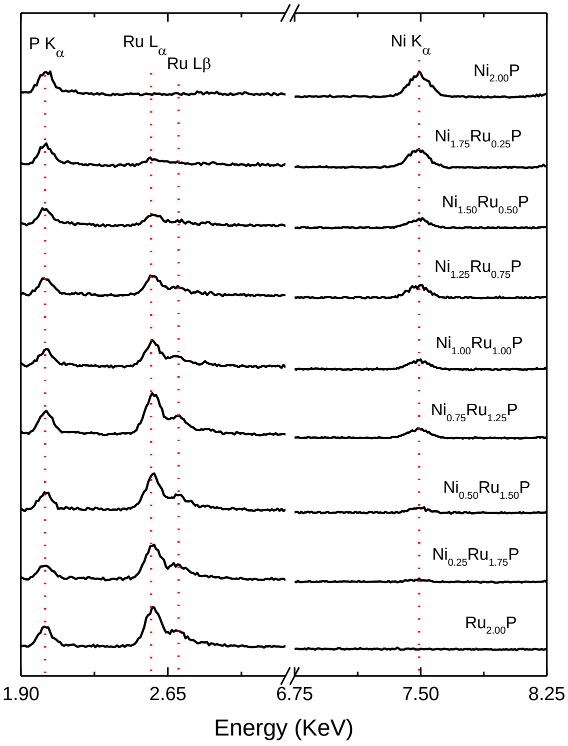

Figure 3.10: EDX spectra of as-prepared 15 wt% $Ni_xRu_{2-x}P/SiO_2$ catalysts.

Table 3.1: Bulk compositions of 15 wt% $Ni_xRu_{2-x}P/SiO_2$ series as determined by SEM-EDX.

Target Composition	Measured Composition	P/M
$Ni_{2.00}P_{1.00}$	$Ni_{2.42}P_{1.00}$	0.41
$Ni_{1.75}Ru_{0.25}P_{1.00}$	$Ni_{1.53}Ru_{0.24}P_{1.00}$	0.56
$Ni_{1.50}Ru_{0.50}P_{1.00}$	$Ni_{1.41}Ru_{0.49}P_{1.00}$	0.53
$Ni_{1.25}Ru_{0.75}P_{1.00}$	$Ni_{1.84}Ru_{0.82}P_{1.00}$	0.38
$Ni_{1.00}Ru_{1.00}P_{1.00}$	$Ni_{1.50}Ru_{1.16}P_{1.00}$	0.38
$Ni_{0.75}Ru_{1.25}P_{1.00}$	$Ni_{1.00}Ru_{1.26}P_{1.00}$	0.44
$Ni_{0.50}Ru_{1.50}P_{1.00}$	$Ni_{0.82}Ru_{1.52}P_{1.00}$	0.43
$Ni_{0.25}Ru_{1.25}P_{1.00}$	$Ni_{0.45}Ru_{1.69}P_{1.00}$	0.47
$Ru_{2.00}P_{1.00}$	$Ru_{1.43}P_{1.00}$	0.70

Elemental compositions were quantified by measuring the peak areas associated with the K_α transitions of Ni (7.5 eV), Ru (2.6 eV), Rh (2.7 eV), and P (2.0 eV). EDX spectra in Figure 3.9 show that as the Ru content of a catalyst increases, the peak area corresponding to the K_α transition of Ni decreases while the peak area of the L_α transition of Ru area increases. Figures 3.10-3.11 compare the measured Ni/(Ni + Ru) ratios and measured P/M ratios to the expected ratios.

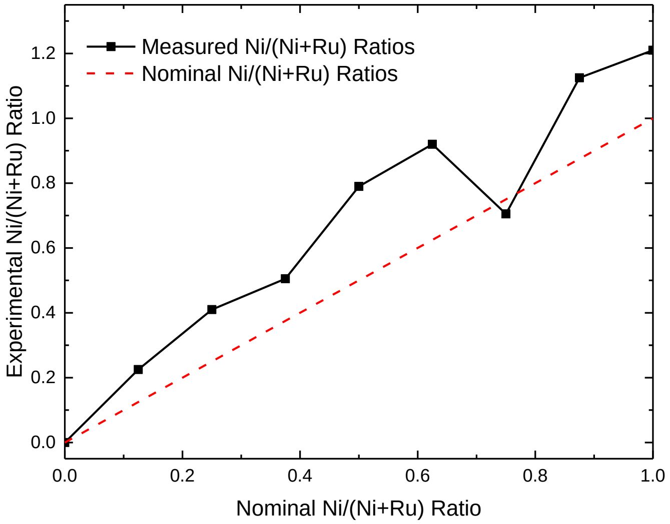

Figure 3.11: Experimentally determined Ni/(Ni+Ru) molar ratios from EDX compositions for the 15 wt% $Ni_xRu_{2-x}P/SiO_2$ catalysts.

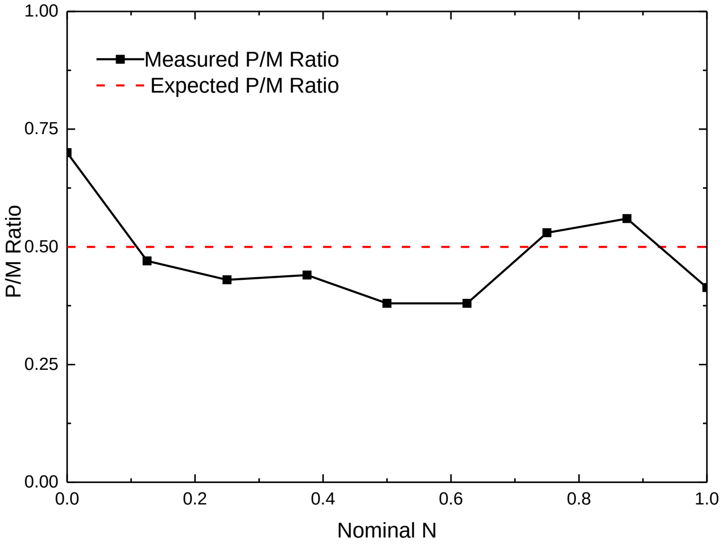

Figure 3.12: Experimentally determined P/(Ni+Ru) molar ratios from EDX compositions of the 15 wt% $Ni_xRu_{2-x}P/SiO_2$ catalysts.

The metal compositions in Table 3.1 determined by EDX were metal-rich with the exception of $Ni_{1.50}Ru_{0.50}P/SiO_2$. The average P/M ratio (P/M = 0.48) for the catalysts determined using EDX were significantly lower than the nominal P/M ratio used in the catalyst precursors (P/M = 0.72), but differed only slightly compared to the stoichiometric value (P/M = 0.50). This indicates that excess phosphorus was lost, likely as PH_3, during TPR synthesis.

The EDX spectra for the $Ni_xRh_{2-x}P/SiO_2$ series and the compositional data for the series are shown in Figures 3.12-3.14.

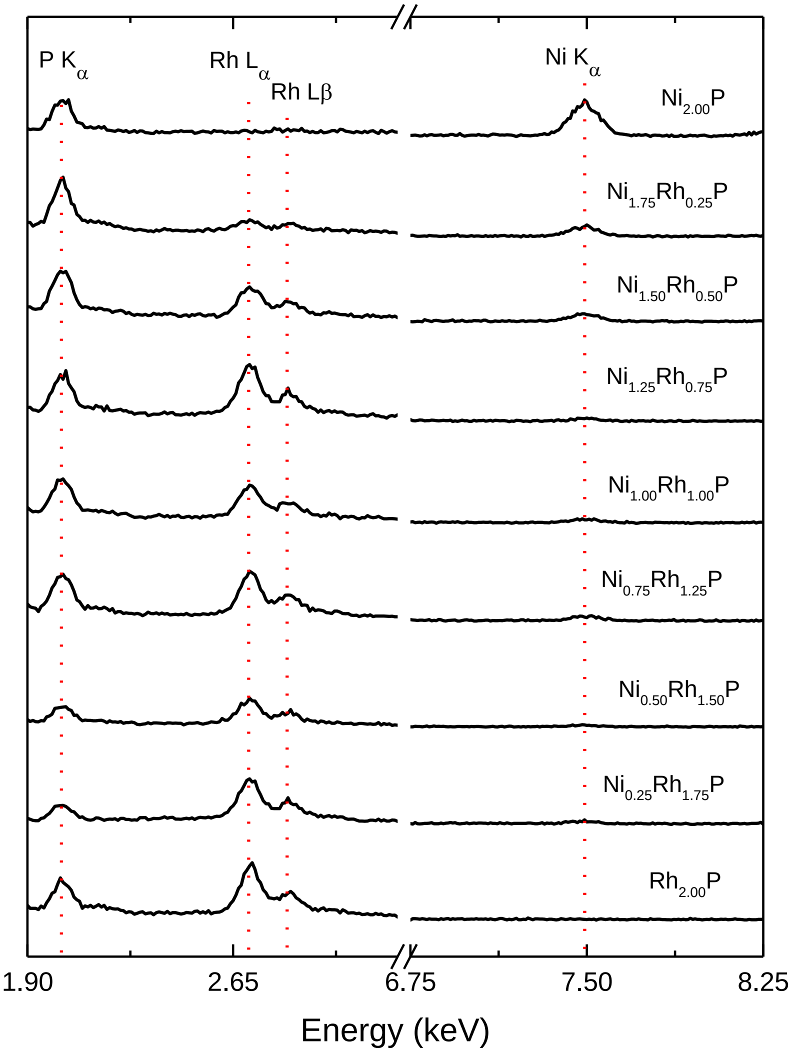

Figure 3.13: EDX spectra of as-prepared 15 wt% $Ni_xRh_{2-x}P/SiO_2$ catalysts.

Table 3.2: Bulk compositions of 15 wt% $Ni_xRh_{2-x}P/SiO_2$ catalysts as determined by SEM-EDX.

Target Composition	Measured Composition	P/M
$Ni_2P_{1.00}$	$Ni_{2.42}P_{1.00}$	0.41
$Ni_{1.75}Rh_{0.25}P_{1.00}$	$Ni_{1.17}Rh_{0.19}P_{1.00}$	0.74
$Ni_{1.50}Rh_{0.50}P_{1.00}$	$Ni_{1.00}Rh_{0.28}P_{1.00}$	0.78
$Ni_{1.25}Rh_{0.75}P_{1.00}$	$Ni_{0.97}Rh_{0.45}P_{1.00}$	0.70
$Ni_{1.00}Rh_{1.00}P_{1.00}$	$Ni_{0.57}Rh_{0.69}P_{1.00}$	0.79
$Ni_{0.75}Rh_{1.25}P_{1.00}$	$Ni_{0.71}Rh_{0.98}P_{1.00}$	0.59
$Ni_{0.50}Rh_{1.50}P_{1.00}$	$Ni_{0.66}Rh_{1.27}P_{1.00}$	0.52
$Ni_{0.25}Rh_{1.25}P_{1.00}$	$Ni_{0.47}Rh_{1.36}P_{1.00}$	0.55
$Rh_2P_{1.00}$	$Rh_{1.45}P_{1.00}$	0.69

As observed in the data in Figure 3.12 and Table 3.2, the peak corresponding to the K_α transition of Ni began to diminish as the second metal content, in this case Rh, increased and the subsequent L_α transition for Rh was observed. Figures 3.13-3.14 compare the measured Ni/(Ni + Rh) ratios and measured P/M ratios to expected ratios.

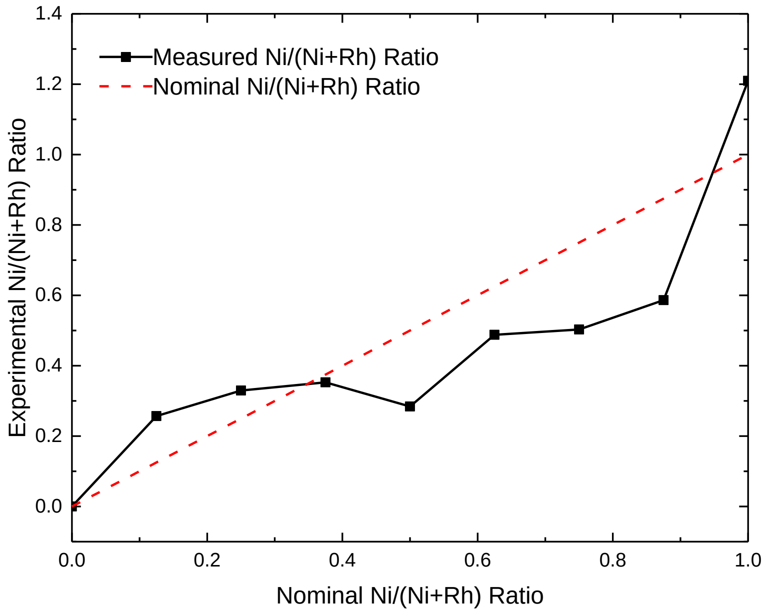

Figure 3.14: Experimentally determined Ni/(Ni+Rh) molar ratios of the 15 wt% $Ni_xRh_{2-x}P/SiO_2$ catalysts.

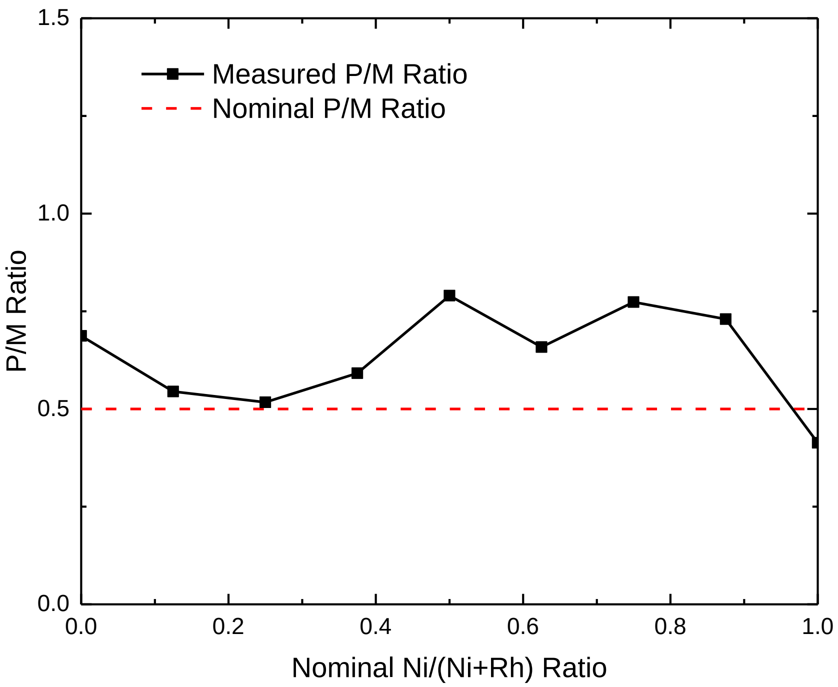

Figure 3.15: Experimental P/(Ni+Rh) molar ratios of the 15 wt% $Ni_xRh_{2-x}P/SiO_2$ catalysts.

The measured Ni/(Ni+Rh) ratios varied slightly from those of the nominal compositions, but were not significantly different. The P/M ratio determined by EDX for compositions x = 0 and 0.25 ≤ x ≤ 0.75 were similar to the P/M stoichiometric ratio (P/M = 0.5) while compositions 1.75 ≤ x ≤ 1.00 were similar to the P/M ratio of the catalyst precursors (P/M = 0.72).

3.1.3 Surface Area Analysis and CO Chemisorption Analysis

The results from the BET surface area, BJH pore size distribution and CO chemisorption measurements for the $Ni_xRu_{2-x}P/SiO_2$ catalysts are shown below in Table 3.3 and Figures 3.15-3.16.

Table 3.3: Surface area and pore size distribution of 15 wt% $Ni_xRu_{2-x}P/SiO_2$ catalysts.

Catalyst	Surface Area (m^2/g)	Average Particle Size (nm)	Average Pore Size (nm)	CO Chemisorption (µmol/g)
$Ni_2P_{1.00}$	119	<5	8.3	143
$Ni_{1.85}Ru_{0.15}P_{1.00}$	160	7	14.3	155
$Ni_{1.80}Ru_{0.20}P_{1.00}$	163	8	14.5	167
$Ni_{1.75}Ru_{0.25}P_{1.00}$	158	6	13.0	147
$Ni_{1.63}Ru_{0.37}P_{1.00}$	166	6	16.1	160
$Ni_{1.50}Ru_{0.50}P_{1.00}$	193	6	15.7	158
$Ni_{1.25}Ru_{0.75}P_{1.00}$	156	<5	12.9	121
$Ni_{1.00}Ru_{1.00}P_{1.00}$	143	<5	14.7	140
$Ni_{0.75}Ru_{1.25}P_{1.00}$	143	5	15.6	128
$Ni_{0.50}Ru_{1.50}P_{1.00}$	121	6	15.6	134
$Ni_{0.25}Ru_{1.25}P_{1.00}$	151	8	14.6	115
$Ru_2P_{1.00}$	169	8	16.5	134

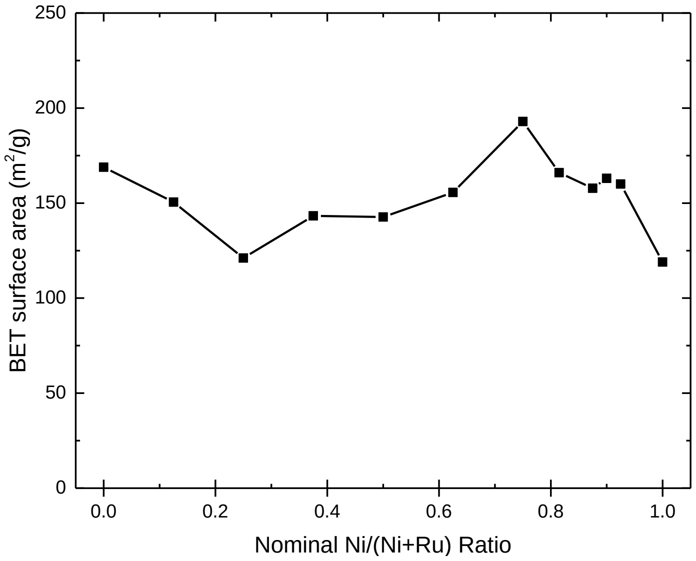

Figure 3.16: BET surface areas of the 15 wt% $Ni_xRu_{2-x}P/SiO_2$ catalysts.

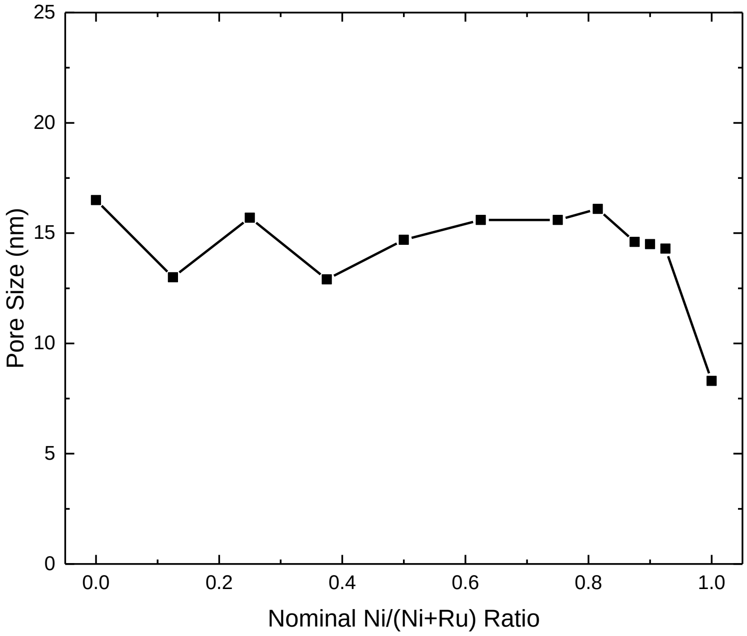

Figure 3.17: Average BJH pore sizes of the 15 wt% $Ni_xRu_{2-x}P/SiO_2$ catalysts.

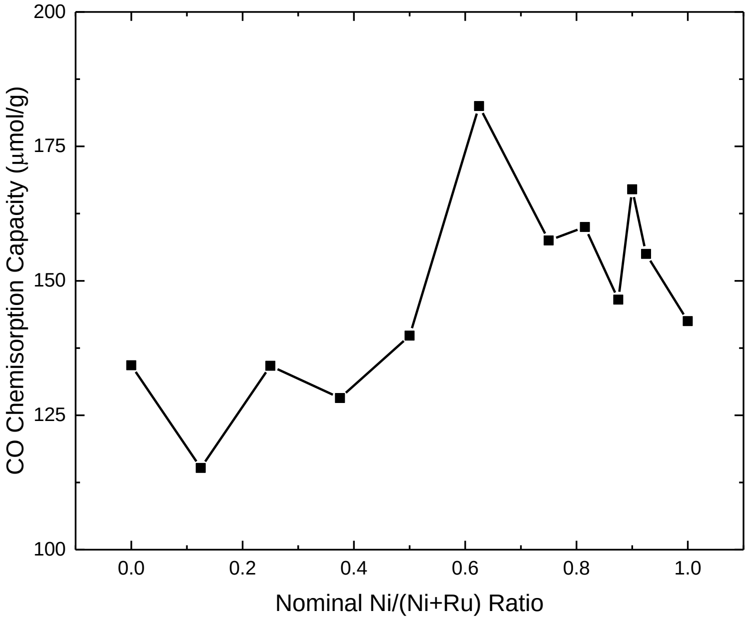

Figure 3.18: CO chemisorption capacities of the 15 wt%, $Ni_xRu_{2-x}P/SiO_2$ catalysts.

For the $Ni_xRu_{2-x}P/SiO_2$ catalysts, no significant trend in the surface area was observed throughout the composition range. The average pore sizes of the $Ni_xRu_{2-x}P/SiO_2$ catalysts show a slight downward trend ending with Ni_2P/SiO_2. The CO chemisorption capacities of the $Ni_xRu_{2-x}P/SiO_2$ catalysts were observed to increase as Ni-content increased.

The BET surface areas, BJH pore sizes and CO chemisorption capacities for the $Ni_xRh_{2-x}P/SiO_2$ catalysts are listed below in Table 3.4 and plotted Figures 3.18-3.19.

Table 3.4: Surface area and pore size distribution of 15 wt% $Ni_xRh_{2-x}P/SiO_2$ catalysts.

Catalyst	Surface Area (m^2/g)	Average Particle size (nm)	AveragePore size (nm)	CO Chemisorption (μmol/g)
$Ni_2P_{1.00}$	119	<5	8.3	143
$Ni_{1.85}Rh_{0.15}P_{1.00}$	185	7	12.5	180
$Ni_{1.75}Rh_{0.25}P_{1.00}$	180	9	16.2	188
$Ni_{1.50}Rh_{0.50}P_{1.00}$	184	7	14.3	166
$Ni_{1.25}Rh_{0.75}P_{1.00}$	168	5	15.5	144
$Ni_{1.00}Rh_{1.00}P_{1.00}$	202	<5	14.7	160
$Ni_{0.87}Rh_{1.12}P_{1.00}$	180	5	16.8	177
$Ni_{0.75}Rh_{1.25}P_{1.00}$	190	5	13.4	169
$Ni_{0.63}Rh_{1.37}P_{1.00}$	205	6	17.0	183
$Ni_{0.50}Rh_{1.50}P_{1.00}$	197	9	14.9	157
$Ni_{0.25}Rh_{1.25}P_{1.00}$	190	7	13.2	193
$Rh_2P_{1.00}$	203	6	15.7	201

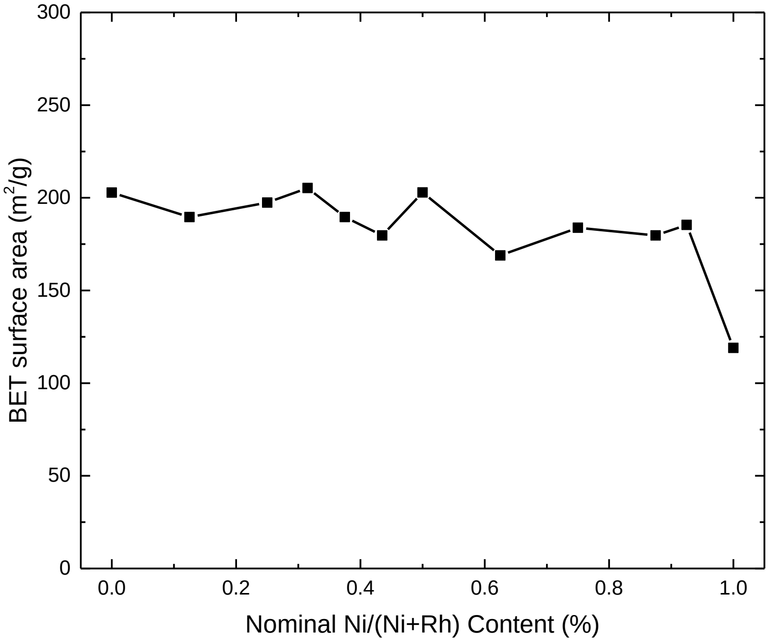

Figure 3.19: BET surface areas of the 15 wt% $Ni_xRh_{2-x}P/SiO_2$ catalysts.

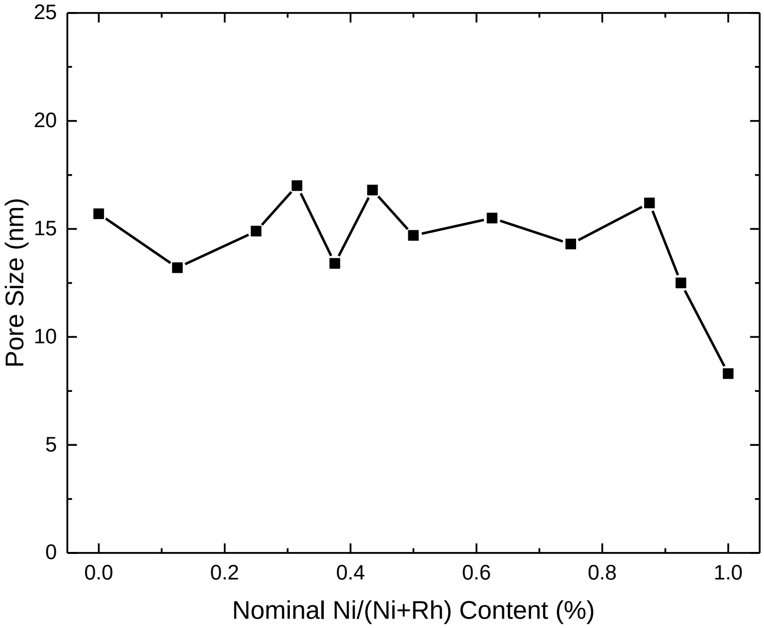

Figure 3.20: Average pore size of the 15 wt% $Ni_xRh_{2-x}P/SiO_2$ catalysts.

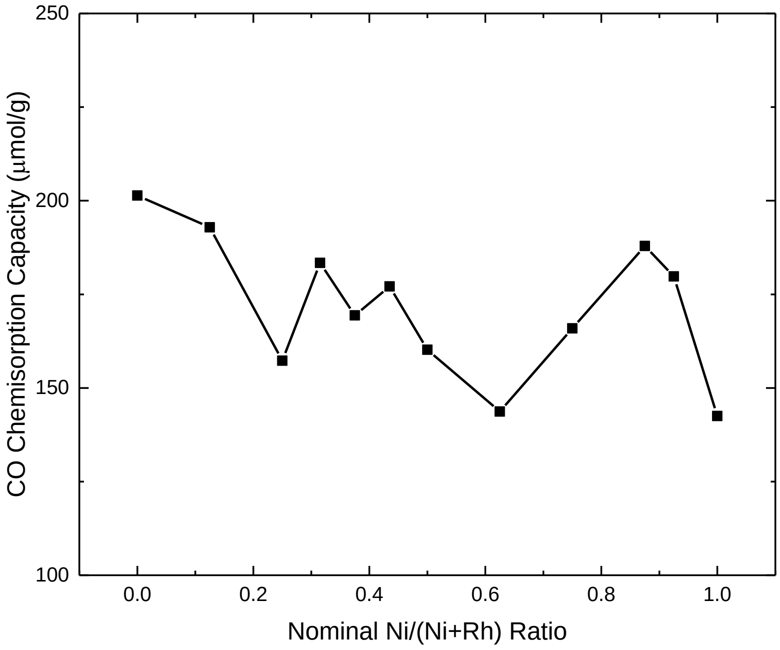

Figure 3.21: CO chemisorption capacities of the 15 wt% $Ni_xRh_{2-x}P/SiO_2$ catalysts.

The BET surface areas and average pore sizes of the $Ni_xRh_{2-x}P/SiO_2$ catalysts showed slightly downward trends as Ni content increased. The CO chemisorption capacities of the $Ni_xRh_{2-x}P/SiO_2$ series showed an overall downward trend as well, with the highest CO chemisorption capacity measured for the Rh_2P/SiO_2 catalyst.

3.1.4 X-ray Photoelectron Spectroscopy

XPS spectra were collected for selected catalysts in the $Ni_xRu_{2-x}P/SiO_2$ and $N_xRh_{2-x}P/SiO_2$ catalysts to probe the surface compositions and the electronic environments of the elements of interest (Figures 3.21-3.22). Note that the selected catalysts were not re-reduced prior to XPS analysis and as such underwent XPS analysis with the passivization layer intact. The peak in XPS spectra reveal information about the binding energies of core electrons in the elements present at the surface of the catalysts. The peaks were identified by comparing the observed binding energies with those from the National Institute of Standards and Technology (NIST) XPS database.[36] Shifts in observed binding energies from those of the NIST database are due to the different chemical environments of surface atoms in the catalysts. The presence of Ni^0, Ru^0, Rh^0, and P was confirmed by using the reference binding energies listed in Table 3.5. The presence of P was confirmed by observing a peak at 133.3 eV which corresponds to the binding energy of a $2p_{3/2}$ electron, but one that originated from a highly oxidized P species (PO_4^{3-}).[100] The XPS spectra of select $Ni_xRu_{2-x}P/SiO_2$ and $Ni_xRh_{2-x}P/SiO_2$ catalysts are displayed in Figure 3.2 and Figure 3.23 respectively.

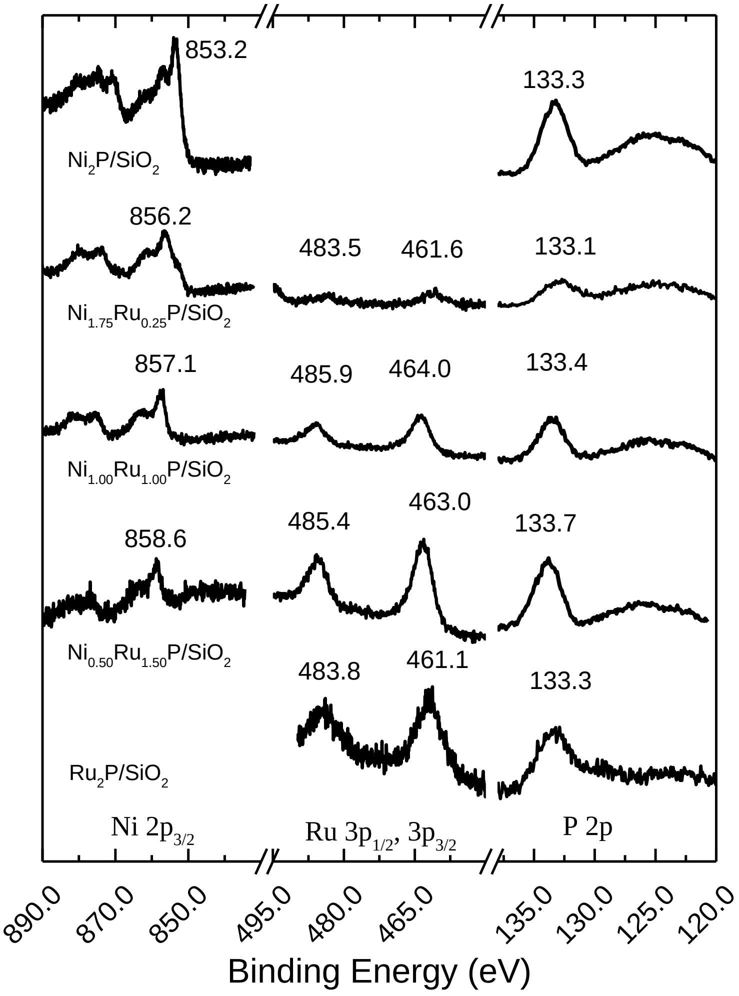

Figure 3.22: XPS spectra of select $Ni_xRu_{2-x}P/SiO_2$ catalysts.

The XPS spectra of Ni_2P/SiO_2 showed a strong Ni $2p_{3/2}$ peak at 853.2 eV suggesting that the majority of the Ni present was in the Ni^0 state. The XPS spectra for the $Ni_{1.75}Ru_{0.25}P/SiO_2$ catalysts displayed shoulder peaks for the presence of Ni^0 at high Ni-content compositions, but as the Ru content increased, the peaks corresponding to Ni $2p_{3/2}$ increased in binding energy suggesting an oxidized state such as Ni^{2+} at 856.2-858.6 eV. The XPS spectra of Ru_2P/SiO_2 showed a strong peak at 461.1 eV suggesting that the majority of the Ru present was in the Ru^0 state; however, for the bimetallic compositions, the $3p_{3/2}$ peak was shifted (from 461.1 to 463.0 eV) suggesting an oxidized form of Ru such as Ru^{4+}.

Table 3.5: Reference binding energies used to identify elements of interest in $Ni_xRu_{2-x}P/SiO_2$ catalysts.[36]

Reference Compound	Orbital	Binding Energy (eV)
Ni^0	$2p_{1/2}$, $2p_{3/2}$	853.2, 870.0
Ru^0	$3p_{1/2}$, $3p_{3/2}$	484.0, 461.6
Ru^{4+}	$3p_{3/2}$	463.2
Rh^0	$3d_{3/2}$, $3d_{5/2}$	312.2, 307.5
P^0	2p	129.7
PO_4^{3-}	2p	133.3

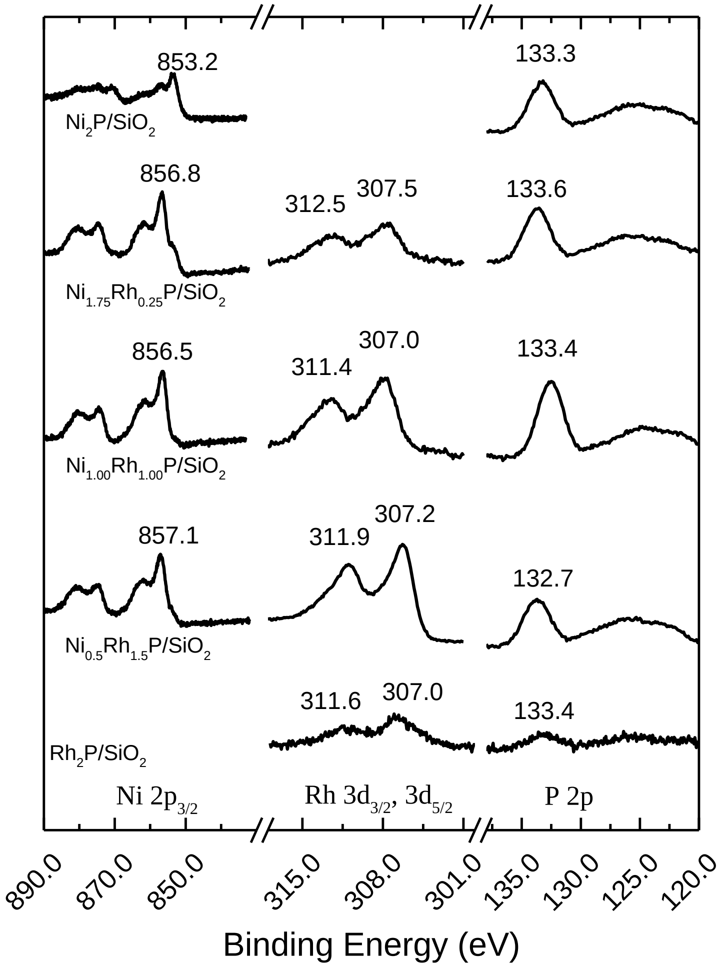

Figure 3.23: XPS spectra of select $Ni_xRh_{2-x}P/SiO_2$ catalysts.

The XPS spectra of the $Ni_{1.75}Rh_{0.25}P/SiO_2$ catalysts showed a Ni $2p_{3/2}$ shoulder at 853.8 eV suggesting the presence of Ni^0 in addition to oxidized Ni^{2+} observed at 856.8 eV. For compositions $Ni_{1.00}Ru_{1.00}P/SiO_2$ and $Ni_{0.50}Ru_{1.50}P/SiO_2$, only the presence of Ni^{2+} was determined.The XPS spectra of Rh_2P/SiO_2 and the bimetallic compositions showed a peak at 307.0-307.5 eV suggesting the presence of Rh^0 and no evidence of an oxidized form.

Table 3.4: Binding energies and surface compositions of select 15 wt% $Ni_xRu_{2-x}P/SiO_2$ catalysts.

Nominal Composition	Surface Composition	Surface P/M ratio	Ni $2p_{3/2}$ BE (eV)	Ru $3p_{3/2}$ BE (eV)	P 2p BE (eV)
$Ni_2P_{1.00}$	$Ni_{2.55}P_{1.00}$	0.39	853.2	N/A	133.3
$Ni_{1.75}Ru_{0.25}P_{1.00}$	$Ni_{1.04}Ru_{0.32}P_{1.00}$	0.71	856.2	461.6	133.1
$Ni_{1.00}Ru_{1.00}P_{1.00}$	$Ni_{0.73}Ru_{0.61}P_{1.00}$	0.74	857.1	464.0	133.4
$Ni_{0.50}Ru_{1.50}P_{1.00}$	$Ni_{0.22}Ru_{087}P_{1.00}$	0.91	858.6	463.0	133.7
$Ru_2P_{1.00}$	$Ru_{0.62}P_{1.00}$	1.59	N/A	461.1	133.3

Table 3.5: Binding energies and surface compositions of select 15 wt% $Ni_xRh_{2-x}P/SiO_2$ catalysts.

Nominal Composition	Surface Composition	Surface P/M ratio	Ni $2p_{3/2}$ BE (eV)	Rh $3p_{3/2}$ BE (eV)	P 2p BE (eV)
$Ni_2P_{1.00}$	$Ni_{2.55}P_{1.00}$	0.39	853.2	N/A	133.3
$Ni_{1.75}Rh_{0.25}P_{1.00}$	$Ni_{1.02}Rh_{0.21}P_{1.00}$	0.81	856.8	307.5	133.6
$Ni_{1.00}Rh_{1.00}P_{1.00}$	$Ni_{0.69}Rh_{0.77}P_{1.00}$	0.68	856.5	307.0	133.4
$Ni_{0.50}Rh_{1.50}P_{1.00}$	$Ni_{0.38}Rh_{0.93}P_{1.00}$	0.75	856.5	307.2	132.7
$Rh_2P_{1.00}$	$Rh_{0.77}P_{1.00}$	1.29	N/A	307.0	133.4

3.2 HDS Activities and Product Selectivities of $Ni_xRu_{2-x}P/SiO_2$ Catalysts

The HDS measurements for the $Ni_xRu_{2-x}P/SiO_2$ catalysts were carried out over a temperature range of 533-653 K with the reactor at a total pressure of 3 MPa. A model feed comprised of 1000 ppm 4,6-DMDBT in decalin was allowed to flow through the reactor. Once the reactor had stabilized for 24 h, the first measurement was taken at the starting temperature of 533 K, after which the temperature was increased by 20 K. The reactor was allowed to stabilize for at least 4 h after each temperature ramp prior to taking a measurement. Two sets of measurements were taken during a 24 h period for a total of 96 h for the full range of temperatures. At each temperature, four effluent samples were collected and analyzed via GC to determine what percentage of 4,6-DMDBT was converted by the catalyst. The relative amounts of four normalized products (3,3'-DMBP, 3,3'-DMCHB, 3,3'-DMBCH, and TH-4,6-DMDBT) were observed at each temperature to determine the product selectivity of the catalyst. The reaction network for the HDS of 4,6-DMDBT is shown in Figure 3.24.

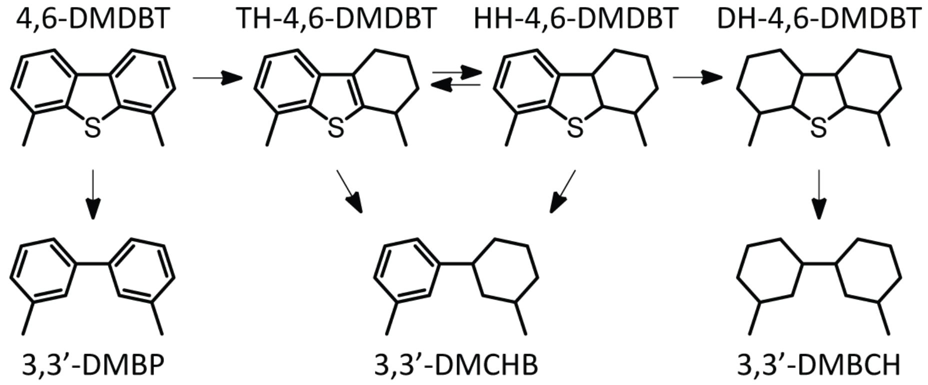

Figure 3.24 Reaction network for the HDS of 4,6-DMDBT.

The product selectivity and HDS conversions of 4,6-DMDBT as a function of time by a $Ni_{1.75}Ru_{0.25}P/SiO_2$ catalyst are shown in Figures 3.25.

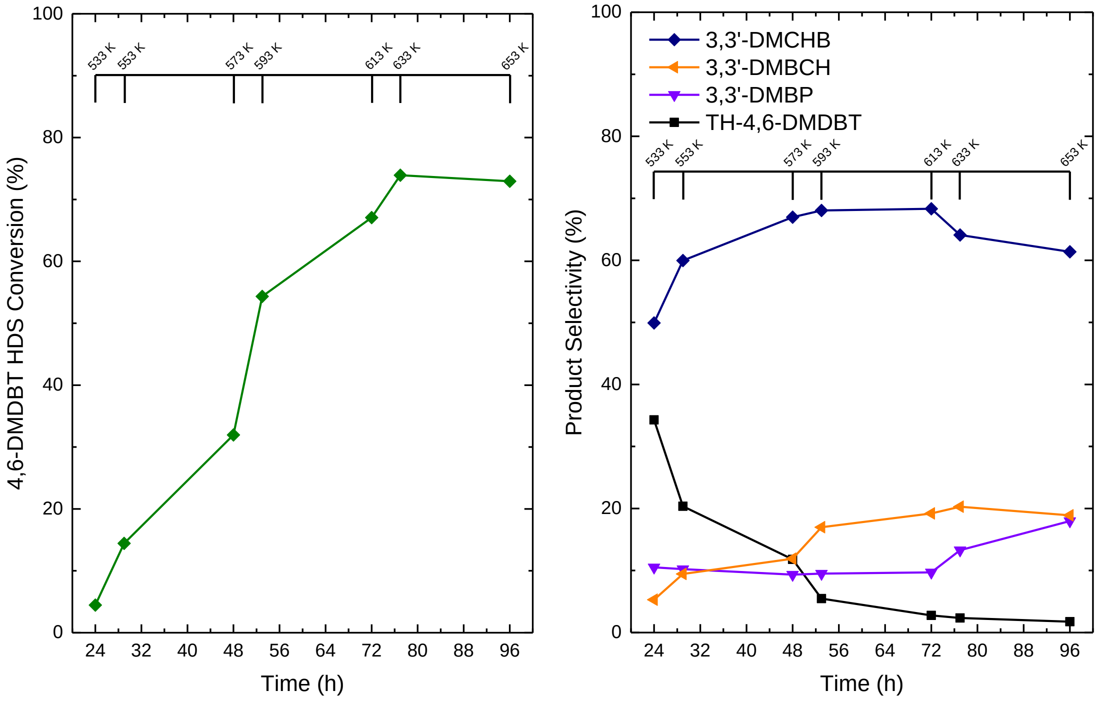

Figure 3.25 4,6-DMDBT HDS conversion (left) and the product selectivity (right) as a function of time for a 15 wt% $Ni_{1.75}Ru_{0.25}P/SiO_2$ catalyst over the temperature range 533-653K.

The $Ni_{1.75}Ru_{0.25}P/SiO_2$ catalyst was observed to increase its HDS conversion, over time and as temperature increased, with a maximum 4,6-DMDBT HDS conversion of 74% at hour 77 (T = 633 K). The most significant increases in HDS conversion were observed at hours 29-53. The product formation of TH-4,6-DMDBT was observed to decrease over time while the production of the major product, 3,3’-DMCHB was observed to initially increase, but remained fairly consistent after hour 29. The minor products (3,3’-DMBP and 3,3’-DMBCH) were not observed to significantly increase with time.

The 4,6-DMDBT HDS conversions as a function of temperature for selected 15 wt% $Ni_xRu_{2-x}P/SiO_2$ catalysts are displayed in Figure 3.26.

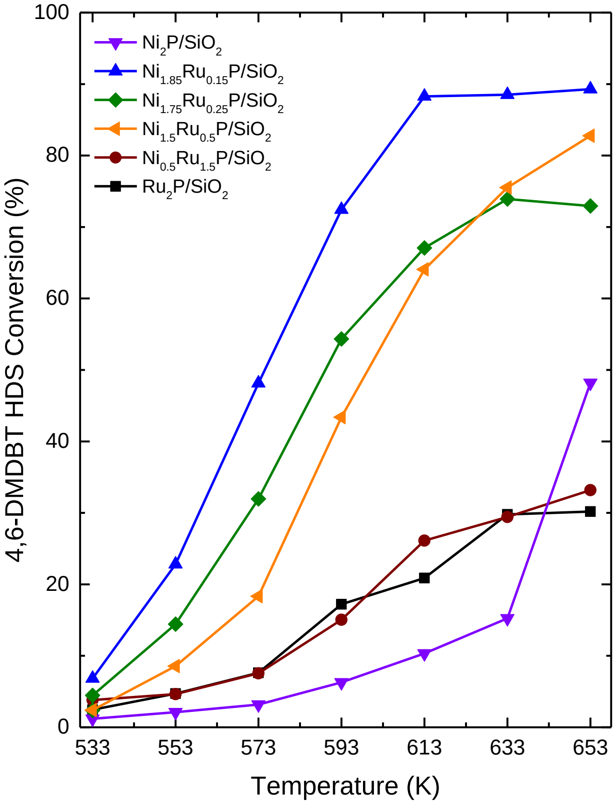

Figure 3.26: The 4,6-DMDBT HDS conversion for selected 15 wt% $Ni_xRu_{2-x}P/SiO_2$ catalysts.

The 4,6-DMDBT HDS conversion increased as the reactor temperature was increased for all $Ni_xRu_{2-x}P/SiO_2$ catalysts. The highest conversion was observed for the $Ni_{1.85}Ru_{0.15}P/SiO_2$ catalyst which reached a maximum HDS conversion of 89% at 653 K and exhibited the highest conversion throughout the temperature range. At lower temperatures ($T < 633$ K) the lowest HDS conversion was observed for Ni_2P/SiO_2; however, at 653 K the HDS conversion of Ni_2P/SiO_2 surpassed both Ru_2P/SiO_2 and $Ni_{0.5}Ru_{1.5}P/SiO_2$ catalysts. At 533 K, all of the catalysts had HDS conversions below 10%, but significant differences in HDS conversion were observed at higher temperatures.

To further investigate the $Ni_xRu_{2-x}P/SiO_2$ catalysts and the effect of composition on the HDS of 4,6-DMDBT, additional catalysts were tested and the HDS conversion at 573 K is plotted as a function of Ru-content in Figure 3.24.

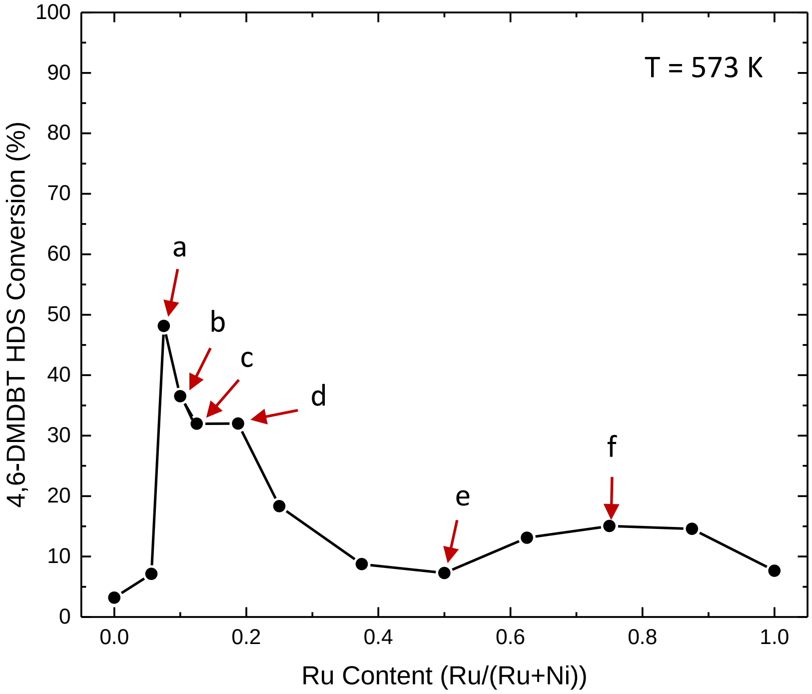

Figure 3.27: 4,6-DMDBT conversion as a function of Ru-content at 573 K for 15 wt% $Ni_xRu_{2-x}P/SiO_2$ catalysts. The following catalysts are labeled above: (a) $Ni_{1.85}Ru_{0.15}P/SiO_2$ (b) $Ni_{1.80}Ru_{0.20}P/SiO_2$ (c) $Ni_{1.75}Ru_{0.25}P/SiO_2$ (d) $Ni_{1.62}Ru_{0.38}P/SiO_2$ (e) $Ni_{1.0}Ru_{1.0}P/SiO_2$ (f) $Ni_{0.5}Ru_{1.5}P/SiO_2$.

With the exception of the $Ni_{1.88}Ru_{0.12}P/SiO_2$ catalyst, the high Ni-content catalysts displayed the highest HDS conversion of 4,6-DMDBT. The $Ni_{1.85}Ru_{0.15}P/SiO_2$ catalyst was the most active, with the HDS conversion decreasing on either side of this composition. The HDS conversions of Ru-rich $Ni_xRu_{2-x}P/SiO_2$ catalysts were substantially lower than those of the Ni-rich catalysts. The most HDS active catalysts were found to be those with compositions in the range $1.62 \le x \le 1.85$.

CO chemisorption capacities, HDS activities and the turnover frequencies and for $Ni_xRu_{2-x}P/SiO_2$ catalysts are reported in Tables 3.5

Table 3.6: CO chemisorption capacities, HDS activity, and turnover frequencies of the 15 wt% $Ni_xRu_{2-x}P/SiO_2$ catalysts.

Catalyst	**CO Chemisorption Capacity (μmol/g)**	**Activity @ 573 K (nmol DMDBT/$g_{cat.}$*s)**	**Turnover Frequency (s^{-1})**
Ni_2P/ SiO_2	143	1.34	9.40E-06
$Ni_{1.85}Ru_{0.15}P/ SiO_2$	155	20.3	1.31E-04
$Ni_{1.80}Ru_{0.20}P/ SiO_2$	167	15.0	8.98E-05
$Ni_{1.75}Ru_{0.25}P/ SiO_2$	147	13.5	9.19E-05
$Ni_{1.62}Ru_{0.38}P/ SiO_2$	160	8.52	5.32E-05
$Ni_{1.50}Ru_{0.50}P/ SiO_2$	158	7.72	4.90E-05
$Ni_{1.25}Ru_{0.75}P/ SiO_2$	121	3.68	1.40E-05
$Ni_{1.00}Ru_{1.00}P/ SiO_2$	140	3.06	2.19E-05
$Ni_{0.75}Ru_{1.25}P/ SiO_2$	128	5.51	4.30E-05
$Ni_{0.50}Ru_{1.50}P/ SiO_2$	134	3.19	2.38E-05
$Ni_{0.25}Ru_{1.25}P/ SiO_2$	115	6.11	5.30E-05
Ru_2P/SiO_2	134	3.21	2.39E-05

The HDS activity trends well with the HDS conversion of the $Ni_xRu_{2-x}P/SiO_2$ catalysts. The CO chemisorption capacities and turnover frequencies also increase as Ni-content increases. The TOFs were highest for Ni-rich compositions where $1.75 \le x \le 1.85$ and decreased over all as Ru content increased.

To further investigate the $Ni_xRu_{2-x}P/SiO_2$ catalysts and the effect of composition on product selectivity, additional catalysts were tested and the overall and HDS product selectivities at 573 K are plotted as a function of Ru-content in Figure 3.25.

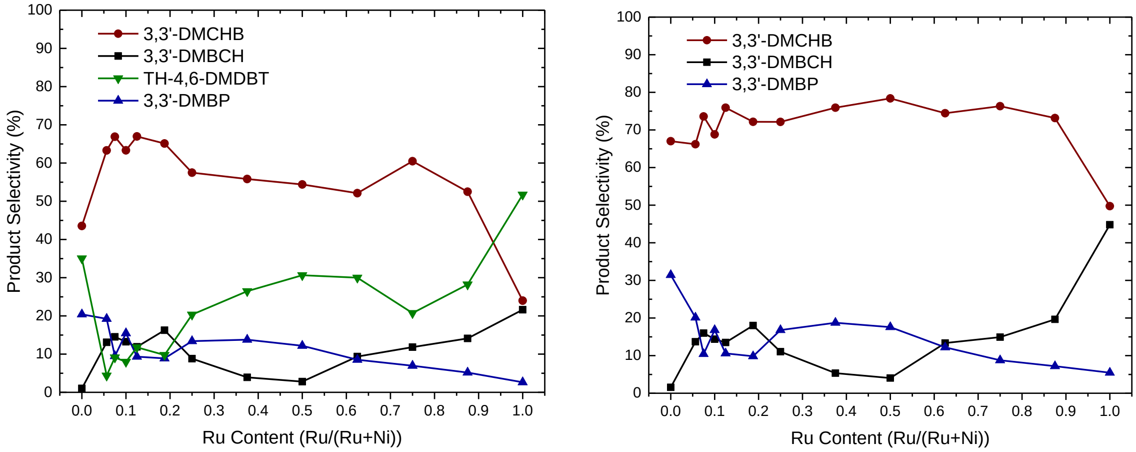

Figure 3.28: Product selectivity (left) and HDS product selectivity (right) as a function of Ru-content at 573 K for 15 wt% $Ni_xRu_{2-x}P/SiO_2$ catalysts.

As Ru-content increased, the product selectivity toward the major product, 3,3'-DMCHB, was observed to remain fairly consistent with the exception of the Ru_2P/SiO_2 catalys. The production of TH-4,6-DMDBT increased with Ru-content to a maximum for the Ru_2P/SiO_2 catalyst where it was the major product. The minor products remained 3,3'-DMBP and 3,3'-DMBCH throughout the catalyst series. The production of 3,3'-DMBP was highest for the Ni_2P/SiO_2 catalyst and decreased with Ru-content to a minimum for the Ru_2P/SiO_2 catalyst. The production of 3,3-DMBCH was lowest for the Ni_2P/SiO_2 catalyst and reached a maximum for the Ru_2P/SiO_2 catalyst. For bimetallic compositions, the major product was 3,3'-DMCHB and represented ~66-78% of HDS products formed.

3.3 HDS Activities and Product Selecivities of $Ni_xRh_{2-x}P/SiO_2$ Catalysts

The HDS measurements for the $Ni_xRu_{2-x}P/SiO_2$ catalysts were carried out over a temperature range of 493-613 K with the reactor at a total pressure of 3 MPa. A model feed comprised of 1000 ppm 4,6-DMDBT in decalin was allowed to flow through the reactor. Once the reactor had stabilized for 24 h, the first measurement was taken at the starting temperature of 533 K, after which the temperature was increase by 20 K. The reactor was allowed to stabilize for at least 4 hours after each temperature ramp prior to taking a measurement. Two sets measurements were taken per 24 h period for a total of 96 h for a full range of temperatures. At each temperature, four effluent samples were collected and analyzed via GC to determine what percentage of 4,6-DMDBT was converted by a catalyst. The relative amounts of four normalized products (3,3'-DMBP, 3,3'-DMCHB, 3,3'-DMBCH, and TH-4,6-DMDBT) (Figure 3.25) were observed at each temperature to determine the product selectivity of a catalyst.

The product selectivity and HDS conversions of 4,6-DMDBT as a function of time by a $Ni_{1.75}Ru_{0.25}P/SiO_2$ catalyst is shown in Figures 3.29.

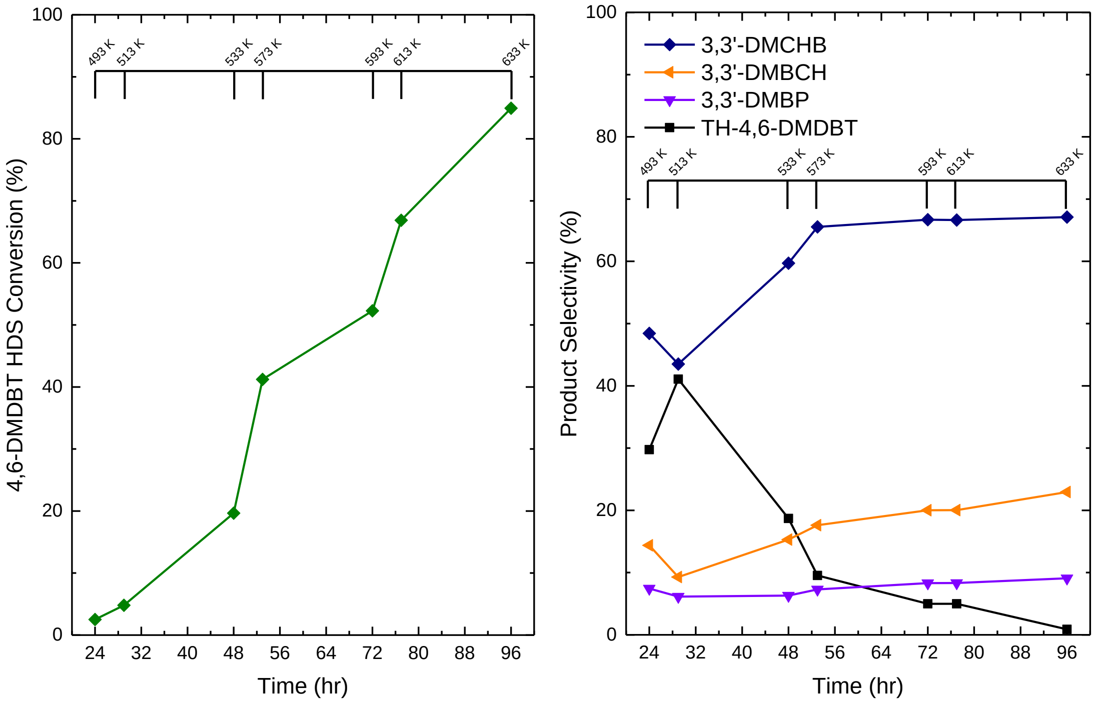

Figure 3.29: 4,6-DMDBT HDS conversion (left) and product selectivity (right) as a function of time for a wt 15% $Ni_{1.75}Rh_{0.25}P/SiO_2$ catalyst over the temperature range of 493-613 K.

The $Ni_{1.75}Rh_{0.25}P/SiO_2$ catalyst was observed to increase its HDS conversion, over time and as temperature increased, leading to a maximum 4,6-DMDBT HDS conversion of 85% at hour 96 and temperature 633 K. The most dramatic increases in HDS conversion happened from hours 48-53 (T = 533-573 K) and hours 72-77 (T = 593-613 K). The product formation of TH-4,6-DMDBT was observed to decrease as time and temperature increased. The production of the major product (3,3’-DMCHB) was observed to initially increase, but remained fairly consistent after hour 53 (T = 573 K). The minor product 3,3’-DMBCH was observed to slightly increase throughout the timeframe while 3,3’-DMBP remained fairly consistent throughout.

The 4,6-DMDBT HDS conversions as a function of temperature for selected 15 wt% $Ni_xRh_{2-x}P/SiO_2$ series is displayed below in Figure 3.30.

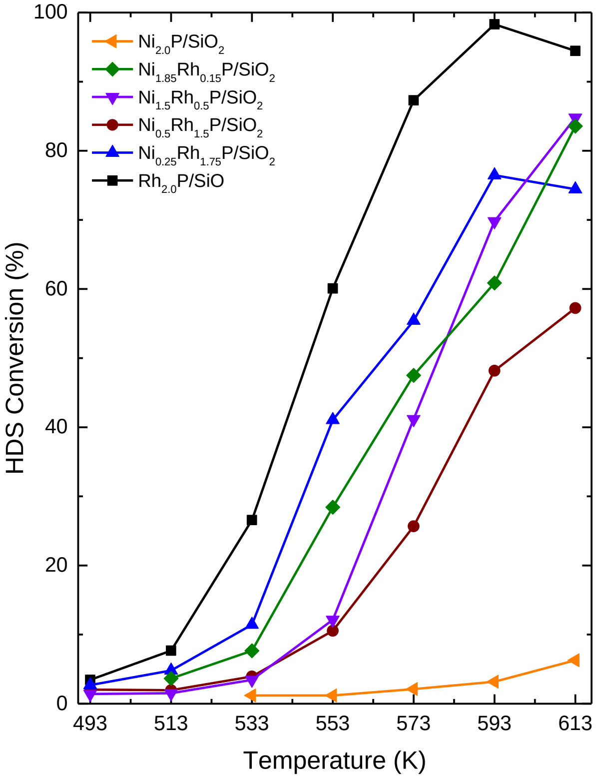

Figure 3.30: The 4,6-DMDBT HDS conversion for selected 15 wt% $Ni_xRh_{2-x}P/SiO_2$ catalysts.

The 4,6-DMDBT HDS conversion increased as the reactor temperature was increased for all $Ni_xRh_{2-x}P/SiO_2$ catalysts. The $Ni_xRh_{2-x}P/SiO_2$ catalysts displayed a maximum HDS conversion for Rh_2P/SiO_2 which reached a maximum HDS conversion at 98% at 593 K. The next highest HDS conversion was observed at composition $Ni_{0.25}Rh_{1.75}P/SiO_2$; however, at 613 K this was surpassed by subsequent Ni-rich catalysts such as $Ni_{1.85}Rh_{0.15}P/SiO_2$ and $Ni_{1.5}Rh_{0.5}P/SiO_2$. In all $Ni_xRh_{2-x}P/SiO_2$ compositions, the HDS of 4,6-DMDBT was significantly higher than Ni_2P/SiO_2. Overall, the $Ni_xRh_{2-x}P/SiO_2$ catalysts were more active than the analogous compositions of the

$Ni_xRu_{2-x}P/SiO_2$ catalysts which was not unexpected as Rh-based phosphides have been shown to be more HDS active than Ru-based phosphides.[32]

To further investigate the $Ni_xRh_{2-x}P/SiO_2$ catalysts and the effect of composition on the HDS of 4,6-DMDBT, additional catalysts were tested and the HDS conversion is plotted as a function of Rh-content at 553 K in Figure 3.31.

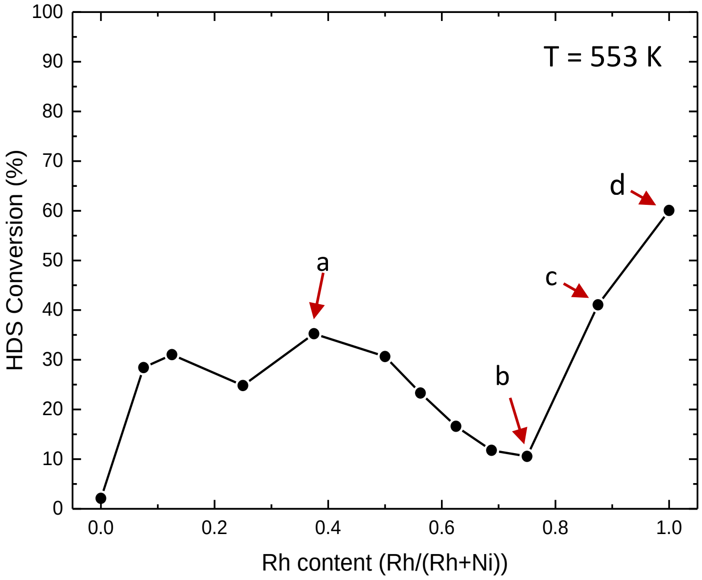

Figure 3.31: 4,6-DMDBT conversion as a function of noble metal content at 553 K for $Ni_xRh_{2-x}P/SiO_2$ catalysts. The following catalysts are labeled above: (a) $Ni_{1.25}Rh_{0.75}P/SiO_2$ (b) $Ni_{0.50}Rh_{1.50}P/SiO_2$ (c) $Ni_{0.25}Rh_{1.75}P/SiO_2$ (d) Rh_2P/SiO_2.

The highest HDS conversion was observed from the Rh_2P/SiO_2 catalyst with the next highest HDS conversion being observed form the $Ni_{0.25}Rh_{1.75}P/SiO_2$. A local minimum in HDS conversion was observed at composition $Ni_{0.50}Rh_{1.50}P/SiO_2$. A local maximum was observed at composition $Ni_{1.25}Rh_{0.75}P/SiO_2$. All compositions showed greater HDS conversion than Ni_2P/SiO_2 and at high Ni-content compositions, such as $1.00 \leq x \leq 1.85$, the average HDS conversion was higher by ~50% than that for compositions of $0.50 \leq x \leq 0.88$.

To further investigate the $Ni_xRh_{2-x}P/SiO_2$ catalysts and the effect of composition on the product selectivity, additional catalysts were tested and the product selectivity at 553 K is plotted as a function of Rh-content in Figure 3.28.

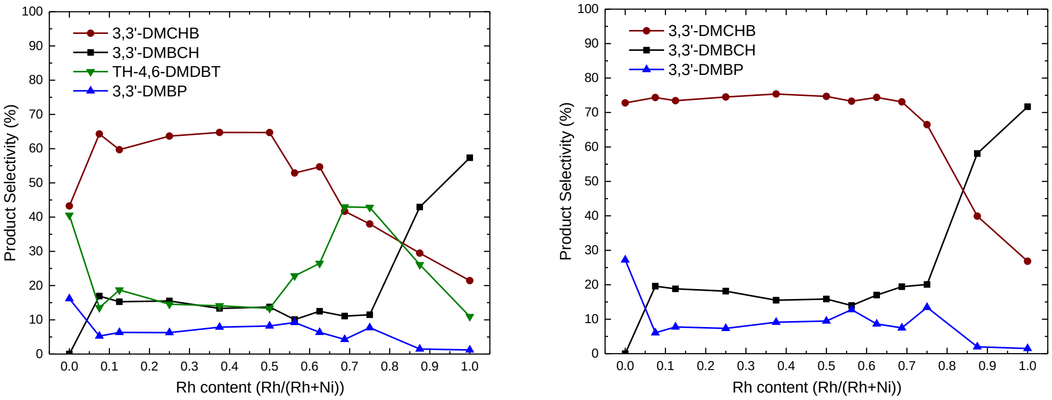

Figure 3.32: Product selectivity (left) and HDS product selectivity (right) as a function of Rh-content at 573 K for $Ni_xRh_{2-x}P/SiO_2$ catalysts.

At low Rh-content (0.1-0.5 Rh/(Rh+Ni)) the major product formed was 3,3’-DMCHB which represented ~75% of products. For these low Rh compositions, the production of minor products, 3,3’-DMBCH, 3,3’-DMBP and TH-4,6-DMDBT, remained fairly linear as did the production of the 3,3’-DMCHB. Prior to these compositions, the Ni_2P/SiO_2 catalyst produced significant amounts of TH-4,6-DMDBT and 3,3’-DMBP, while producing no 3,3’-DMBCH. In Rh-content ranging from 0.5-0.68, it was observed that the production of 3,3’-DMCHB began to decrease while the production of TH-4,6-DMDBT began to increase. At high Rh-content (0.75-1.00) the production of 3,3’-DMBCH began to dramatically increase as the production of TH-4,6-DMDBT began to decrease and 3,3’-DMCHB continued to decrease. The major product for Rh_2P/SiO_2 was observed to be 3,3’-DMBCH, representing ~57% of the normalized products and ~72% of the HDS products.

The turnover frequencies, HDS activities and CO chemisorption capacities for selected $Ni_xRh_{2-x}P/SiO_2$ catalysts are reported in Tables 3.5-3.6.

Table 3.7: CO chemisorption capacities, HDS activity, and turnover frequencies of $Ni_xRh_{2-x}P/SiO_2$ catalysts.

Catalyst	CO Chemisorption Capacity (μmol/g)	Activity @ 553 K (nmol DMDBT/$g_{cat.}$*s)	Turnover Frequency (s^{-1})
Ni_2P/ SiO_2	143	1.22	8.53E-06
$Ni_{1.85}Rh_{0.15}P/ SiO_2$	180	12.0	6.67E-05
$Ni_{1.75}Rh_{0.25}P/ SiO_2$	188	8.28	4.40E-05
$Ni_{1.50}Rh_{0.50}P/ SiO_2$	166	10.4	6.26E-05
$Ni_{1.25}Rh_{0.75}P/ SiO_2$	144	14.9	1.03E-04
$Ni_{1.00}Rh_{1.00}P/ SiO_2$	160	12.9	8.06E-05
$Ni_{0.87}Rh_{1.13}P/ SiO_2$	177	9.83	5.78E-05
$Ni_{0.75}Rh_{1.25}P/ SiO_2$	169	6.96	4.12E-05
$Ni_{0.62}Rh_{1.38}P/ SiO_2$	183	4.99	2.73E-05
$Ni_{0.50}Rh_{1.50}P/ SiO_2$	157	7.45	4.75E-05
$Ni_{0.25}Rh_{1.25}P/ SiO_2$	193	12.7	6.58E-05
Rh_2P/SiO_2	201	25.3	1.26E-04

The HDS activity trends well with the HDS conversion of the $Ni_xRh_{2-x}P/SiO_2$ catalysts; however, the CO chemisorption capacities do not strictly follow such trends.

3.4 Sulfur Analysis on HDS-tested $Ni_xM_{2-x}P/SiO_2$ Catalysts

After being subject to reactor conditions, selected catalysts underwent carbon-sulfur analysis to determine the extent of S incorporation (Table 3.6-7).

Table 3.8: Sulfur analysis of selected $Ni_xRu_{2-x}P/SiO_2$ catalysts.

Catalyst	Raw S wt%	S/M
Ni_2P/ SiO_2	0.282	0.033
$Ni_{1.85}Ru_{0.15}P/ SiO_2$	0.165	0.066
$Ni_{1.80}Ru_{0.20}P/ SiO_2$	0.245	0.037
$Ni_{1.75}Ru_{0.25}P/ SiO_2$	0.219	0.045
$Ni_{1.63}Ru_{0.37}P/ SiO_2$	0.358	0.044
$Ni_{1.50}Ru_{0.50}P/ SiO_2$	0.208	0.017
$Ni_{1.25}Ru_{0.75}P/ SiO_2$	0.011	0.028
$Ni_{1.00}Ru_{1.00}P/ SiO_2$	0.035	0.005
$Ni_{0.75}Ru_{1.25}P/ SiO_2$	0.715	0.038
$Ni_{0.50}Ru_{1.50}P/ SiO_2$	0.155	0.048
$Ni_{0.25}Ru_{1.75}P/ SiO_2$	0.089	0.011
Ru_2P/SiO_2	0.550	0.041

Table 3.9: Sulfur analysis of selected $Ni_xRh_{2-x}P/SiO_2$ catalysts.

Catalyst	Raw S wt%	S/M
Ni_2P/SiO_2	0.282	0.033
$Ni_{1.85}Rh_{0.15}P/SiO_2$	0.216	0.071
$Ni_{1.75}Rh_{0.25}P/SiO_2$	0.196	0.025
$Ni_{1.50}Rh_{0.50}P/SiO_2$	0.376	0.049
$Ni_{1.25}Rh_{0.25}P/SiO_2$	0.215	0.044
$Ni_{1.00}Rh_{1.00}P/SiO_2$	0.382	0.034
$Ni_{0.87}Rh_{1.12}P/SiO_2$	0.244	0.020
$Ni_{0.75}Rh_{1.25}P/SiO_2$	0.213	0.026
$Ni_{0.63}Rh_{1.37}P/SiO_2$	0.257	0.311
$Ni_{0.50}Rh_{1.50}P/SiO_2$	0.262	0.025
$Ni_{0.25}Rh_{1.75}P/SiO_2$	0.376	0.049
Rh_2P/SiO_2	0.120	0.012

The amount of S incorporated into the $Ni_xRu_{2-x}P/SiO_2$ catalysts ranged from 0.011-0.048 wt%. The $Ni_xRh_{2-x}P/SiO_2$ catalysts displayed S incorporation ranging from 0.012-0.071 wt%. Less S was incorporated by the $Ni_xRu_{2-x}P/SiO_2$ than the $Ni_xRh_{2-x}P/SiO_2$ catalysts. Within each catalyst series, the catalyst composition did not appear to contribute to the amount of incorporation of S.

4. Discussion

As global petroleum reserves decline, the United States has begun sourcing increasing amounts of crude oil from unconventional resources such as shale oil and oil sands; such supplies of petroleum contain significant amounts of refractory organosulfur compounds. While the sulfur content has increased, environmental regulations regarding the allowable sulfur content in transportation fuels have decreased to 10 ppm or less of sulfur in fuels such as gasoline and diesel.[7, 8] One major issue in achieving ultra-low sulfur transportation fuels lies in the different varieties of organosulfur compounds found in petroleum; lighter crude oil distillates contain lower-boiling-point organosulfur compounds (473-573 K) that are more reactive and relatively easy to desulfurize when compared with heavier crude oil distillates that contain the more refractory high-boiling point organosulfur compounds (573-673 K).[1,32-34] The conversion of refractory organosulfur compounds to sulfur-free hydrocarbons is known as "deep" HDS and the development of reactors and catalysts for deep HDS processing is a significant technological challenge.

Considerable research focuses on the HDS of 4,6-DMDBT, a substituted dibenzothiophene that represents a class of the most refractory organosulfur compounds.[13,25,29-31,33,35-36] In substituted DBTs, access to catalyst sites by the sulfur atom is greatly hindered by the presence of alkyl groups at the 4 and 6 positions. In the case of 4,6-DMDBT, the methyl substituents at these positions leads to a ten-fold decrease in reactivity relative to DBT.[36]

Transition metal phosphides, specifically Ni phosphides, are the focus of a growing area of research to develop a new class of hydrotreating catalysts.[15-17, 20, 21] In recent years, research studies of metal phosphides have shown them to be highly active in HDS reactions and a significant number of publications have investigated their application for hydrotreating catalysis.[16-18, 37] Different Ni phosphide phases exist (e.g. $Ni_{12}P_5$, Ni_2P, and Ni_5P_4); however, the most active phase for HDS is Ni_2P.[16] Research by the Oyama group discussed the hydrotreating properties and stability of Ni_2P/SiO_2; it was revealed that altering the P/Ni ratio had a profound effect on the tolerance of Ni_2P to sulfur poisoning, resulting in high HDS conversion of DBT.[38] A similar investigation by Bussell and coworkers of the HDS properties of a series of Ni_xP_y/SiO_2 catalysts having different P/Ni ratios showed that using an excess of P (P/Ni = 0.8) in the catalyst precursor yielded a highly HDS active, phase-pure Ni_2P/SiO_2 catalyst.[39] Such research has highlighted the potential of Ni_2P for hydrotreating and has garnered the attention of industrial researchers; an article published in 2015 by ExxonMobil Research and Engineering focused directly on the applicability of Ni_2P as a viable hydroprocessing catalyst.[40] The ExxonMobil researchers concluded that Ni_2P would require average particle sizes of approximately 3 nm to be competitive with state-of-the-art Ni-Mo and Co-Mo sulfide catalysts.[40]

The incorporation of a second metal into a catalyst phase can lead to optimized catalyst properties such as increased HDS activity as well as the ability to alter product selectivity. An example of such optimization was reported by the Oyama group in which the incorporation of Fe into Ni_2P ($Fe_xNi_{2-x}P/SiO_2$) resulted in a selectivity shift from a HYD product to a DDS product for the HDS of 4,6-DMDBT.[25] In the case of conventional Mo sulfide-based catalysts, increased

HDS activity is observed by incorporating promoting atoms, such as Ni or Co, that preferentially occupy the edges of the active sulfide phase (Figure 1.3). Such promotion was reported by Alonso and coworkers in which an increase in the activity for HDS of DBT was attributed to Co atoms occupying the edges of the CoMo sulfide layers.[14] Previous research by the Bussell group has shown Ru_2P and Rh_2P to be highly active phases for HDS. A 8.8 wt% Ru_2P/SiO_2 catalyst was measured to have ~10% higher HDS conversion of DBT than a sulfided Ru/SiO_2 catalyst at 548-573 K. A 5 wt% Rh_2P/SiO_2 catalyst was reported to have ~30% higher DBT conversion than a sulfided Rh/SiO_2 catalyst and ~17% higher conversion than a commercial Ni-Mo/Al_2O_3 catalyst at 548 K.[31] This thesis research focused on the incorporation of Ru and Rh into Ni_2P ($Ni_xM_{2-x}P/SiO_2$) for the purpose of investigating the effect of bimetallic phosphide composition on 4,6-DMDBT HDS conversion and product selectivity.

The metal phosphide phases present in $Ni_xRu_{2-x}P/SiO_2$ catalysts prepared by TPR were confirmed by XRD (Figure 3.5). XRD patterns for compositions having $1.50 \leq x \leq 2.00$ indicated that Ru atoms were incorporated into the hexagonal crystal structure of Ni_2P and that a phase-pure bimetallic phosphide phase was synthesized. At compositions of $0.00 \leq x \leq 0.50$, only XRD peaks consistent with the Ru_2P structure were observed and it was reasoned that Ni was incorporated into the orthorhombic crystal structure of Ru_2P. XRD patterns collected after HDS testing showed no signs of significant sintering of the bimetallic phosphide phase. The $Ni_xRu_{2-x}P/SiO_2$ catalysts showed an overall decrease in CO chemisorption capacity as Ru content increased and the average crystallite sizes, as determined by using the Scherrer equation, ranged from <5 to 8 nm. Metal composition did not significantly affect S incorporation during HDS testing and the measured S/(Ni+Ru) molar ratios were low (0.11-0.66).

The metal phosphide phase present in the $Ni_xRh_{2-x}P/SiO_2$ catalysts prepared by TPR were confirmed by XRD (Figure 3.7). XRD patterns for compositions $1.00 \leq x \leq 2.00$ indicate that Rh atoms were incorporated into the hexagonal crystal structure of Ni_2P and that a phase-pure bimetallic phosphide phase was synthesized. At compositions $0.00 \leq x \leq 0.50$, only XRD peaks consistent with the Rh_2P structure were observed and it was reasoned that Ni was incorporated into the cubic crystal structure of Rh_2P. XRD patterns collected after HDS testing showed no signs of significant sintering of the bimetallic phosphide phase. The $Ni_xRh_{2-x}P/SiO_2$ catalysts showed an overall increase in CO chemisorption capacity as Rh content increased and the average crystallite sizes, as determined by using the Scherrer equation, ranged from <5 to 9 nm. The metal composition did not significantly affect S incorporation during HDS testing and the measured S/(Ni+Rh) molar ratios were low (0.12-0.71).

4.1 HDS over $Ni_xRu_{2-x}P/SiO_2$ Catalysts

A 15 wt% $Ni_{1.85}Ru_{0.15}P/SiO_2$ catalyst exhibited the highest HDS conversion of the $Ni_xRu_{2-x}P/SiO_2$ catalysts and remained stable throughout HDS testing at 533-653 K and 3 MPa. At 573 K, the $Ni_{1.85}Ru_{0.15}P/SiO_2$ catalyst showed 44% higher 4,6-DMDBT HDS conversion than a 15 wt% Ni_2P/SiO_2 catalyst and 40% higher 4,6-DMDBT HDS conversion than a 15 wt% Ru_2P/SiO_2 catalyst. This high HDS conversion can be attributed to an increase in active sites as well as

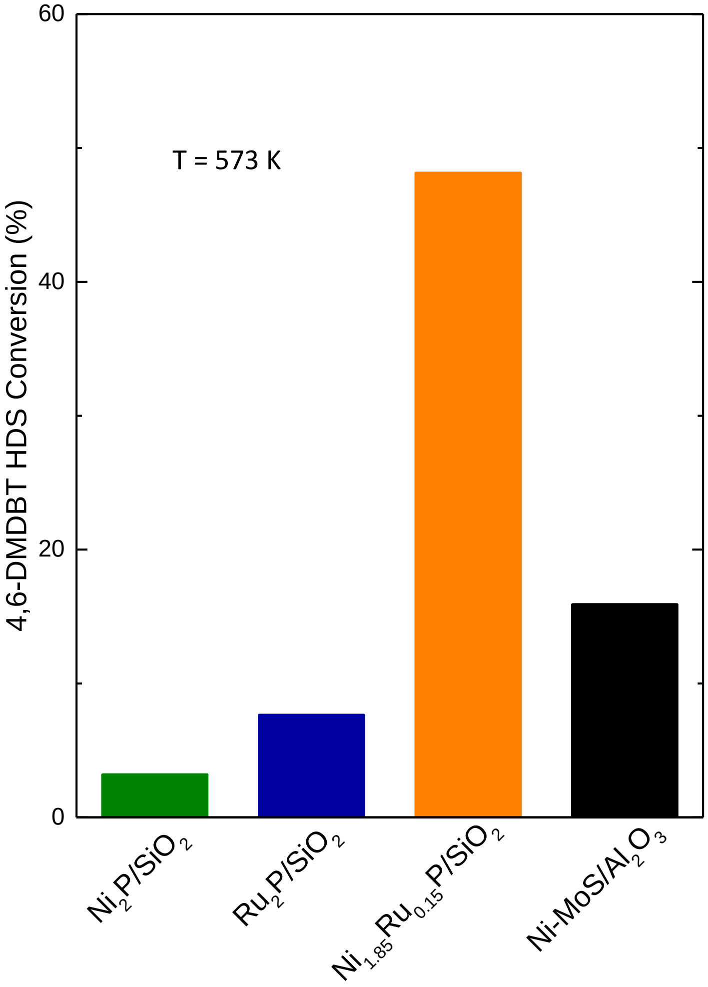

Figure 4.1: 4,6-DMDBT HDS conversions of selected 15 wt% $Ni_xRu_{2-x}P/SiO_2$ catalysts and a sulfided $Ni\text{-}Mo/Al_2O_3$ catalyst at 573 K.

higher activity per site. The HDS conversions of these catalysts at 573 K are compared to that of a sulfided Ni-Mo/Al_2O_3 catalyst in Figure 4.1.

The metal composition had a strong effect on the HDS properties of the $Ni_xRu_{2-x}P/SiO_2$ catalysts as the highest HDS conversions were observed at Ni-rich compositions ($1.62 \leq x \leq 1.85$), which were higher than those of the monometallic phosphide phases (Ni_2P, Ru_2P) and a commercial sulfided Ni-Mo/Al_2O_3 catalyst. Synergist effects existing in sulfided Ni-Ru/Al_2O_3 catalysts were reported by De Los Reyes et al. who proposed that electron donation from Ni to Ru led to an increase of the biphenyl hydrogenation activity.[41, 42] Synergistic effects were also reported by Li and coworkers for Pd-Ni_2P/SiO_2 catalysts in which electron donation from Ni to Pd resulted in highly active, electron-rich sites that aided in the hydrogenation of phenol. The high HDS conversion observed for high Ni-content catalysts in the $Ni_xRu_{2-x}P/SiO_2$ series can be attributed to an increase in the active site densities as determined by CO chemisorption (Figure 4.2) as

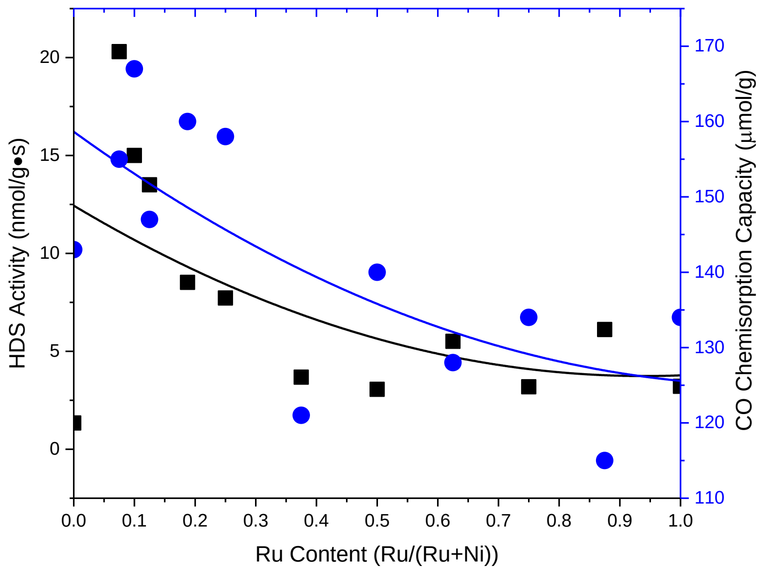

Figure 4.2: CO chemisorption capacities and HDS activities at 573 K for 15 wt% $Ni_xRu_{2-x}P/SiO_2$ catalysts.

well as higher activity per site as determined by the TOFs (Figure 4.3). This suggests synergistic effects between Ni and Ru in the $Ni_xRu_{2-x}P/SiO_2$ catalysts.

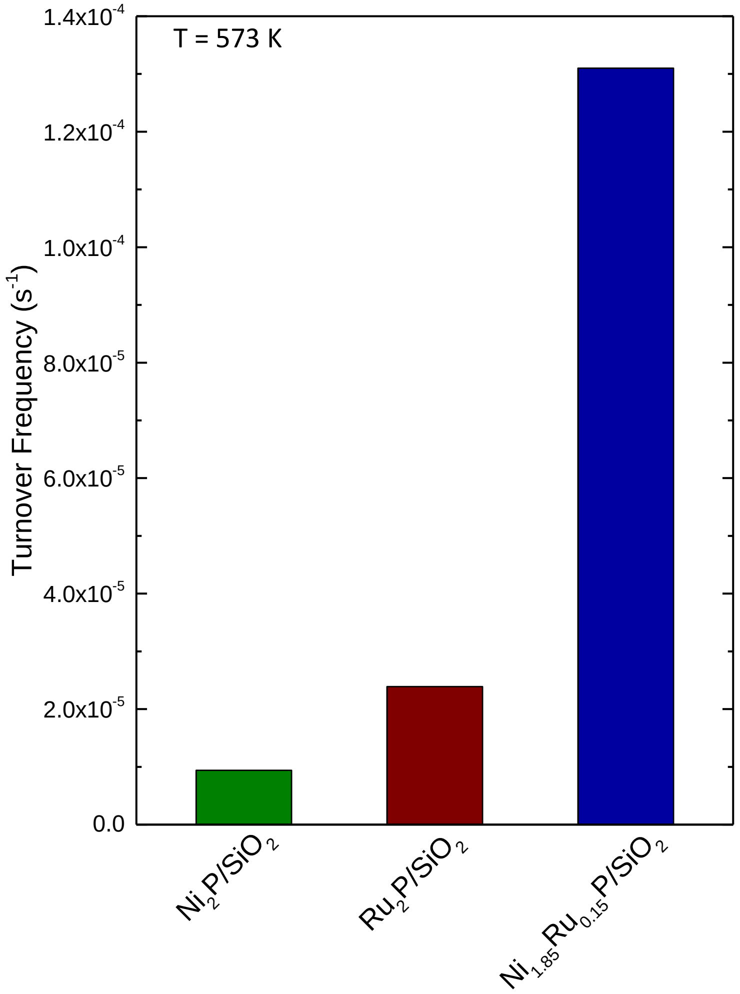

Figure 4.3: TOFs of selected 15 wt% $Ni_xRu_{2-x}P/SiO_2$ catalysts at 573 K.

The high TOFs for the $Ni_xRu_{2-x}P/SiO_2$ catalysts having Ni-rich compositions ($1.75 \le x \le 1.85$) indicate that the active sites of these catalysts were the most active of the Ni-Ru-P bimetallic phosphides (Table 3.6). The highest TOF of the $Ni_xRu_{2-x}P/SiO_2$ series was observed for the $Ni_{1.85}Ru_{0.15}P/SiO_2$ catalyst (1.31×10^{-4} s^{-1}), which indicates the presence of a highly active, Ni-rich phosphide phase that benefits from a small amount of noble metal incorporation. Such synergistic effects have been reported for other bimetallic phosphide phases. Abu and Smith reported increases in the 4,6-DMDBT HDS for a $Ni_{0.3}MoP/Al_2O_3$ catalyst compared to a Ni_2P/Al_2O_3 and conventional Ni-Mo-S catalysts; they suggested that the observed increase in HDS activity was due to greater active site dispersion.[26] Research by the Bussell group reported a 25 wt% $Fe_{0.03}Ni_{1.97}P/SiO_2$ catalyst that was 10% more active for the HDS of DBT than an optimized 25 wt% Ni_2P/SiO_2 catalyst and suggested that increased active site densities and higher TOFs resulted in such high catalytic activity.[27] These reports are consistent with the findings here for the 15 wt% $Ni_xRu_{2-x}P/SiO_2$ catalysts; however, the increased activity cannot be explained simply with increased site density. These results suggest an optimization of the active sites as well as an increase of the active site densities of the $Ni_xRu_{2-x}P/SiO_2$ catalysts. This conclusion is similar to that proposed by De Los Reyes in which a $Ni_{0.4}Ru_{0.6}S_2/Al_2O_2$ catalyst exhibited an increased chemisorption capacity and an increase in activity at Ni and Ru sites due to electron donation from Ni to Ru.[41.42]

The 4,6-DMDBT HDS product selectivities of the $Ni_xRu_{2-x}P/SiO_2$ catalysts did not depend strongly on metal composition; however, the product selectivties of the $Ni_xRu_{2-x}P/SiO_2$ catalysts can give insight into the properties contributing to the observed increase in HDS activity at high Ni-content. The major product formed by the Ni-rich $Ni_xRu_{2-x}P/SiO_2$ catalysts was 3,3'-DMCHB (~70%) and little selectivity was observed for the DDS product, 3,3'-DMBP (<10%). The Ni_2P/SiO_2 catalyst showed a higher selectivity for 3,3'-DMBP (32%). This indicates an enhancement of the HYD pathway with the incorporation of Ru into Ni_2P (Figure 4.4).

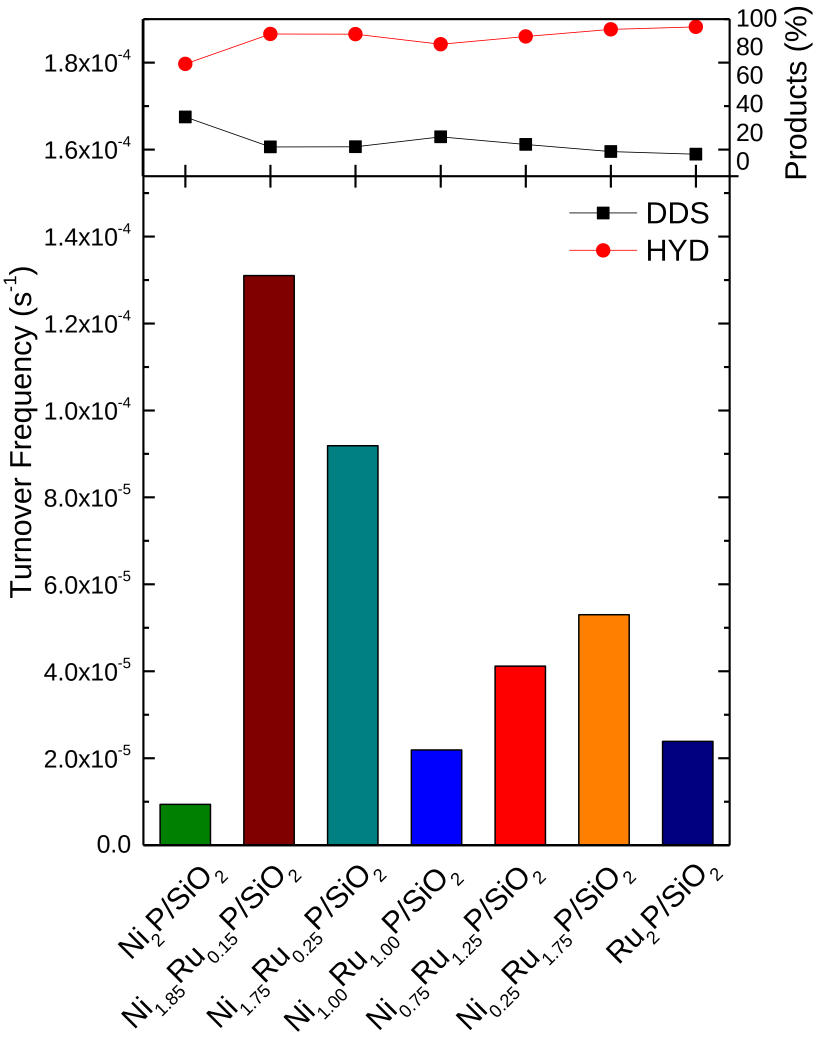

Figure 4.4: TOFs and selectivity of HYD products of selected 15 wt% $Ni_xRu_{2-x}P/SiO_2$ catalysts at 573 K.

It has been discussed in the literature that the incorporation of a noble metal into a nickel phosphide precursor results in an optimization of Ni_2P during the reduction phase. As reported by da Silva et al., H_2 activation at noble metal sites may cause H spillover to the Ni precursor phase and facilitate increased reduction to Ni_2P.[48] Incorporation of a noble metal into the Ni_2P phase has also been reported to lead to increased selectivity for hydrogenation of aromatic rings. [49] These points are discussed further in Section 4.3 in relation to the $Ni_xRh_{2-x}P/SiO_2$ catalysts.

4.2 HDS over $Ni_xRh_{2-x}P/SiO_2$ Catalysts

A 15 wt% Rh_2P/SiO_2 catalyst exhibited the highest HDS conversion for the $Ni_xRh_{2-x}P/SiO_2$ catalyst series and remained stable throughout HDS testing at 493-613 K and 3 MPa. At 553 K, the 15 wt% Rh_2P/SiO_2 catalyst showed 57% higher 4,6-DMDBT HDS conversion than a 15 wt% Ni_2P/SiO_2 catalyst, 20% higher 4,6-DMDBT HDS conversion than a 15 wt% $Ni_{0.25}Rh_{1.75}P/SiO_2$ catalyst, and 31% higher 4,6-DMDBT HDS conversion than a 15 wt% $Ni_{1.85}Rh_{0.25}P/SiO_2$ catalyst. The HDS conversions for these catalysts are compared to a sulfided $Ni\text{-}Mo/Al_2O_3$ catalyst in Figure 4.5.

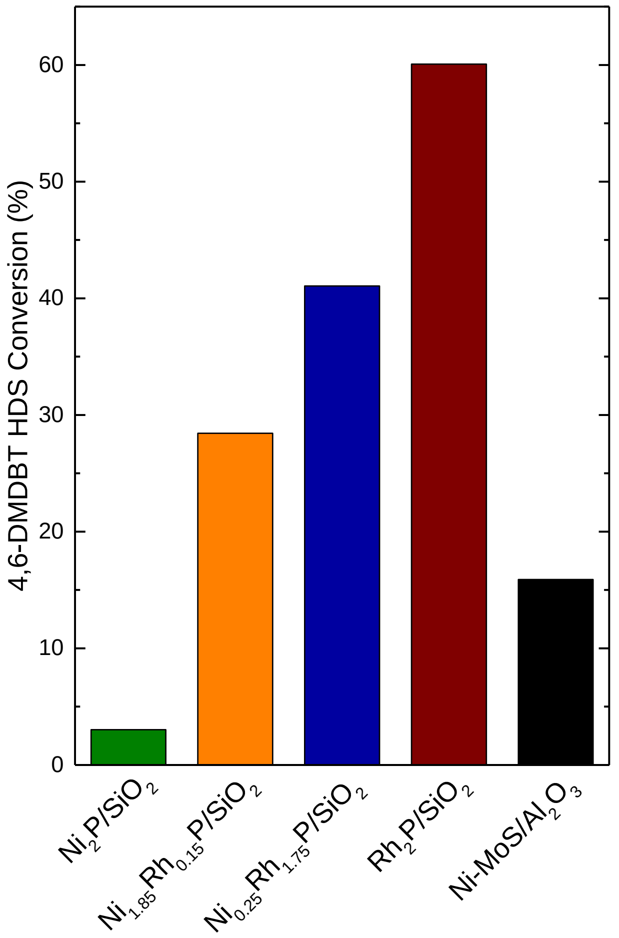

Figure 4.5: 4,6-DMDBT HDS conversions of selected 15 wt% $Ni_xRh_{2-x}P/SiO_2$ catalysts and a conventional sulfided $Ni\text{-}Mo/Al_2O_3$ catalyst at 553 K.

The high 4,6-DMDBT HDS conversion observed for Rh_2P/SiO_2 in this study was not unexpected as a 5 wt% Rh_2P/SiO_2 was T = 553 K reported to be 37% more active than a 25 wt% Ni_2P/SiO_2 catalyst for DBT HDS.[31] Sulfided Rh-based catalysts have been reported to be among the most active catalysts for the HDS of refractory organosulfur compounds.[46, 47] A decrease in HDS conversion from the incorporation of a small amount of Ni into a Rh_2P phase suggests that Ni sites are less active than Rh sites (Figure 4.6). For $Ni_xRh_{2-x}P/SiO_2$ catalysts that exhibited evidence from XRD for both of Ni_2P and Rh_2P phases ($0.63 \leq x \leq 0.75$), the 4,6-DMDBT conversions were lowest of the series; this observed decrease in 4,6-DMDBT HDS conversion is likely due to the presence of a Ni_2P phase in these catalysts (refer to Figure3.8). The 4,6-DMDBT conversion of the $Ni_{1.85}Rh_{0.15}P/SiO_2$ catalyst showed a significant increase in HDS conversion relative to the 15 wt% Ni_2P/SiO_2 catalyst and was measured to have a greater active site density as well as a higher TOF, indicating a dramatically more active catalytic phase from the addition of a small amount of noble Rh.

The 4,6-DMDBT product selectivites for the $Ni_xRh_{2-x}P/SiO_2$ catalysts exhibited a strong dependence on the metal composition. At Ni-rich compositions ($1.00 \leq x \leq 1.85$) the major product was 3,3'-DMCHB, while at Rh-rich compositions ($0.00 \leq x \leq 0.25$) the major product was 3,3'-DMBCH (Figure 4.6).

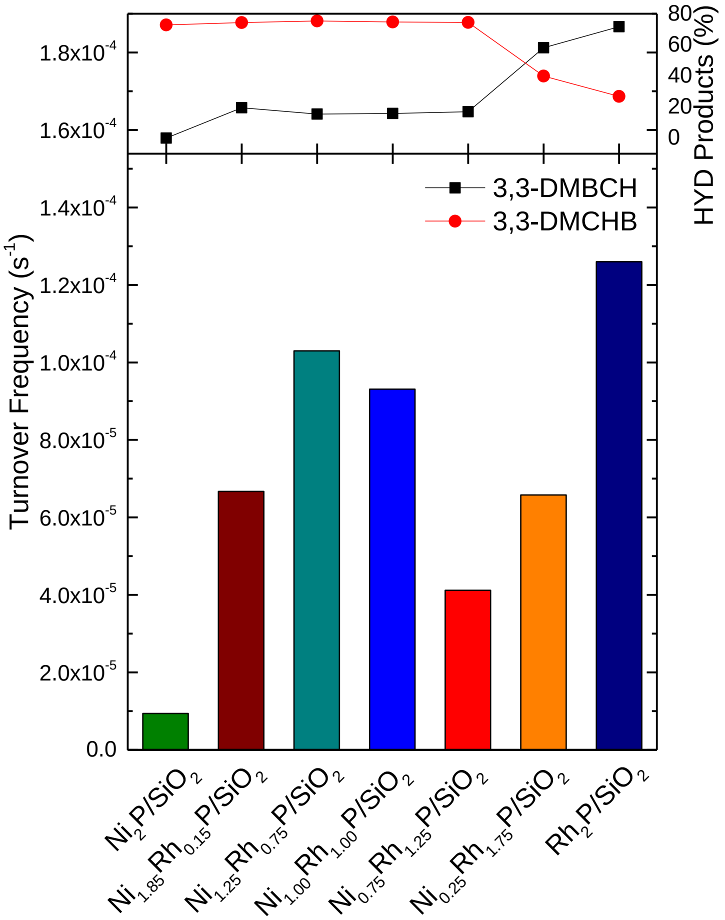

Figure 4.6: TOFs and selectivity of HYD products of selected 15 wt% $Ni_xRh_{2-x}P/SiO_2$ catalysts at 553 K.

The increase in hydrogenation of the aromatic rings of 4,6-DMDBT observed for the $Ni_{0.25}Rh_{1.75}P/SiO_2$ and Rh_2P/SiO_2 catalysts can be attributed to the single type of active site present in the Rh_2P crystal structure, which has been reported to be highly selective for the HYD pathway. The Bussell group observed a 5 wt% Rh_2P/SiO_2 catalyst to be 96% selective for the HYD pathway for DBT HDS at 548 K and while the study did not indicate the ratios of HYD products, the increased hydrogenation properties were attributed to strong sulfur tolerance as it incorporated approximately four times less sulfur than a sulfided Rh/SiO_2 catalyst.[31] The Rh_2P/SiO_2 catalyst presented in this research was measured to incorporate four times less sulfur than the $Ni_{0.25}Rh_{1.75}P/SiO_2$ catalyst and incorporated three times less sulfur than the average for the $Ni_xRh_{2-x}P/SiO_2$ catalysts (refer to Table 3.9).

4.3 Comparing Catalytic Properties of $Ni_xM_{2-x}P/SiO_2$ Catalysts

The increase in HDS activity and active sites that favor the HYD pathway for $Ni_xRu_{2-x}P/SiO_2$ catalysts containing small amounts of noble metal (Rh, Ru) can be explained in two ways: (1) During HDS testing, noble metal sites in the bimetallic phosphide catalysts activate hydrogen and facilitate hydrogen spillover to the Ni sites. A greater degree of hydrogenation occurs at Ni sites due to the excess of available hydrogen. (2) The presence of noble metal induces electron transfer from Ni to the noble metal, resulting in an increase in HDS conversion via the HYD pathway. A study by Teixera da Silva and coworkers reported a low-temperature synthesis of a Pd-Ni_2P phase due to the presence of Pd dissociating H_2 and allowing spillover to the $Ni_3(PO_4)_2$ precursor phase which was then reduced to Ni_2P at 200 K lower than unpromoted precursors.[48] The study proposed that noble-metal-facilitated hydrogen spillover was causing an excess of hydrogen around the Ni precursor allowing for lower reduction temperatures. A study by Li et al. reported synergistic effects for carbonyl hydrogenation in noble metal-Ni_2P/SiO_2 catalysts. In particular, 1% M-10% Ni_2P/SiO_2 catalysts (M = Ru, Pt, and Pd) showed increased hydrogenation properties compared to a 10% Ni_2P/SiO_2 catalyst for the conversion of phenol.[49] The increase in hydrogenation properties observed in the Ni-rich bimetallic phosphide catalysts reported in this research can be attributed to hydrogen spillover, facilitated by the presence of Ru or Rh, to Ni sites. Evidence for hydrogen spillover occurring during the reduction phase was supported by the TPR-MS traces for the evolution of water as seen in Figure 4.7.

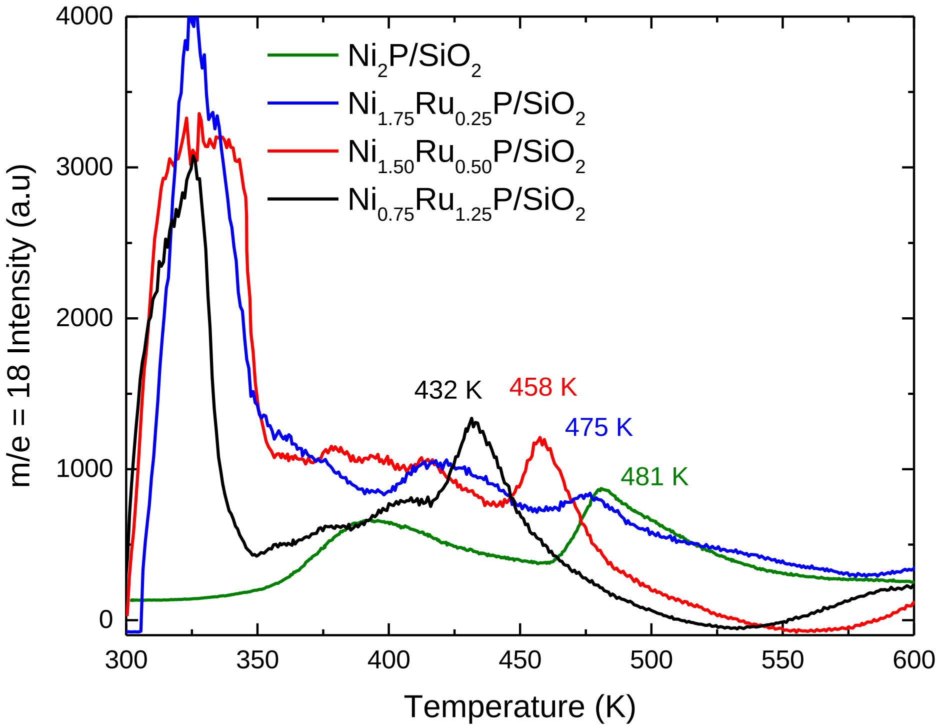

Figure 4.7: MS traces for the evolution of H_2O from the reduction of select $Ni_xRu_{2-x}P/SiO_2$ catalysts.

The reduction of $Ni(H_2PO_2)_2$ for Ni_2P/SiO_2 takes place at 481 K, however with the incorporate of Ru that reduction temperature was observed to decrease. Similar to the results reported by Teixera da Silva and coworkers, the presence of Ru facilitates hydrogen spillover to the $Ni(H_2PO_2)_2$ precursor allowing for lower reduction temperatures. Similarly during HDS testing, hydrogen spillover, from Ru or Rh sites, is allowing excess hydrogen to be present at Ni sites causing an increase in the hydrogenation properties for these sites. This accounts for the increased selectivity for the 3,3'-DMCHB product relative to Ni_2P/SiO_2 as well as the increase active per site as observed from the TOFs. The highest TOFs were observed for the Rh_2P/SiO_2, $Ni_{1.25}Rh_{0.75}P/SiO_2$ and $Ni_{1.85}Ru_{0.15}P/SiO_2$ catalysts (Figure 4.8). The high Rh-content catalysts exhibited high TOFs, which is due to the highly active and highly selective Rh_2P phase showing nearly 100% selectivity for the HYD pathway and significant production of the 3,3'-DMBCH product. The high Ru-content $Ni_xRu_{2-x}P/SiO_2$ catalysts maintained similar selectivity to the Ni-rich catalysts, favoring the HYD pathway. However, they were significantly less active than the Ni-rich $Ni_xRu_{2-x}P/SiO_2$ catalysts. This indicates that Ni_2P is the more active phase when optimized by the incorporation of a small amount of Ru.

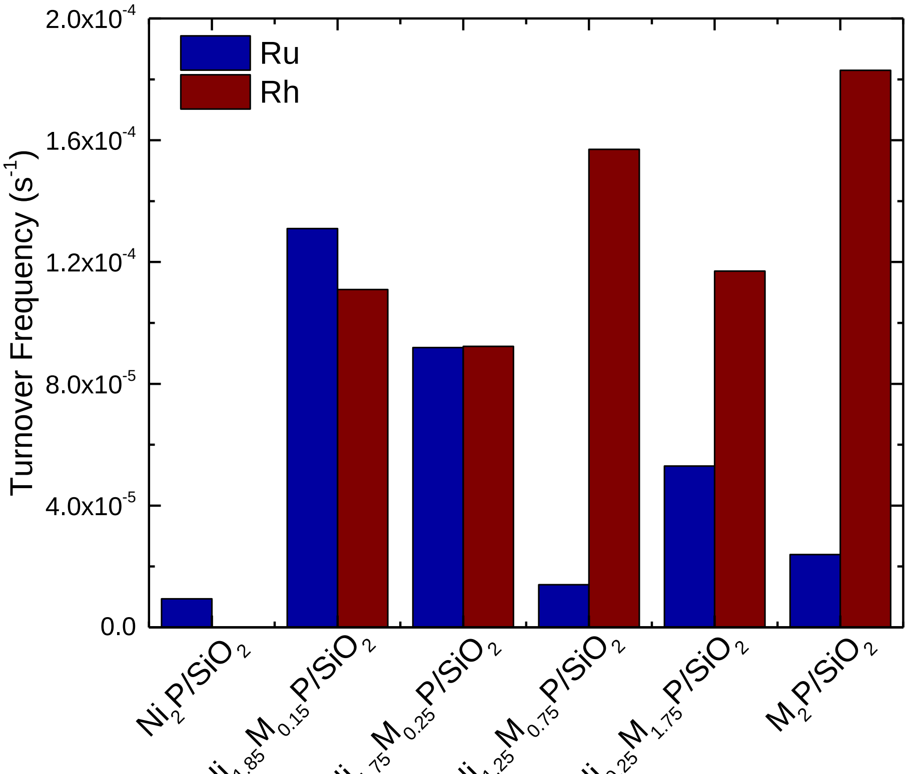

Figure 4.8: TOFs of 15 wt% $Ni_xM_{2-x}P/SiO_2$ (M=Rh, Ru) at 573 K.

From the results presented in this thesis research, the synthesis of a phase-pure bimetallic phosphide catalyst containing Ni and a noble metal (Ru, Rh) leads to increased active site densities as well as active site optimization for the deep HDS of 4,6-DMDBT. In the case of the Ni-rich $Ni_xM_{2-x}P/SiO_2$ catalysts, significantly higher HDS activity than for either Ni_2P/SiO_2 and Ru_2P/SiO_2 was observed because of increased S removal via the HYD pathway to give 3,3'-DMCHB. The Rh-rich $Ni_xRh_{2-x}P/SiO_2$ catalysts also exhibited increased desulfurization by the HYD pathway, but yielded the fully hydrogenated product, 3,3'-DMBCH. Incorporating small amounts of a noble metal (Ru or Rh) into Ni-rich bimetallic phosphide catalysts may have practical applications. The use of high noble metal contents would likely be cost prohibitive, but these results indicate that the product selectivity of 4,6-DMDBT HDS can be controlled by the metal composition of the bimetallic phosphides. In order for the catalysts presented in this research to compete with state-of-the-art Mo-sulfide-based hydrotreating catalysts used in industry, further optimization of the surface area and particle size will be needed, as noted by researchers at ExxonMobil Research and Engineering.[40] Such optimization could be accomplished by using a higher surface area support and optimizing the TPR synthesis to lower the reduction temperature.

5. Conclusion

The goal of this research was to synthesize and characterize a series of 15 wt% $Ni_xM_{2-x}P/SiO_2$ (M = Rh, Ru) catalysts and to investigate the effects of metal composition on the HDS of 4,6-DMDBT for these catalysts. The HDS properties of the $Ni_xRu_{2-x}P/SiO_2$ catalysts were tested to be more active for Ni-rich compositions and the TOFs indicated that the active sites of Ni-rich $Ni_xRu_{2-x}P/SiO_2$ catalysts were more active when compared to Ni_2P and Ru_2P catalysts. The measured increase in CO chemisorption capacities at Ni-rich compositions in consideration with the higher TOFs, suggest synergistic effects between Ni and Ru in the bimetallic phosphide phases. The metal compositions affected the $Ni_xRu_{2-x}P/SiO_2$ catalysts as strong selectivity for the 3,3’-DMCHB product was observed for Ni-rich catalysts; this indicated the presence of highly active sites in the hexagonal crystal structure. Of the $Ni_xRh_{2-x}P/SiO_2$ series, the most active was the Rh_2P/SiO_2 catalyst and it displayed strong selectivity for the 3,3’-DMBCH product. This indicated that the active site of the Rh_2P phase favored complete hydrogenation of the aromatic rings of 4,6-DMDBT even with a small incorporation of a second metal. The TOFs of the $Ni_xRh_{2-x}P/SiO_2$ and $Ni_xRu_{2-x}P/SiO_2$catalysts indicated that Rh_2P/SiO_2 was the most active catalyst tested in this research, however $Ni_{1.85}Ru_{0.15}P/SiO_2$ and $Ni_{1.85}Rh_{0.15}P/SiO_2$ displayed similar TOFs indicating that a bimetallic phosphide catalyst with a Ni_2P phase can be tailored in its metal composition to have dramatically increased catalytic properties relative to Ni_2P catalyst. In order to further investigate the synergistic effects present in these catalysts, information regarding the active sites present in the $Ni_xM_{2-x}P/SiO_2$ (M = Rh, Ru) catalysts is needed. Using CO as a probe molecule of the catalyst active sites, Fourier transform infrared spectroscopy (FT-IR) would reveal information regarding the types and relatives abundances of active sites present in $Ni_xM_{2-x}P/SiO_2$ (M = Rh, Ru) catalysts and provide insight into the proposed electron donation form Ni to Ru (and Rh) and how this leads to optimization of the catalyst active sites.

References

1. Topsøe, H.; Clausen, B. S.; Massoth, F. E. Hydrotreating Catalysis. Springer-Verlag; Berlin, **1996**.
2. Boubel, R. W.; Fox, D. L.; Turner, D. B.; Stern, A. C. Fundamentals of Air Pollution. Academic Press; San Diego, **1994**, pg 100.
3. U.S. Environmental Protection Agency. NOX How Nitrogen Oxides Affect the Way We Live and Breath. https://nepis.epa.gov/Exe/ZyPDF.cgi/P10006ZO.PDF?Dockey=P10006ZO.PDF (accessed March 2017).
4. Brandt, E. P.; Wang, Y.; Grizzle, J. W. *Contr. Sys. Technol.* **1999**, *20*, 1.
5. Prins, R. Catalysis: From Principals to Applications. Wiley; Weinheim, **2012**, pg 390.
6. Bartholomew, C. H.; Agrawal, P. K.; Katzer, J. R. *Adv. In Catal.* **1982**, *31*, 135-242.
7. U.S. Environmental Protection Agency. http://www.epa.gov/ (accessed Jan, 2017).
8. Pawelec, B.; Navarro, R. M.; Campos-Martin, J. M.; Fierro, J. L. G. *Catal. Sci. Technol.* **2011**, *1*, 23.
9. U.S. Energy Information Administration. http://www.eia.gov/ (accessed Jan, 2017).
10. Raybaud, P.; Hafner, J.; Kresse, G.; Kasztelan, S.; Toulhoat, H.*, J. Catal.* **2000**, *190*, 128.
11. Bej, S. K.; Maity, S. K.; Turagne, U. T. *Energy Fuels* **2004**, 18, 1227-1237.
12. Yang, L.; Li, X.; Wang, A.; Prins, R.; Wang, Y.; Chen, Y.; Duan, X. *J. Catal.* **2014**, *317*, 144.
13. Li, X.; Wang, A.; Egorova, M.; Prins, R. *J. Catal.* **2007**, *250*, 283.
14. Nava, H.; Ornelas, C.; Aguilar, A.; Berhault, G.; Fuentes, S.; Alonso, G. *Catal. Lett.* **2003**, *86*, 257.
15. Vit, Z.; Gulkova, D.; Kaluza, L.; Kupcik, J. *App. Catal. B* **2015**, *179*, 44.
16. Prins, R.; Bussell, M. E. *Catal. Lett.* **2012**, *142*, 1413.
17. Oyama, S. T.; Wang, X.; Requejo, F. G.; Sato, T.; Yoshimuar, Y. *J. Catal.* **2002**, *209*, 1.
18. Sawhill, S. J.; Phillips, D. C.; Bussell, M. E. *J. Catal.* **2003**, *215*, 208.
19. Rundqvist, S. *Acta Chem. Scand.* **1962**, *16*, 993.
20. Kanama, D.; Oyama, S. T.; Otani, S.; Cox, D. F. *Surf. Sci.* **2004**, *552*, 8.
21. Danforth, S. J. Masters Thesis, Western Washington University, Bellingham, Wa, 2015.
22. Hernandez, A. B.; Ariga, H.; Takakusagi, S.; Kinoshita, K.; Suzuki, S.; Otani, S.; Oyama, S. T.; Asakura, K. *Chem. Phys. Lett.* **2011**, *513*, 48.

23. Li, Q.; Hu, X. *Phys. Rev. B* **2006**, *74*, 35414.

24. Sachtler, W. H.M.; van Santen R. A. *Adv. Catal.* **1977**, *26*, 69.

25. Oyama, S. T.; Zhao, H.; Freund, H. J.; Asakura, K.; Wlodarczyk, R.; Sierka, M. *J. Catal.* **2012**, *285*, 1.

26. Abu, I. I.; Smith, K. J. *J. Catal.* **2006**, *241*, 356-366.

27. Burns, A. W.; Gaudette, A. M.; Bussell, M. E. *J. Catal.* **2008**, *260*, 262-269.

28. JCPDS—International Centre for Diffraction Data. PDF-4/full file relational database. International Centre for Diffraction data: Newtown Square, Pa. **2002**.

29. Bowker, R. H.; Smith, M. C.; Pease, M. L.; Slenkamp, K. M.; Kovarik, L.; Bussell, M. E. *ACS Catal.* **2011**, *1, 917-922*

30. Bowker, R. H.; Smith, M. C.; Carrillo, B. A.; Bussell, M. E. *Top. Catal.* **2012**, *55*, 999-1009

31. Hayes, J. R.; Bowker, R. H.; Gaudette, A. F.; Smith, M. C.; Moak, C. E.; Nam, C. Y.; Pratum, T. K.; Bussell, M.E. *J. Catal.* **2010**, *276*, 249-258

32. Houalla, M.; Broderick, D.H.; Sapre A.V.; Nag N.K.; de Beer, V.H.J.; Gates, B.C.; Kwart H. *J Catal* **1980**, *61,* 523.

33. Rashidi, F.; Sasaki, T.; Rashidi, A. M.; Kharat, A. N.; Jozani, K. J. *J. Catal.* **2013**, *299*, 321-335.

34. Babich, I. V.; Moulijn, J. A. *Fuel*. **2003**, *82*, 607-631.

35. Isoda, T.; Takase, Y.; Kusakabe, K.; Morooka, S. *Energy Fuels* **2000**, *14*, 585-590.

36. Hermann, N.; Brorson, M.; Topsøe, H. *Catal. Lett.* **1999**, *65*, 169-174.

37. Oyama, S. T. *J. Catal.* **2003**, *216*, 343-352.

38. Oyama, S. T.; Wang, X.; Lee, T. K.; Bando, K. Requejo, F. G. *J. Catal.* **2002**, *210*, 207-217.

39. Sawhill, S. J.; Layman, K. A.; Van Wyk, D. R.; Engelhard, M. H.; Wang, C.; Bussell, M. E. *J. Catal.* **2005**, *231,* 300-313.

40. Soled, S.; Miseo, S.; Baumgartner, J.; Guzman, J.; Bolin, T.; Meyer, R. *Catal. Today* **2015**, *246*, 3-8.

41. De Los Reyes, J. A.; Vrinat, M.; Geantet, C.; Breysse, M.; Grimblot, *J. Catal.* **1993**, *142*, 455-464.

42. De Los Reyes, J. A.; Vrinat, M.; Breysse, M.; Mauge, F.; LaValley, J. C. *Catal. Lett.* **1992**, *13*, 213-220.

43. Demirbas, A. *Energy Policy* **2007**, *25*, 4661-4670.

44. Oyama, S. T.; Lee, Y. K. *J. Catal.* **2008**, *258*, 393-400.

45. Gaudette, A. M.; Burns, A. W.; Hayes, J. R.; Smith, M. C.; Bowker, R. H.; Seda, T.; Bussell, M. E. *J. Catal.* **2010**, *272*, 18-27.

46. Harris S.; Chianelli, R. R. *J. Catal.* **1984**, *86*, 400-412.

47. Ledoux, M. J.; Michaux, O.; Agostini, G. *J. Catal.* **1986**, *102*, 275-288.

48. Teixeria da Siliva, V.; Sausa, L. A.; Amorim, R. M.; Andrini, L.; Figueroa, S. J. A.; Requejo, F. G.; Vicentini, F. C. *J. Catal.* **2011**, *279*, 88-102.

49. Li, Y.; Yang, X.; Zhu, L.; Zhang, H.; Chen, B. *RSC. Adv*. **2015**, *5*, 80388-80396.